DEVELOPMENT OF CONFOCAL X-RAY FLUORESCENCE TECHNIQUES FOR BIOLOGICAL AND ARCHAEOLOGICAL APPLICATIONS

A Thesis Submitted to the College of

Graduate Studies and Research

In Partial Fulfillment of the Requirements

For the Degree of Doctor of Philosophy

In the Department of Geological Sciences

University of Saskatchewan

Saskatoon

By

SANJUKTA CHOUDHURY

PERMISSION TO USE

In presenting this thesis in partial fulfilment of the requirements for a Postgraduate degree from the University of Saskatchewan, I agree that the Libraries of this University may make it freely available for inspection. I further agree that permission for copying of this thesis in any manner, in whole or in part, for scholarly purposes may be granted by the professor or professors who supervised my thesis work or, in their absence, by the Head of the Department or the Dean of the College in which my thesis work was done. It is understood that any copying or publication or use of this thesis or parts thereof for financial gain shall not be allowed without my written permission. It is also understood that due recognition shall be given to me and to the University of Saskatchewan in any scholarly use which may be made of any material in my thesis.

Requests for permission to copy or to make other use of material in this thesis in whole or part should be addressed to:

Head of the Department of Geological Sciences

114 Science Place, University of Saskatchewan

Saskatoon, Saskatchewan S7N 5E2

ABSTRACT

X-ray fluorescence imaging (XFI) is a versatile tool for determining spatial distributions of elements or elemental species within a variety of samples. A newer XFI variant, confocal X-ray fluorescence imaging (CXFI), shows significant promise since confocal detection facilitates important advantages such as three-dimensionally resolved elemental investigation, preservation of sample integrity and higher sensitivity. Additionally, a readily available extension of CXFI, confocal X-ray absorption spectroscopy (CXAS), allows determination of elemental speciation within a specific localized volume element. To enable direct visualization of three-dimensional elemental distribution and speciation in intact biological samples without staining or thinning, this thesis aimed at developing CXFI and CXAS for biological and archaeological applications.

CXFI and CXAS technique development included installing and refining the polycapillary based setup at beamline 20ID-B, Advanced Photon Source (APS), USA, and verifying the feasibility of different configurations through select measurements. In addition, a novel X-ray detection focusing optic, the spoked channel array (SCA) recently developed at the Cornell High Energy Synchrotron Source (CHESS), USA, was implemented to provide superior spatial resolution.

CXFI and CXAS were used to study the following scientific problems:

a) *Embryonic exposure to elevated selenium in zebrafish:* The localization and chemical form of maternally transferred selenium were studied in an early developmental stage of life to understand the effect of exposure.

b) *Highly localized Fe speciation within intact corrosion layer in antique stained glass:* SCA derived CXAS was employed to determine iron speciation in an antique stained glass sample from 13th century Paderborn Cathedral, Germany to aid the study of cleaning methods used in restoration.

c) *Differentiating diagenesis from biogenicity:* Archaeological bone samples from the Royal Naval Hospital Cemetery (c. A.D. 1793-1822), Antigua were studied in an attempt

to distinguish between diagenetic and biogenic lead uptake. Systematic comparisons of conventional XFI with polycapillary and SCA-based CXFI showed that lateral spatial resolution was remarkably improved with SCA optics.

This research facilitated incorporating CXFI and CXAS at beamline 20ID-B, APS and establishing SCA optics as a valuable addition to the confocal X-ray detection toolkit. These capabilities will be implemented at the BioXAS imaging beamline at the Canadian Light Source.

ACKNOWLEDGEMENTS

I am deeply indebted to my supervisors Drs. Ingrid J. Pickering, Graham N. George and Ian Coulthard for their invaluable guidance throughout my doctoral program. I express sincere gratitude to them for the encouragement, direction, inputs and funding without which this thesis would not have been possible. I gratefully acknowledge the guidance from my advisory committee, Drs. Dean Chapman, Pat Krone and Helen Nichol, throughout this dissertation.

I am thankful to Drs. Robert Gordon and Zou Finfrock, beamline scientists, Advanced Photon Source (APS) for their support during beamtime. I am also thankful to Dr. Arthur Woll, beamline scientist, Cornell High Energy Synchrotron Source (CHESS) for the opportunity to work with his novel optics and support during beamtime. This thesis involved collaborations with researchers from a variety of disciplines for which specific acknowledgements are included in the relevant chapters.

I am a fellow in the Canadian Institutes of Health Research Training grant in Health Research Using Synchrotron Techniques (CIHR-THRUST). I would like to thank CIHR-THRUST and the Canadian Light Source (CLS) for support.

This thesis is predominantly based on synchrotron data collected at APS beamline 20ID-B through the CLS-APS Partnership Agreement (chapters 2-6). Data were also obtained at CHESS (section 2.3.2) and at the Stanford Synchrotron Radiation Lightsource (SSRL) (sections 3.6.2, 5.6.2 and 6.6.2). Complete facility acknowledgements are included in the respective chapters.

I would like to thank all Molecular and Environmental Science Research Group members for making my student life rewarding. Finally, my gratitude and thanks to my family for their encouragement and support.

DEDICATION

To my parents,

Uma Sankar and Reba Choudhury,

who gave me life, nurtured, inspired and supported me to be here today.

TABLE OF CONTENTS

LIST OF FIGURES

LIST OF TABLES

LIST OF ABBREVIATIONS

AAS	Atomic Absorption Spectrophotometry
ANKA	Angströmquelle Karlsruhe
APS	Advanced Photon Source
BESSY	Berliner Elektronenspeichering Für Synchrotronstrahlung
BSRF	Beijing Synchrotron Radiation Facility
CHESS	Cornell High Energy Synchrotron Source
CIHR	Canadian Institutes of Health Research
CLS	Canadian Light Source
CNRS	Centre National de la Recherche Scientifique
CPS	Counts Per Second
CXAS	Confocal X-Ray Absorption Spectroscopy
CXFI	Confocal X-Ray Fluorescence Imaging
DOE	Department of Energy
DRIE	Deep Reactive Ion Etching
ESRF	European Synchrotron Radiation Facility
EXAFS	Extended X-Ray Absorption Fine Structure
FWHM	Full Width at Half Maximum
HASYLAB	Hamburger Synchrotronstrahlungslabor

ICP AES	Inductively Coupled Plasma Atomic Emission Spectrometry
K-B	Kirkpatrick-Baez
LA ICPMS	Laser Ablation Inductively Coupled Plasma Mass Spectrometry
LCO	Large Canal Osteon
LNLS	Laboratório Nacional De Luz Síncrotron
MCA	Multiple Channel Analyzer
PBST	Phosphate Buffered Saline Tween
PMMA	Poly (Methyl Methacrylate)
RSC	Royal Society of Chemistry
SCA	Spoked Channel Array
SEM	Scanning Electron Microscopy
SSRL	Stanford Synchrotron Radiation Lightsource
THRUST	Training Grant in Health Research Using Synchrotron Techniques
XANES	X-ray Absorption Near Edge Structure
XAS	X-ray Absorption Spectroscopy
XFI	X-ray Fluorescence Imaging
XRF	X-ray Fluorescence

CHAPTER 1. Introduction

1.1 X-ray Fluorescence Imaging

X-ray fluorescence imaging (XFI)[1] is a well established technique for direct visualization of the elemental and chemical species distributions in a variety of matrices. Important benefits of XFI include elemental specificity, relative non-destructiveness, and minimal or no pre-treatment of sample. In an XFI experiment, the sample is bombarded with an X-ray beam of energy selected to be above the absorption edges of all elements of interest. Although a conventional X-ray source can be used for this application, a state-of-the-art synchrotron source[2] is preferred in many experiments due to its greater brightness and tunability. The absorption of X-rays by atoms of the target elements causes excitation of electrons resulting in core holes. These core holes are then rapidly filled by the decay of outer electrons resulting in a release of energy equal to the energy difference between the initial and final states of the transitions. This energy is characteristic of the specific element excited. This released energy escapes from the sample either in the form of fluorescence emission (electromagnetic radiation) or Auger electrons.[3] It is the former which is detected in an XFI experiment. Figure 1.1 shows a simplified schematic diagram demonstrating the X-ray fluorescence emission from an atom.

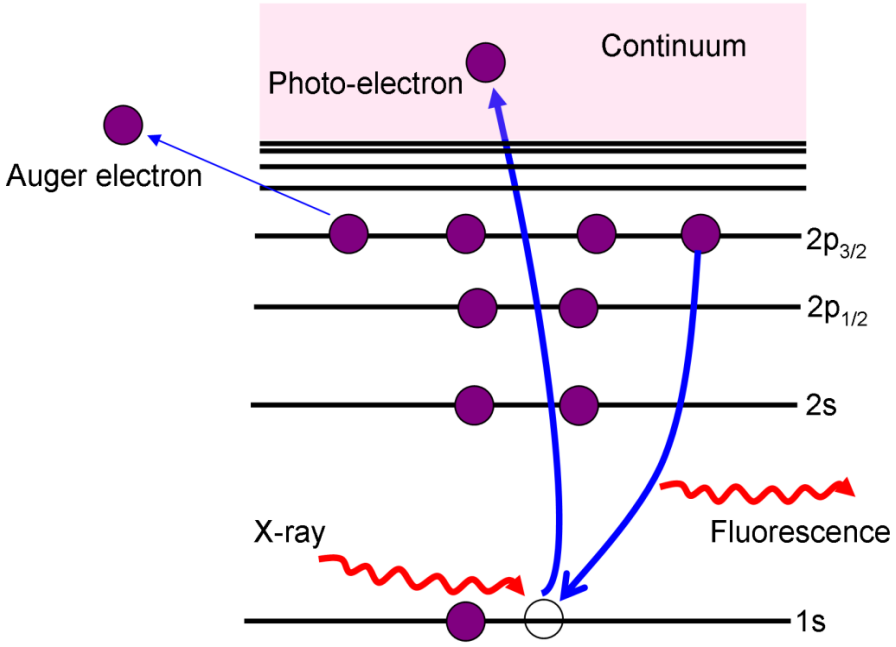

Figure 1.1 Schematic diagram showing the physics of X-ray absorption and fluorescence emission in an atom. Incident X-ray excites a 1s electron as a photo-electron to the continuum resulting in a core hole. The core hole is filled by the dipole allowed decay of a $2p_{3/2}$ or $2p_{1/2}$ electron with a concomitant emission of X-ray fluorescence.

Figure 1.2 shows a diagram displaying the nomenclature of energy levels and examples of transitions giving rise to some characteristic fluorescence emission lines. The energy of an electron within an atom depends on three associated quantum numbers, which are known as: principle quantum number, n; azimuthal or orbital angular quantum number, ℓ; and total angular momentum quantum number, j. The principal quantum number is allowed to have integer values of $n = 1, 2, 3, \ldots$ which derive the allowed values of azimuthal quantum number as $\ell = 0, 1, 2, \ldots n\text{-}1$ and total angular momentum quantum number as $j = \ell \pm ½$. Traditionally, the atomic shells are labeled with letters K, L, M, …, which respectively correspond to $n = 1, 2, 3 \ldots$ and the atomic orbitals are denoted by letters s, p, d, …, which respectively correspond to $\ell = 0, 1, 2 \ldots$. The number of electrons in each energy level is $2j + 1$. The possible transition of an electron from one energy level to the other is constrained by the selection rules for absorption and emission of electromagnetic radiation. These are the electric dipole selection or Laporte rule[4] ($\Delta\ell = \pm 1$) leading to the most intense lines, and the magnetic dipole- and the electric quadrupole selection rules attributed to certain weak features in the spectra. The most important of the

forbidden transitions are the magnetic dipole transitions for which $\Delta\ell = 0$; $\Delta j = 0$ or ± 1 and the electric quadrupole transitions for which $\Delta\ell = 0, \pm 2$; $\Delta j = 0, \pm 1$, or ± 2. A complete listing of the emission lines and corresponding characteristic energies for all elements are available in X-ray data booklet.[5] Generally, the most intense fluorescence lines, specifically the K_α and L_α lines respectively for K and L edges are studied in an XFI experiment. According to the dipole selection rule, the most intense K X-ray fluorescence lines are $K_{\alpha 1}$ and $K_{\alpha 2}$, which respectively originate from the $2p_{3/2} \rightarrow 1s_{1/2}$ and $2p_{1/2} \rightarrow 1s_{1/2}$ transitions. The lines $K_{\beta 1}$ and $K_{\beta 2}$, which are of secondary intensity, respectively originate from the $3p_{3/2} \rightarrow 1s_{1/2}$ and $3p_{1/2} \rightarrow 1s_{1/2}$ transitions. Although the most intense K_α lines are of primary interest in an XFI experiment, the use of a K_β line may be necessary if the K_α is not usable due to an overlap with some other peak generated in the experiment. The L X-ray fluorescence lines are used when the excitation energy for a K-edge is too high to be available in a beamline, for example in the case of a heavy element such as Hg or Pb. The spectroscopic notations for three L-edges are $2s_{1/2}$, $2p_{1/2}$, and $2p_{3/2}$. The most intense L X-ray fluorescence lines are $L_{\alpha 1}$ and $L_{\beta 1}$, which respectively originate from the $3d_{5/2} \rightarrow 2p_{3/2}$ and $3d_{3/2} \rightarrow 2p_{1/2}$ transitions.

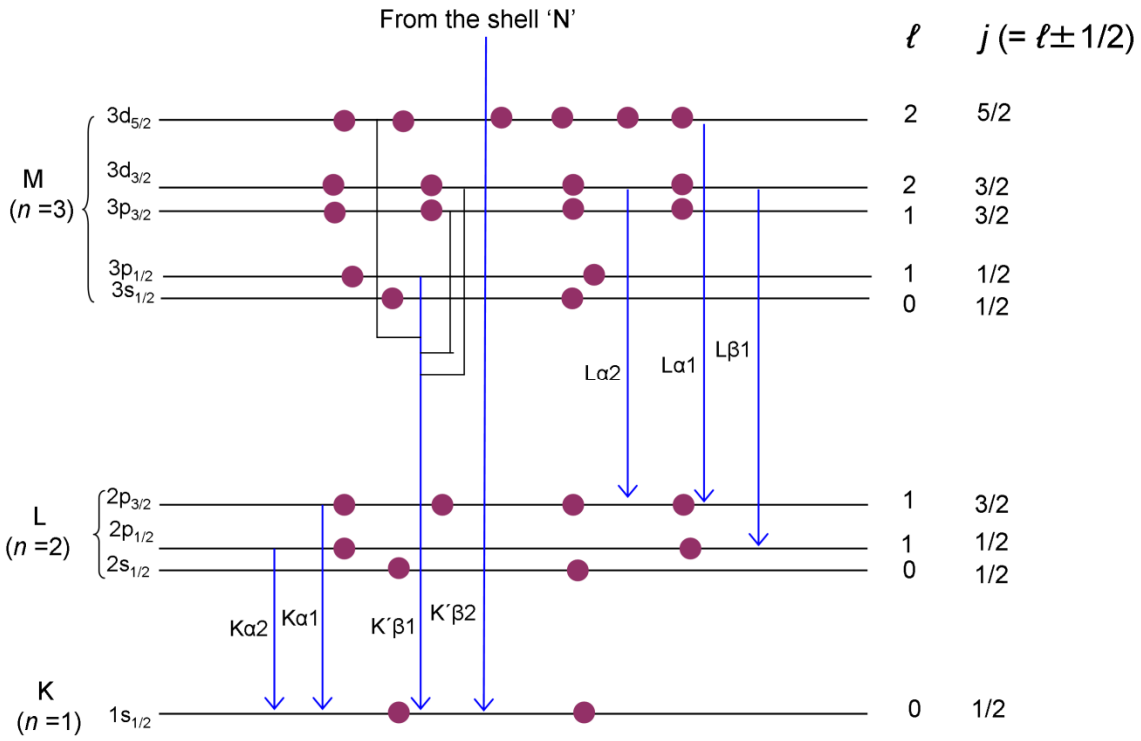

Figure 1.2 Examples of transitions giving rise to some characteristic fluorescence emission lines. The K´β1 and K´β2 respectively represent combinations of all the M to K and N to K transitions.

Figure 1.3 shows a schematic diagram for the experimental setup of a typical XFI experiment. In the experiment, incident X-rays pass through a focusing optic, such as a Kirkpatrick-Baez (K-B) mirror pair,[6] producing a microfocused beam. The microfocused beam then passes through an ion chamber I_0, which measures the intensity of incident beam falling onto the sample. The experimental sample sits on an XY motorized stage, which allows rastering of the sample along two perpendicular directions. When the microfocused incident beam interrogates a sample, the emitted fluorescence is monitored by an energy dispersive detector, which facilitates obtaining a plot of the intensity of photons emanating from the sample as a function of emitted energy. The experiment records a full X-ray fluorescence spectrum at each scan point. The elemental maps are then obtained by integrating over the spectral regions of interest corresponding to specific elemental X-ray fluorescence lines. The ion chamber, I_T is for measuring the transmitted intensity, which is measurable only if the incident X-rays are not overly attenuated by the sample thickness or substrate. In addition, other equipment such as a

cooling stage could make measuring transmitted beam impossible. Figure 1.4 shows an example detector output spectrum from an archaeological bone sample. The spectrum was obtained using a single element silicon drift detector in a spoked channel array (section 2.2.2) based confocal XFI experiment (section 2.4.2). The K_α and K_β peaks respectively represent the convolution of all K_α and K_β lines, which cannot be resolved in a typical XFI experiment.

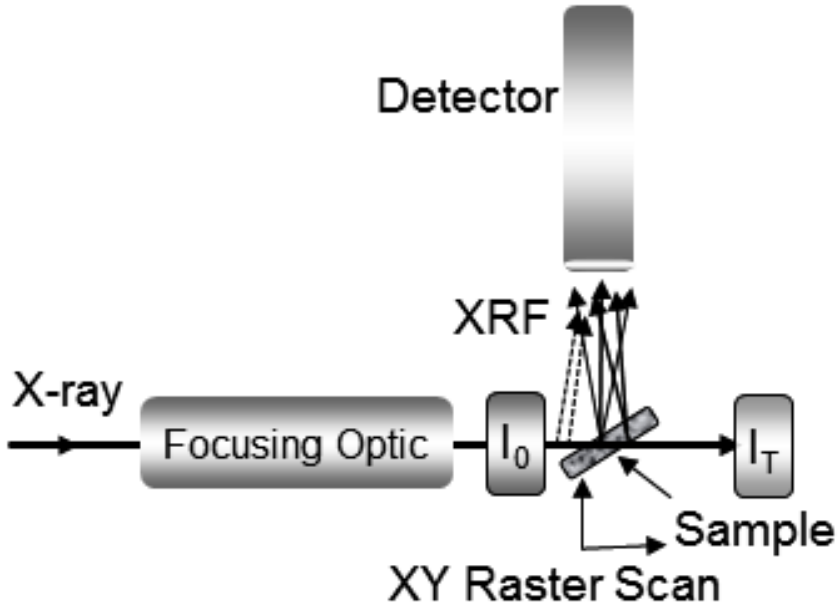

Figure 1.3 A simplified schematic diagram displaying the experimental setup of an XFI experiment. The incident X-rays are focused by a focusing optic before being placed on sample. The ion chamber, I_0 measures incident beam intensity. The sample is mounted at 45˚ to the incident X-ray beam and detector. The ion chamber, I_T measures transmitted intensity. Arrows show that X-ray fluorescence (XRF) emitted along the incident X-ray beam path, both inside (solid arrows) and outside (dotted arrows) the sample, can be registered as long as fall within the detector solid angle.

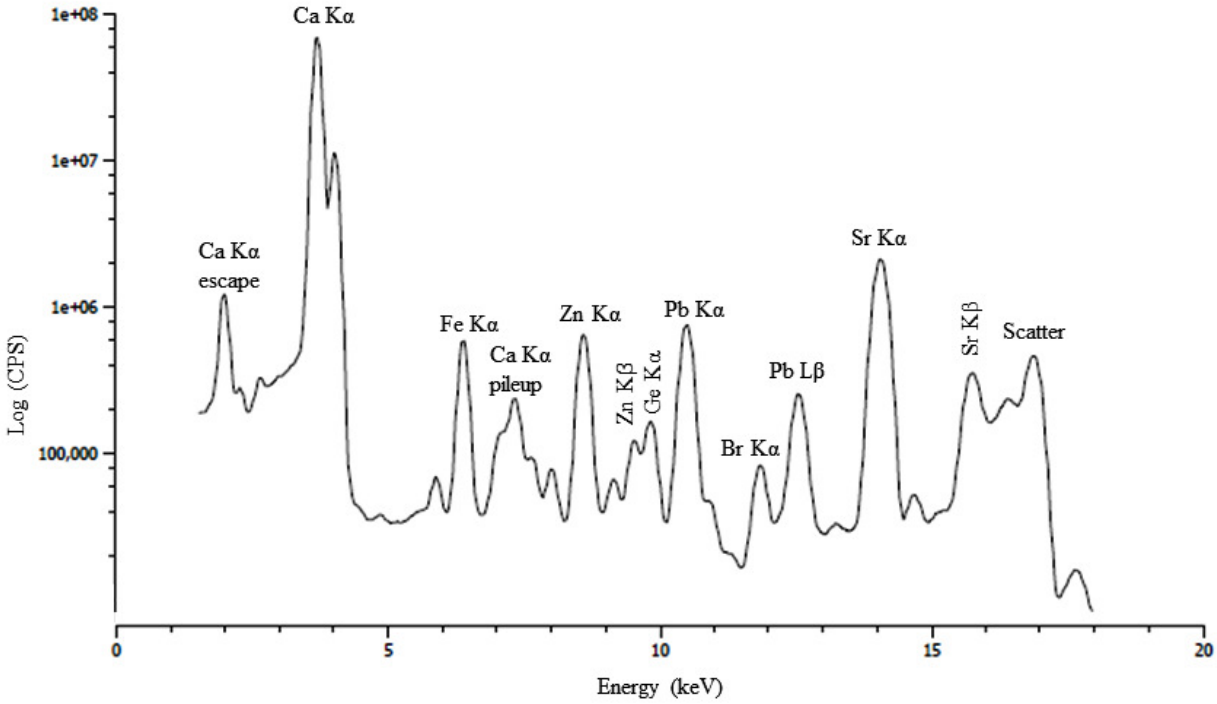

Figure 1.4 An example detector output spectrum plotted with the logarithmic counts per second (CPS) in the ordinate. The data in this example are collected from a bone sample using an energy dispersive silicon-drift vortex detector at excitation energy of 16.999 keV.

1.2 X-ray Absorption Spectroscopy

X-ray absorption spectroscopy (XAS) is a widely used technique for determining the chemical speciation and local coordination environment information of an absorbing atom.[7–13] XAS measures the energy dependency of the X-ray absorption coefficient of an element while the incident X-ray energy is scanned from below to above the binding energy of a core electron.[8,9] When the incident energy is just enough to excite a core electron, the photo-electron is excited to the unoccupied bound states of the absorbing atom leading to a sharp increase of the absorption coefficient at a particular X-ray energy corresponding to the energy difference between the core level and unoccupied state. This phenomenon gives rise to the first part of an XAS spectrum (Figure 1.5), which is within about 50 eV of the absorption edge, often known as X-ray absorption near edge structure (XANES). At higher incident X-ray energies, the photo electron is promoted to a free or continuum state, where it is considered as a photo-electron wave. This wave propagates outward and is backscattered by the neighboring atoms, leading to

constructive or destructive interference as a function of energy.[9] This phenomenon gives rise to the oscillatory part of the spectrum (Figure 1.5), often known as Extended X-ray absorption fine structure (EXAFS).[9] XAS is an element specific technique; the characteristic absorption edge energies are well-known and tabulated.[5] Besides element specificity, XAS offers nondestructive investigation of any phases of materials with no or minimal sample preparation.

An XAS experiment requires a tunable source, typically provided by a synchrotron source. XAS can be carried out with a microfocused beam using the same setup as XFI. Whereas XFI employs a fixed incident energy while scanning the sample position, the XAS uses a fixed sample position while scanning the incident energy. Typically XAS is recorded following the completion of an XFI map, although faster detectors allow the collection of effectively an XAS spectrum at each pixel at some synchrotrons. The XAS data collection is performed by measuring the intensity of either the transmitted X-rays through the sample, or the fluorescent X-rays emitted off the sample as a result of the decay of higher level electrons to the core holes. The former is measured using an ion chamber, I_T while the latter is measured using a fluorescence detector, as shown in Figure 1.3. Monitoring X-ray transmission is the useful technique for concentrated samples while fluorescence based measurements are valid and useful in the thin-dilute limit due to greater sensitivity.[9] While the XANES yields information about the electronic structure, such as oxidation state, the EXAFS provides physical information such as coordination number, interatomic distances, and size (atomic number) of neighboring atoms.[9]

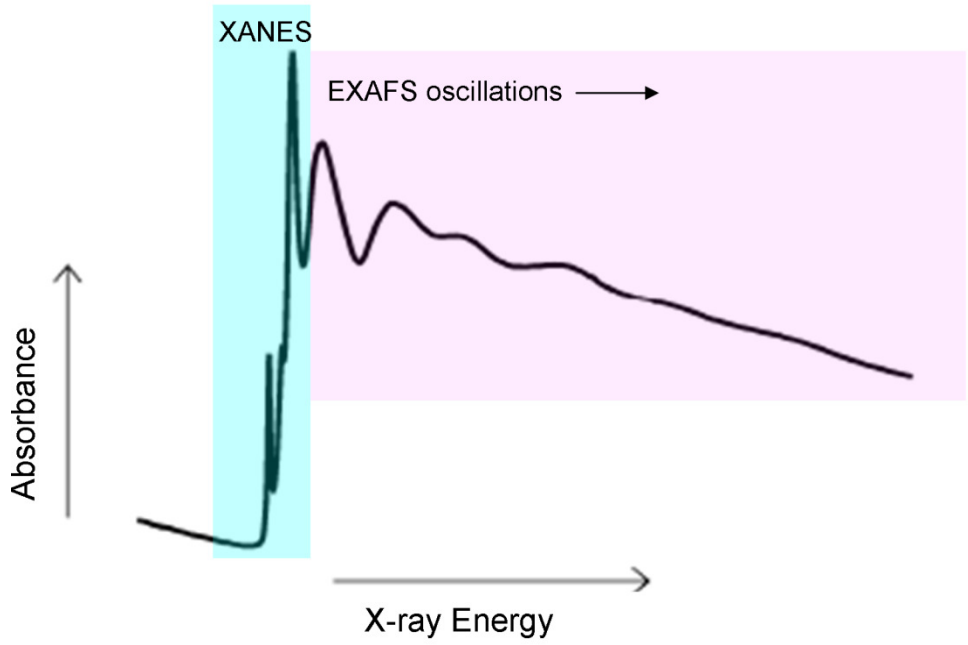

Figure 1.5 An example XAS spectrum showing the XANES and EXAFS regions. The spectrum is adapted from the course materials of Geol 898: Synchrotron Hard X-ray XAS provided by G. N. George and I. J. Pickering in the University of Saskatchewan.

1.3 Confocal X-ray Fluorescence Imaging

Confocal X-ray fluorescence imaging (CXFI)[14] is an innovative variant of the conventional XFI technique described in section 1.1. Just as confocal optical microscopy has revolutionized optical microscopy,[15] CXFI has the potential to revolutionize conventional XFI. In the confocal mode, an additional focusing optic is installed upstream of an energy-dispersive detector in order to restrict the detection of fluorescence to the focal spot of that focusing optic. Thus in the confocal scenario, although excitation happens everywhere along the beam path, detection only occurs where the incident beam focusing spot and the detector optic focusing spot converge in what is known as the confocal volume.[14,16] The strength of the confocal technique arises from its ability to resolve all three spatial dimensions that facilitates using a thick or intact sample in the experiment.[17] Best spatial resolution in a conventional XFI experiment requires samples to be thinned to a thickness approximately equal to the beam spot size, which is achieved through the physical sectioning of the sample to a thickness of only few microns.[18–20] If the sample is not sufficiently thin, then the conventional XFI results in blurry images due to the

superposition of fluorescence originating from the penetrated path of incident X-rays (chapter 4). In contrast, CXFI is capable of resolving all three dimensions; which lead to the ability to select a particular plane within a thick sample, often referred to as optical sectioning. Hence, CXFI avoids the need for physical thin sectioning of the sample. The ability to avoid physical sectioning offers many advantages, such as maintaining the sample integrity, the nondestructive study of valuable samples for which sectioning is not desirable and the freedom of investigating elements in any location within a thick or intact sample. The maximum depth that can be probed within a sample is dictated by the element to be imaged. For example, a low Z element cannot be imaged in the middle of a thick sample due to a small critical depth (discussed below).

Figure 1.6 schematically shows how a CXFI experimental arrangement differs from a conventional XFI setup. Similar to conventional XFI, CXFI also employs an incident focusing optic such as a K-B mirror pair and ion chamber I_0 in order to produce a microfocused beam and to measure incident intensity. In CXFI, the experimental sample sits on an XYZ motorized stage, which allows the rastering of a sample along all three perpendicular directions so that a spot of interest within the sample can be resolved in three dimensions. Unlike conventional XFI, a CXFI experiment implements a focusing optic on the detection side so that the depths from which fluorescence are being originated can be identified. Generally, a polycapillary[21,22] mounted in front of the detector is the approach that is overwhelmingly used. Figure 1.7 shows how a probing volume or confocal volume (V_c) is generated in a CXFI experiment through the intersection of the focal spots of the incident and detection focusing optics.[23] This confocal volume, which is the key to the confocal setup, is determined by the focal spot sizes of the focusing optics involved.[23] To obtain elemental distribution below the surface, the confocal volume is moved into the desired depth inside the sample and an XY map is collected. The confocal method thus achieves optical sectioning of a sample. For generating three dimensional views of elemental distributions, a series of XY maps collected at sequential depth positions is stacked and combined. In the confocal method, one can go deeper and deeper into the sample until the critical depth is reached. The critical depth is the depth from which no fluorescence will be able to reach the detector due to the complete attenuation caused by the overlying thickness of sample. The critical depth depends on the sample matrix and the energy of fluorescent X-rays. In a CXFI experiment (applies to conventional XFI as well), both the incident and fluorescent X-

rays will be attenuated due to penetration through the sample matrix.[24] In principle, these attenuation effects can be modeled by knowing the composition of the sample matrix.[17,24,25]

The collimated detection in CXFI, achieved by the implementation of an additional focusing optic on the detection side, results in a higher signal to noise ratio in the collected data through a significant reduction in background counts.[26–28] Figure 1.6 demonstrates that a conventional XFI experiment detects X-rays (scatter and fluorescence) essentially from anywhere along the beam path, such as the whole depth of the sample (as long as not attenuated), some air, windows and sample mounting slides. In contrast, a CXFI experiment accepts X-rays solely from the confocal volume. This collimated detection results in a significantly less intense scattering peak (Figure 1.8), which comprises scattered signals only from the confocal volume. The high signal to noise ratio in the multiple channel analyzer (MCA) spectrum enables better detection of the minor peaks in the detector output spectrum, hence increased sensitivity.[29] Moreover, since a CXFI scatter map is constructed by the signals collected only from the probing volume within sample, it may facilitate visualizing sample structure as obtained in conventional histology.

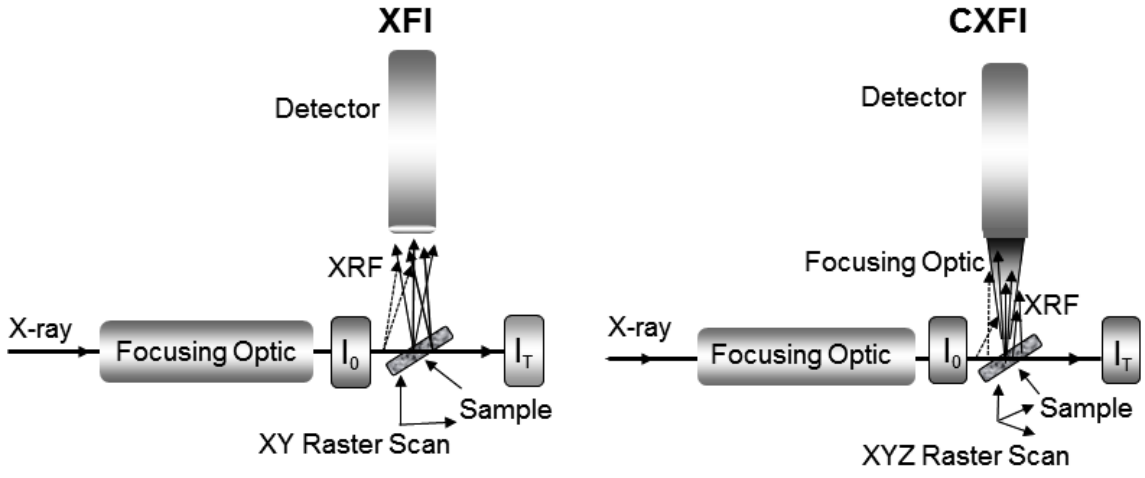

Figure 1.6 A diagram comparing the experimental setup between conventional XFI and CXFI. Unlike conventional XFI, CXFI has an additional focusing optic mounted in front of the detector. This difference results in collection of X-ray fluorescence (XRF) only from the region of the sample where the foci of the detection focusing optic intersect that of the incident.

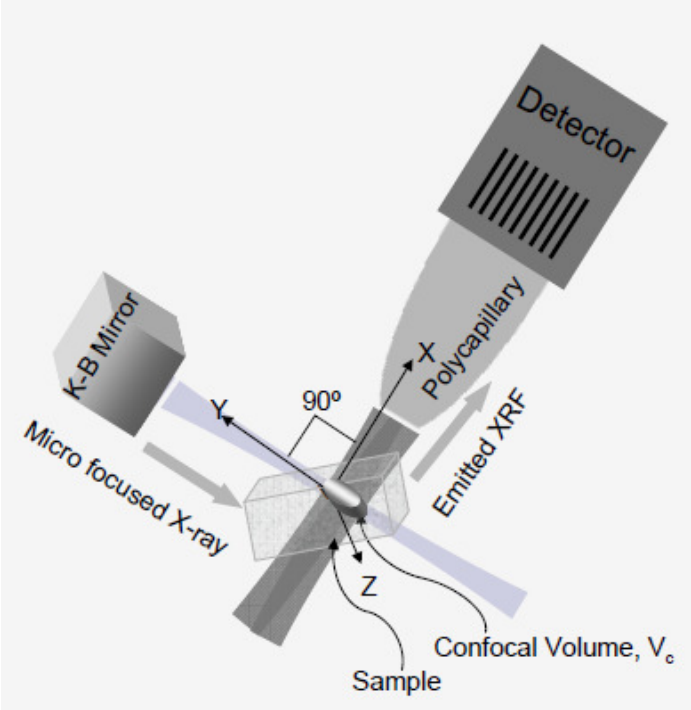

Figure 1.7 Formation of the confocal volume (Vc) within a sample in CXFI. The intersection of the foci of incident (K-B mirror) and detection (polycapillary) focusing optics forms an ellipsoidal volume, known as confocal volume (Vc).

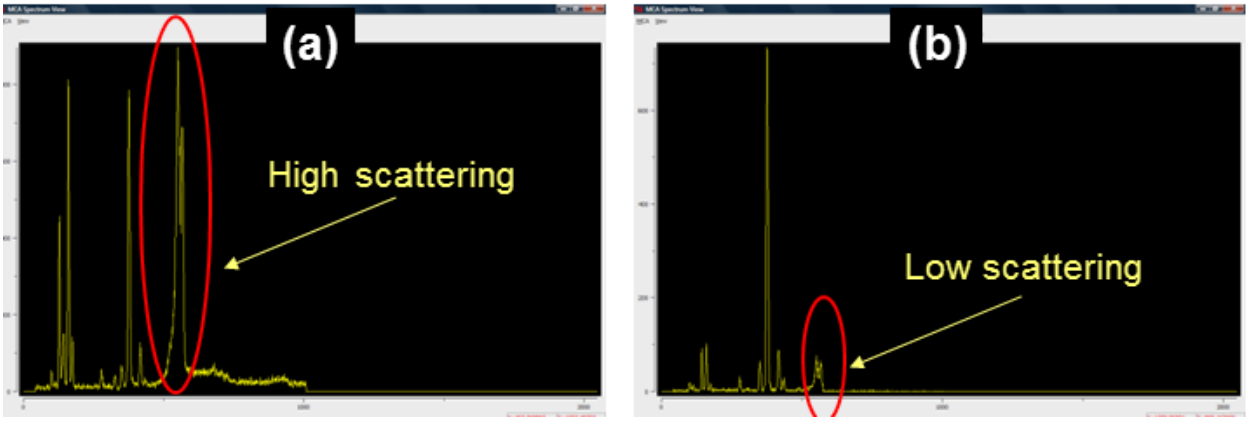

Figure 1.8 Comparison of the scatter peak intensities between conventional XFI (a) and CXFI (b). Spectra collected from a hair sample. Conventional XFI shows substantially higher intensity compared to the CXFI.

1.4 Confocal X-ray Absorption Spectroscopy

A confocal arrangement offers the benefit of studying the localized chemical form of elements in a three dimensionally resolved micro-volume within a sample through the implementation of confocal X-ray absorption spectroscopy (CXAS).[23] In a CXAS experiment, a fluorescence map is first collected using CXFI and then motors are driven to the specific locations of interest chosen from the map. Then a spectrum is collected from those locations by tuning the energy of excitation X-ray beam.[23,27,28] This method of collecting XAS is particularly useful if micron-scale heterogeneity is expected in the chemical form of elements within a sample. In a conventional XFI experiment, an XAS measurement following an XFI may be challenging due to the high background from the substrate upon which the extremely thin sample is mounted. Such background poses a major difficulty especially when a dilute sample is concerned. Since confocal detection is localized, a greater degree of confidence with respect to localization can be expressed and the scatter contribution to the total integrated detector signal is now limited to scatter only produced from within the confocal volume.[27] The other great aspect of CXAS is that it allows browsing through a three dimensional sample for the nondestructive determination of localized chemical form of elements. Examples of CXAS making use of polycapillary and spoked channel array optics are presented in chapters 3, 5 and 6 of this thesis.

1.5 Advantages of Confocal Approach

There are many advantages of employing the confocal approach in imaging or spectroscopy. Some of the leading benefits are described in the following paragraphs.

Ability to use thick or intact sample: In the confocal technique, a probing volume is created within the sample whose three dimensional rastering throughout the sample results in maps of elemental distribution. Such capability enables optical sectioning of the sample and hence, allows the use of a thick or intact sample. The ability to use an intact sample allows the maintenance of sample integrity - a particularly useful capability when dealing with samples prone to contamination. Also, the process of thin sectioning of a sample is not always easy, especially when a tiny feature or serial sections of the sample are of interest. An important tiny part of the sample can be easily missed during serial sectioning. Furthermore, sometimes

samples are fragile or a one of a kind precious one, when thin sectioning is either not possible or desirable.

Three dimensional elemental distributions: CXFI allows investigation of elemental distributions in three dimensions from an un-stained, un-thinned, and intact sample. Studying three dimensional elemental distributions is also possible in a fluorescence tomography experiment,[30,31] in which a sample is rotated and rastered to yield a sinogram, which can in turn be subjected to tomographic reconstruction[32] of a cross-sectional slice of the object. The sample is then vertically translated to collect another cross-sectional slice. The sequential cross-sectional slices are then stacked to generate the three dimensional viewing of the elemental distribution.[33] While CXFI and tomography both have particular benefits, CXFI may be favored when both are applicable as alternatives. This is because the confocal measuring mode readily collects pixel by pixel data and does not require reconstruction algorithms to obtain spatially resolved results. Additionally, CXFI offers the selection of a specific spatial region of interest, thus allowing the analysis of a small area within a larger specimen.

Three dimensionally resolved speciation: One of the important strengths of the confocal technique is that the probing volume can also be used for localized chemical speciation of elements by employing CXAS. Such determination can greatly benefit the study of elements in microscopically inhomogeneous samples. The conventional geometry lacks the ability of localized speciation due to the background noise from the substrate upon which the thinned sample is mounted. Moreover, such speciation is highly complicated in a tomography experiment as it would require reconstruction of spectra from multiple angles.

Higher signal to noise ratio: In CXFI, a detector collects fluorescence only from the probing volume and rejects all other fluorescence arising from sample, air, or beamline components. Such a superior rejection of background can be viewed in Figure 1.8, in which the intensity of the scatter peak is significantly reduced in confocal detection. This superior rejection of the scatter signal greatly helps the detector dead time effect, thus allowing a significant increase in the incident flux on sample compared to conventional XFI. The increased incident flux results in a higher intensity count, consequently yielding a higher detection sensitivity; this

is particularly useful when studying a dilute sample. Also, in the case of an XAS experiment when the scatter peak is close to the peak of interest, a confocal measurement is always advantageous since the windowed counts are significantly less affected by the scatter contribution.

1.6 Developments and Applications of Confocal X-ray Techniques

The fundamental principle of CXFI was proposed by Gibson and Kumakhov in 1992, as one of the applications of polycapillary optics.[34] Later, in 2000, a practical demonstration of CXFI was presented by Ding *et al.* in which a confocal arrangement was employed to achieve improved detection sensitivity.[21] The implementation of CXFI for achieving three dimensional elemental distribution did not happen until 2003, when Kanngießer *et al.* employed it in studying paint layers in ancient Indian Mughal miniatures.[35] This pioneering experiment was performed at BAMline, BESSY II, in which major and minor elements were detected with a depth resolution of 10µm in paint layers. Since then, CXFI using either a synchrotron or a laboratory based setup slowly began to appear.

X-ray sources: CXFI experiments have been realized at several synchrotron facilities. While European synchrotrons are the major players in this field, a few have also been reported from other synchrotrons of the world. Beamlines in which CXFI have been available include, BAMline and mySpot beamlines at Berliner Elektronenspeichering für Synchrotronstrahlung II (BESSY II, Berlin, Germany),[35] ID18F micro-fluorescence end station and other beamlines at European Synchrotron Radiation Facility (ESRF, Grenoble, France),[26] beamline L at Hamburger Synchrotronstrahlungslabor (HASYLAB, Hamburg, Germany),[14] G line at Cornell high-energy synchrotron source (CHESS, Ithaca, NY, USA),[16] Fluo Topo beamline at Angströmquelle Karlsruhe (ANKA, Karlsruhe, Germany),[36] beam line 4W1B-XRF at Beijing Synchrotron Radiation Facility (BSRF, Beijing, China),[37] and D09B beamline at Laboratorio Nacional de Luz Syncrotron (LNLS, São Paulo, Brazil).[38] This thesis has introduced CXFI at the 20ID-B beamline at Advanced Photon Source (APS, Argonne, IL, USA).[27,28,39] As a long term goal of this thesis, the BioXAS beamline at Canadian Light Source (CLS) will also have CXFI available in the near future. Although synchrotron facilities are the most desirable place for CXFI due to high brightness, monochromaticity, and tunable nature of X-rays, laboratory based alternatives

also have evolved due to limited availability of synchrotron beamtime. Examples of laboratory based CXFI can be found in Havrilla *et al.,*[40] Kanngießer *et al.,*[41] Tsuji *et al.*,[42,43] and Nakano *et al.*[44,45] Although less sensitive, a laboratory based CXFI can produce useful elemental maps, given that the concentration is not too low. The major advantage of a laboratory CXFI is its accessibility; no beamtime proposals are required and data can be collected anytime as desired. Laboratory based setups deploy commercially available X-ray tubes as a source, which have anode spot sizes of several tens of microns. Hence, generally the probing volume achieved in a laboratory setup is larger compared to the one from a synchrotron based set up. Also, the brightness of X-rays obtained from an X-ray tube is much lower compared to the synchrotron. Therefore, a laboratory based setup generally demonstrates lower elemental sensitivity compared to a synchrotron based one. Additionally, synchrotron X-rays are readily tunable while laboratory X-rays are not. Although tunability is not required for imaging, it is a prerequisite for CXAS.

X-ray focusing optics: A CXFI setup uses two focusing X-ray optics, one in the incident side and the other in the detection side, to enable discrimination of the origin of fluorescence photons in three dimensions. A number of incident focusing optics, such as K-B mirrors,[37] monocapillaries,[16] and compound refractive lenses[26] are utilized in synchrotron facilitated experiments, whereas a polycapillary[21] is predominantly employed for a laboratory based setup. An attractive feature of a K-B mirror is that it allows high flexibility of working distance, while offering a micron-size beam-spot whose position is energy-independent. For the detection focusing optic, a polycapillary is the predominantly used optic for both synchrotron and laboratory based experiments. This is because a polycapillary is uniquely well suited for collecting fluorescence from a point-like source and no other optic is able to transport a broad energy range without having to be moved. Also, a polycapillary provides an energy-independent focal distance and collects from a larger solid angle. This thesis has contributed to the development of a new collection optic, the spoked channel array (SCA),[39] which showed an order of magnitude improvement in resolution when compared with the state-of-the-art polycapillaries.[27,39]

Previous applications: The four main uses of the CXFI method which have been demonstrated include depth profiling, probing site selection, three dimensional mapping and localized speciation of elements. Among publications, a significant number have involved the characterization of paint layers.[16,35,41,46,47] These studies were mainly focused in understanding the methodology applied in creating works of art or paintings, the pattern involved in the deterioration of paint layers, and the strategy and process of restoration. Knowledge about the composition of buried layers in paintings is crucial for conservation and restoration. CXFI, in contrast to other techniques, offers non-destructive depth profiling of paint layers from an intact sample – therefore, has been considered to be well suited for cultural heritage applications. Other cultural heritage applications which have employed CXFI include investigation of reverse glass painting to realize depth profiling of mobile elements responsible for corrosion process,[48,49] depth selective mapping of layered paint structures in Japanese lacquerware '*Tamamushi-nuri*',[45] and profile analysis of the color/glaze and glaze/ceramic interfaces in Portuguese polychrome glazed ceramics to understand the manufacturing process.[50] This thesis also has contributed to a cultural heritage application of CXFI, in which the chemical form of iron is investigated in the corrosion layer of a medieval stained glass sample from Paderborn cathedral.[27] CXFI was also implemented in the investigation of some geological samples, such as iron oxide in a polished granite sample,[14] age dating of monazite within rock samples,[51] radioactive particle embedded in sediment,[52] hot particles originated from hydrogen bombs,[53] actinide migration in granite,[54] and inclusions in a diamond sample.[26] In the case of biological samples, the application of CXFI can be very useful as these samples are often prone to contamination and higher penetration depth can be obtained. Some applications of CXFI to plants include: distribution and speciation of Se in onion plants;[55] depth profiling of Ca, K and Fe in the surface coat of a wheat grain;[42] investigation of the distribution of elements in a twig of *Buxus microphylla*;[37] distribution of Ca, Fe, Zn and Cu across virtual cross sections of a root of common duckweed;[56] and Ti, As, Mn and Zn in the skin region of rice.[57] Applications of CXFI to other biological systems include: the study of distributions of lead (Pb) and other relevant metals in skeletal tissues of femoral head and patella;[58] and tissue-specific three-dimensional (3D) distribution of metals in *Daphnia magna*.[17] As for CXAS applications, experiments have been reported in two geological samples: Fe K XAS study of mineral inclusions within rare natural diamonds[23] and Np L3 XAS study to determine valence state of Np within granite,[54] and also in a cultural heritage sample: chemical

speciation of the coloring agent in painted tiles.[59] This thesis has contributed to the publication of first biological CXAS, in which the chemical form of Se is investigated in zebrafish eye lens.[28]

Limitations of CXFI: A major limitation of confocal method can be its limited probe depth (dependent on the sample matrix and the energy of X-ray fluorescence line of interest). This implies to the maximum depth can be probed into the sample before the detected X-ray fluorescence reaches too low to be considered meaningful. The application of confocal mode can also be limited due to its shorter working distance, which is especially relevant when the confocal setup is constructed based on a spoked channel array device (section 2.2.2) for which the value of working distance is only a few hundred microns. While doing three dimensional mapping of a volume of interest, a long measuring time, which could easily stretch to a non-reasonable amount, can be another drawback of CXFI. However, this can be largely overcome by the introduction of so called on-the-fly scanning mode in the synchrotron beamlines, in which the overhead produced in the step scanning mode from the time it takes to start and stop the motors at each step is eliminated. Another limitation is the complexity of the quantification procedure, arising from the difficulty in simulating accurate heterogeneous sample matrix, energy-dependent probing volume, and attenuation of incident and fluorescent X-rays.[24,60] Other pitfalls include the energy-dependency of depth-resolution and the inability to achieve a depth-resolution smaller than about 10 μm; both of these limitations are linked to the characteristics of a polycapillary detection optic (section 2.2.1).

1.7 Objective of this Research

The BioXAS beamline at CLS is being built as a facility for XAS and XFI of biological systems. Since there is a growing interest in the direct visualization of the three-dimensional distribution of elements in un-stained, un-thinned and intact biological samples, the implementation of CXFI is one of the priorities of BioXAS. However, the challenge lies in the fact that biological samples are often dilute compared to the non-biological ones. Also, biological systems are delicate and tend to suffer from contamination or alteration if sectioned. Furthermore, biological samples often show heterogeneity in elemental distribution and speciation at only a few microns, thus requiring higher depth resolution than the currently available ~10 μm. Therefore, this project was initiated in order to develop CXFI for biological

applications. The 20ID-B beamline at APS, a beamline of Canadian partnership at APS, was proposed as the main venue for this research development since BioXAS was under construction during this project. Specific objectives of this research were as follows.

- To develop a CXFI set up at 20ID-B beamline.
- To verify the feasibility of the setup using biological systems of known results.
- To determine the drawbacks of the setup when studying various sample types.
- To establish possible solutions to the drawbacks.
- To establish better depth resolution.
- To establish a full capability for both CXFI and CXAS.

The long term goal of this project is to implement CXFI at the BioXAS imaging endstation, which would establish an incredible opportunity for distinctive innovations at the Canadian Light Source synchrotron.

1.8 Organization of Thesis Chapters

The main theme of this thesis is the development of CXFI for biological applications. Each chapter in this thesis contributes to this overall theme, while focusing on a specific topic. This section is intended to describe how all chapters unify to construct the theme.

Chapter 1 comprises an introduction and literature review. It describes the concept of the CXFI technique, how CXFI works, and what its specialties are. The literature review provides a concise summary of synchrotron and laboratory based CXFI experiments, relevant X-ray optics, application and limitation of CXFI technique; thus presenting the context for this thesis. Finally, chapter 1 states the objective of this research, and the current section presents the transition of the thesis.

Chapter 2 outlines the steps involved in the progress of this research. It provides an account of the initiation of project, evaluation of the results from test experiments, successes and failures. It then presents the progress of this research with regards to incorporating novel X-ray optics and samples.

Chapter 3 was published in the journal *Environmental Science & Technology*.[28] This chapter illustrates the implementation of polycapillary based CXFI and first demonstration of biological CXAS in studying Se distribution and speciation in intact zebrafish larvae. A possible causality between exposure to elevated Se and Se-induced ocular impairments is discussed, since a preferential accumulation of Se is detected in the eye lens of zebrafish larvae.

Chapter 4 was recently accepted in *Archaeometry* (**2016**, In press, DOI: 10.1111/arcm.12232). Based on a polycapillary based CXFI experiment, this chapter illustrates how a confocal approach can be very useful in studying poorly preserved archaeological bones. A comparison with the results from conventional XFI shows that CXFI yields images of higher resolution, which can be insightful in distinguishing biogenic and diagenetic uptake of Pb.

Chapter 5 was published in *Journal of Analytical Atomic Spectrometry*.[27] This chapter demonstrates the first application of a novel focusing optic, the spoked channel array, in studying the oxidation state of Fe in the corrosion layer of a medieval stained glass sample using CXFI and CXAS. The advantages of employing spoked channel arrays include an improved spatial resolution and an energy-independent probing volume. The first implementation of a spoked channel array optic was demonstrated in a non-biological system, since biological samples are challenging as a test sample due to low concentration.

Chapter 6 illustrates the first application of the novel spoked channel array optic in collecting high resolution elemental maps and highly localized spectroscopic information from archeological human bone, a biological sample. This chapter presents the visualization of cellular spaces in bone (lacunae), and highly localized CXAS.

Chapter 7 is the concluding chapter of this thesis. It revisits the main findings of this project and links the drawn conclusions to the overall goal of this thesis. A comparative discussion between the two detection focusing optics, polycapillary and spoked channel arrays, is presented and directions for future research are identified.

1.9 References

(1) Pushie, M. J.; Pickering, I. J.; Korbas, M.; Hackett, M. J.; George, G. N. Elemental and chemically specific X-ray fluorescence imaging of biological systems. *Chem. Rev.* **2014**, *114*, 8499–8541.

(2) Winick, H. *Synchrotron Radiation Sources — A Primer*; World Scientific: New Jersey, 1995.

(3) Müller, R. O. *Spectrochemical Analysis by X-Ray Fluorescence*; Springer US: NewYork, 1972.

(4) Ellis, A. M. Spectroscopic selection rules : the role of photon states. *J. Chem. Educ.* **1999**, *76*, 1291–1294.

(5) Thompson, A.; Attwood, D.; Gullikson, E.; Howells, M.; Kim, K.-J.; Kirz, J.; Kortright, J.; Lindau, I.; Liu, Y.; Pianetta, P.; Robinson, A.; Scofield, J.; Underwood, J.; Williams, G.; Winick, H. *X-Ray Data Booklet*; Center for X-ray Optics and Advanced Light Source, Lawrence Berkeley Laboratory, Berkeley, 2009.

(6) Kirkpatrick, P.; Baez, A. V. Formation of optical images by X-Rays. *J. Opt. Soc. Am.* **1948**, *38*, 766–773.

(7) Cotelesage, J. J. H.; Pushie, M. J.; Grochulski, P.; Pickering, I. J.; George, G. N. Metalloprotein active site structure determination: synergy between X-ray absorption spectroscopy and X-ray crystallography. *J. Inorg. Biochem.* **2012**, *115*, 127–137.

(8) Yano, J.; Yachandra, V. K. X-ray absorption spectroscopy. *Photosynth. Res.* **2009**, *102*, 241–254.

(9) George, G. N.; Pickering, I. J. X-ray absorption spectroscopy in biology and chemistry. In *V. Tsakanov, H. Wiedemann (Eds.), Brilliant Light in Life and Materials Sciences, Springer, Dordrecht, NL,*; 2007; pp 97–119.

(10) George, G. N.; Singh, S. P.; Myers, G. J.; Watson, G. E.; Pickering, I. J. The chemical forms of mercury in human hair: a study using X-ray absorption spectroscopy. *J. Biol. Inorg. Chem.* **2010**, *15*, 709–715.

(11) George, G. N.; MacDonald, T. C.; Korbas, M.; Singh, S. P.; Myers, G. J.; Watson, G. E.; O'Donoghue, J. L.; Pickering, I. J. The chemical forms of mercury and selenium in whale skeletal muscle. *Metallomics* **2011**, *3*, 1232–1237.

(12) Pickering, I. J.; Wright, C.; Bubner, B.; Ellis, D.; Persans, M. W.; Yu, E. Y.; George, G. N.; Prince, R. C.; Salt, D. E. Chemical form and distribution of selenium and sulfur in the selenium hyperaccumulator *Astragalus bisulcatus*[1]. *Plant Physiol.* **2003**, *131*, 1460–1467.

(13) Wilke, M.; Farges, F.; Petit, P.-E.; Brown Jr., G. E.; Martin, F. Oxidation state and coordination of Fe in minerals : An Fe K-XANES spectroscopic study. *Am. Miner.* **2001**, *86*, 714–730.

(14) Janssens, K.; Proost, K.; Falkenberg, G. Confocal microscopic X-ray fluorescence at the HASYLAB microfocus beamline: characteristics and possibilities. *Spectrochim. Acta B* **2004**, *59*, 1637–1645.

(15) Shotton, D. M. Confocal scanning optical microscopy and its applications for biological specimens. *J. Cell Sci.* **1989**, *94*, 175–206.

(16) Woll, A. R.; Mass, J.; Bisulca, C.; Huang, R.; Bilderback, D. H.; Gruner, S.; Gao, N. Development of confocal X-ray fluorescence (XRF) microscopy at the Cornell high energy synchrotron source. *Appl. Phys. A* **2006**, *83*, 235–238.

(17) Samber De, B.; Silversmit, G.; Schamphelaere De, K.; Evens, R.; Schoonjans, T.; Vekemans, B.; Janssen, C.; Masschaele, B.; Hoorebeke Van, L.; Szalóki, I.; Vanhaecke, F.; Rickers, K.; Falkenberg, G.; Vincze, L. Element-to-tissue correlation in biological samples determined by three-dimensional X-ray imaging methods. *J. Anal. At. Spectrom.* **2010**, *25*, 544–553.

(18) Korbas, M.; Krone, P. H.; Pickering, I. J.; George, G. N. Dynamic accumulation and redistribution of methylmercury in the lens of developing zebrafish embryos and larvae. *J. Biol. Inorg. Chem.* **2010**, *15*, 1137–1145.

(19) Korbas, M.; Blechinger, S. R.; Krone, P. H.; Pickering, I. J.; George, G. N. Localizing organomercury uptake and accumulation in zebrafish larvae at the tissue and cellular level. *Proc. Natl . Acad. Sci . U. S. A.* **2008**, *105*, 12108–12112.

(20) Korbas, M.; Lai, B.; Vogt, S.; Gleber, S.-C.; Karunakaran, C.; Pickering, I. J.; Krone, P. H.; George, G. N. Methylmercury targets photoreceptor outer segments. *ACS Chem. Biol.* **2013**, *8*, 2256–2263.

(21) Ding, X.; Gao, N.; Havrilla, G. Monolithic polycapillary X-ray optics engineered to meet a wide range of applications. *Proc. SPIE* **2000**, *4144*, 174.

(22) MacDonald, C. A. Focusing polycapillary optics and their applications. *X-Ray Opt. Instrum.* **2010**, *2010*, 1–17.

(23) Silversmit, G.; Vekemans, B.; Nikitenko, S.; Schmitz, S.; Schoonjans, T.; Brenker, F. E.; Vincze, L. Spatially resolved 3D micro-XANES by a confocal detection scheme. *Phys. Chem. Chem. Phys.* **2010**, *12*, 5653–5659.

(24) Mantouvalou, I.; Malzer, W.; Kanngießer, B. Quantification for 3D micro X-ray fluorescence. *Spectrochim. Acta B* **2012**, *77*, 9–18.

(25) Kanngießer, B.; Malzer, W.; Mantouvalou, I.; Sokaras, D.; Karydas, A. G. A deep view in cultural heritage—confocal micro X-ray spectroscopy for depth resolved elemental analysis. *Appl. Phys. A* **2012**, *106*, 325–338.

(26) Vincze, L.; Vekemans, B.; Brenker, F. E.; Falkenberg, G.; Rickers, K.; Somogyi, A.; Kersten, M.; Adams, F. Three-dimensional trace element analysis by confocal X-ray microfluorescence imaging. *Anal. Chem.* **2004**, *76*, 6786–6791.

(27) Choudhury, S.; Hormes, J.; Agyeman-Budu, D. N.; Woll, A. R.; George, G. N.; Coulthard, I.; Pickering, I. J. Application of a spoked channel array to confocal X-ray fluorescence imaging and X-ray absorption spectroscopy of medieval stained glass. *J. Anal. At. Spectrom.* **2015**, *30*, 759–766.

(28) Choudhury, S.; Thomas, J. K.; Sylvain, N. J.; Ponomarenko, O.; Gordon, R. A.; Heald, S. M.; Janz, D. M.; Krone, P. H.; Coulthard, I.; George, G. N.; Pickering, I. J. Selenium preferentially accumulates in the eye lens following embryonic exposure: A confocal X-ray fluorescence imaging study. *Environ. Sci. Technol.* **2015**, *49*, 2255–2261.

(29) Wilke, M.; Appel, K.; Vincze, L.; Schmidt, C.; Borchert, M.; Pascarelli, S. A confocal set-up for micro-XRF and XAFS experiments using diamond-anvil cells. *J. Synchrotron Radiat.* **2010**, *17*, 669–675.

(30) Golosio, B.; Simionovici, A.; Somogyi, A.; Lemelle, L.; Chukalina, M.; Brunetti, A. Internal elemental microanalysis combining X-ray fluorescence, compton and transmission tomography. *J. Appl. Phys.* **2003**, *94*, 145–156.

(31) Lombi, E.; de Jonge, M. D.; Donner, E.; Kopittke, P. M.; Howard, D. L.; Kirkham, R.; Ryan, C. G.; Paterson, D. Fast X-ray fluorescence microtomography of hydrated biological samples. *PLoS One* **2011**, *6*, 1–5.

(32) La Rivière, P. J.; Billmire, D.; Vargas, P.; Rivers, M.; Sutton, S. R. Penalized-likelihood image reconstruction for X-ray fluorescence computed tomography. *Opt. Eng.* **2006**, *45*, 077005–1 – 077005–077010.

(33) Jonge, M. D. De; Holzner, C.; Baines, S. B.; Twining, B. S.; Ignatyev, K.; Diaz, J.; Howard, D. L.; Legnini, D.; Miceli, A.; Mcnulty, I.; Jacobsen, C. J.; Vogt, S. Quantitative 3D elemental microtomography of *Cyclotella meneghiniana* at 400-nm resolution. *Proc. Natl . Acad. Sci . U. S. A.* **2010**, *107*, 15676–15680.

(34) Gibson, W. M.; Kumakhov, M. A. Applications of X-ray and neutron capillary optics. *Proc. SPIE* **1992**, *1736*, 172.

(35) Kanngießer, B.; Malzer, W.; Reiche, I. A new 3D micro X-ray fluorescence analysis set-up – First archaeometric applications. *Nucl. Instrum. Meth. B* **2003**, *211*, 259–264.

(36) Leroy, S.; Simon, R.; Bertrand, L.; Williams, A.; Foy, E.; Dillmann, P. First examination of slag inclusions in medieval armours by confocal SR-μ-XRF and LA-ICP-MS. *J. Anal. At. Spectrom.* **2011**, *26*, 1078–1087.

(37) Sun, T.; Ding, X.; Liu, Z.; Zhu, G.; Li, Y.; Wei, X.; Chen, D.; Xu, Q.; Liu, Q.; Huang, Y.; Lin, X.; Sun, H. Characterization of a confocal three-dimensional micro X-ray fluorescence facility based on polycapillary X-ray optics and Kirkpatrick–Baez mirrors. *Spectrochim. Acta B* **2008**, *63*, 76–80.

(38) Perez, R. D.; Sánchez, H. J.; Perez, C. A.; Rubio, M. Latest developments and opportunities for 3D analysis of biological samples by confocal μ-XRF. *Radiat. Phys. Chem.* **2010**, *79*, 195–200.

(39) Woll, A. R.; Agyeman-Budu, D.; Choudhury, S.; Coulthard, I.; Finnefrock, A. C.; Gordon, R.; Hallin, E.; Mass, J. Lithographically-fabricated channel arrays for confocal X-ray fluorescence microscopy and XAFS. *J. Phys. Conf. Ser.* **2014**, *493*, 012028 (1–4).

(40) Havrilla, G. J.; Miller, T. Micro X-ray fluorescence in materials characterization. *Powder Diffr.* **2012**, *19*, 119–126.

(41) Kanngießer, B.; Malzer, W.; Rodriguez, A. F.; Reiche, I. Three-dimensional micro-XRF investigations of paint layers with a tabletop setup. *Spectrochim. Acta B* **2005**, *60*, 41–47.

(42) Tsuji, K.; Nakano, K.; Ding, X. Development of confocal micro X-ray fluorescence instrument using two X-ray beams. *Spectrochim. Acta B* **2007**, *62*, 549–553.

(43) Tsuji, K.; Nakano, K. Development of confocal 3D micro-XRF spectrometer with dual Cr – Mo excitation. *X-ray Spectrom.* **2007**, *36*, 145–149.

(44) Nakano, K.; Tsuji, K. Development of laboratory confocal 3D-XRF spectrometer and nondestructive depth profiling. *J. Anal. At. Spectrom.* **2010**, *25*, 562–569.

(45) Nakano, K.; Tsuji, K. Nondestructive elemental depth profiling of Japanese lacquerware "Tamamushi-nuri" by confocal 3D-XRF analysis in comparison with micro GE-XRF. *X-ray Spectrom.* **2009**, *38*, 446–450.

(46) Wei, X.; Lei, Y.; Sun, T.; Lin, X.; Xu, Q.; Chen, D.; Zou, Y.; Jiang, Z.; Huang, Y.; Yu, X.; Ding, X.; Xu, H. Elemental depth profile of faux bamboo paint in Forbidden City studied by synchrotron radiation confocal μ-XRF. *X-ray Spectrom.* **2008**, *37*, 595–598.

(47) Faubel, W.; Simon, R.; Stefan, H.; Friedrich, F.; Weidler, P. G.; Becker, H.; Schmidt, W. Protrusions in a painting by Max Beckmann examined with confocal μ-XRF. *J. Anal. At. Spectrom.* **2011**, *26*, 942–948.

(48) Kanngießer, B.; Mantouvalou, I.; Malzer, W.; Wolff, T.; Hahn, O. Non-destructive, depth resolved investigation of corrosion layers of historical glass objects by 3D Micro X-ray fluorescence analysis. *J. Anal. At. Spectrom.* **2008**, *23*, 814–819.

(49) Mantouvalou, I.; Lange, K.; Wolff, T.; Grötzsch, D.; Lühl, L.; Haschke, M.; Hahn, O.; Kanngießer, B. A compact 3D micro X-ray fluorescence spectrometer with X-ray tube excitation for archaeometric applications. *J. Anal. At. Spectrom.* **2010**, *25*, 554–561.

(50) Guilherme, A.; Coroado, J.; dos Santos, J. M. F.; Lühl, L.; Wolff, T.; Kanngießer, B.; Carvalho, M. L. X-ray fluorescence (conventional and 3D) and scanning electron microscopy for the investigation of Portuguese polychrome glazed ceramics: Advances in the knowledge of the manufacturing techniques. *Spectrochim. Acta B* **2011**, *66*, 297–307.

(51) Schmitz, S.; Möller, A.; Wilke, M.; Malzer, W.; Kanngiesser, B.; Bousquet, R.; Berger, A.; Schefer, S. Chemical U-Th-Pb dating of monazite by 3D-Micro X-ray fluorescence analysis with synchrotron radiation. *Eur. J. Miner.* **2009**, *21*, 927–945.

(52) Bielewski, M.; Himbert, J.; Niagolova, N.; Falkenberg, G.; Eriksson, M.; Betti, M. Nondestructive spectrometric study on a radioactive particle embedded in a marine sediment. *Microsc. Microanal.* **2008**, *14*, 321–327.

(53) Jimenez-Ramos, M. C.; Eriksson, M.; García-López, J.; Ranebo, Y.; García-Tenorio, R.; Betti, M.; Holm, E. A comparison of two micro-beam X-ray emission techniques for actinide elemental distribution in microscopic particles originating from the hydrogen bombs involved in the Palomares (Spain) and Thule (Greenland) accidents. *Spectrochim. Acta B* **2010**, *65*, 823–829.

(54) Denecke, M. A.; Brendebach, B.; De Nolf, W.; Falkenberg, G.; Janssens, K.; Simon, R. Spatially resolved micro-X-ray fluorescence and micro-X-ray absorption fine structure study of a fractured granite bore core following a radiotracer experiment. *Spectrochim. Acta B* **2009**, *64*, 791–795.

(55) Bulska, E.; Wysocka, I. A.; Wierzbicka, M. H.; Proost, K.; Janssens, K.; Falkenberg, G. In vivo investigation of the distribution and the local speciation of selenium in *Allium cepa L.* by means of microscopic X-ray absorption near-edge structure spectroscopy and confocal microscopic X-ray fluorescence analysis. *Anal. Chem.* **2006**, *78*, 7616–7624.

(56) Kanngießer, B.; Malzer, W.; Pagels, M.; Lühl, L.; Weseloh, G. Three-dimensional micro-XRF under cryogenic conditions: a pilot experiment for spatially resolved trace analysis in biological specimens. *Anal. Bioanal. Chem.* **2007**, *389*, 1171–1176.

(57) Mihucz, V. G.; Silversmit, G.; Szalóki, I.; Samber, B. De; Schoonjans, T.; Tatár, E.; Vincze, L.; Virág, I.; Yao, J.; Záray, G. Removal of some elements from washed and cooked rice studied by inductively coupled plasma mass spectrometry and synchrotron based confocal micro-X-ray fluorescence. *Food Chem.* **2010**, *121*, 290–297.

(58) Zoeger, N.; Streli, C.; Wobrauschek, P.; Jokubonis, C.; Pepponi, G.; Roschger, P.; Hofstaetter, J.; Berzlanovich, A.; Wegrzynek, D.; Markowicz, A.; Simon, R.; Falkenberg, G. Determination of the elemental distribution in human joint bones by SR micro XRF. *X-ray Spectrom.* **2008**, *37*, 3–11.

(59) Reiche, I.; Röhrs, S.; Salomon, J.; Kanngießer, B.; Höhn, Y.; Malzer, W.; Voigt, F. Development of a nondestructive method for underglaze painted tiles-demonstrated by the analysis of Persian objects from the nineteenth century. *Anal. Bioanal. Chem.* **2009**, *393*, 1025–1041.

(60) Wrobel, P.; Czyzycki, M. Direct deconvolution approach for depth profiling of element concentrations in multi-layered materials by confocal micro-beam X-ray fluorescence spectrometry. *Talanta* **2013**, *113*, 62–67.

CHAPTER 2. Technique Development

2.1 Preface

This chapter introduces the two detector mounted X-ray focusing optics, the traditional polycapillary and novel SCA, used in this research. It then provides an account on the steps of developing CXFI and CXAS configurations at beamline 20ID-B, APS, and discusses success and failures with regards to incorporating novel X-ray optics and samples.

2.2 Detection Focusing Optics

A detector mounted focusing optic is the key element for confocal detection. In a CXFI configuration, a detection focusing optic is installed in the detector snout in order to limit the detection only to the fluorescence originating from the focal spot of that focusing optic. A polycapillary focusing optic[1] is the predominantly used type of focusing optic for confocal detection. Besides implementing a polycapillary focusing optic, this thesis also implemented a novel focusing optic, spoked channel array (SCA),[2] designed and fabricated at CHESS, in order to achieve improved spatial resolution in confocal detection. Following sections present the mechanism of function, advantages and limitations, and scope of application for both the polycapillary and SCA focusing optics.

2.2.1 Polycapillary

A polycapillary optic,[1] comprised of a tapered bundle of thousands of hollow glass tubes designed to collect and redirect the emitted fluorescence into a quasi-parallel beam, is well suited for collecting fluorescence from a point-like source.[3] The glass tubes in the polycapillary are slightly angled towards a common focal point outside the optic as shown in Figure 2.1 (b). Figure 2.1 (c) shows how an X-ray beam is transported through a polycapillary via repeated total external reflections. The total external reflection occurs if the incident angle at each reflection is

less than a critical angle (θ_c), demonstrated in Figure 2.1 (d). Hence, the transmission of X-rays in polycapillary optics is governed by the critical angle (θ_c), which is energy (E) dependent. For a borosilicate glass, the critical angle is approximately,[4]

$$\theta_c(mrad) \approx \frac{30}{E} \qquad \ldots \quad \ldots \quad \ldots (2.1)$$

In a CXFI experimental setup, the available depth resolution is determined by the polycapillary focal spot, which can be estimated from the following relation,[4]

$$S(mm) \approx a.f.\theta_c + d_{out} \qquad \ldots \quad (2.2)$$

Where S is the full width at half-maximum (FWHM) or the diameter of the spot, d_{out} is the individual channel diameter at the capillary tip, θ_c is the critical angle, f is the focal distance and a is an adjustment parameter determined by the optic design and X-ray source property. Since the focal spot size increases with the focal distance, a smaller spot size would result in a shorter focal distance, meaning a shorter working space between the sample and optic. The above relation 2.2 also indicates that the focal spot increases with the critical angle θ_c, which implies that the focal spot of a polycapillary optic decreases with the X-ray energy. Polycapillary optics have been demonstrated to work over a large energy range of up to 30 keV and to collect from a large solid angle of up to 20 degrees.[3] A photograph of a typical polycapillary optic (XOS®) used in the CXFI studies employed in this thesis is shown in Figure 2.1 (a). It offered a focal spot ~ 25 micron (at Mo K_α), working distance ~ 9 mm, and collection angle ~ 20° .

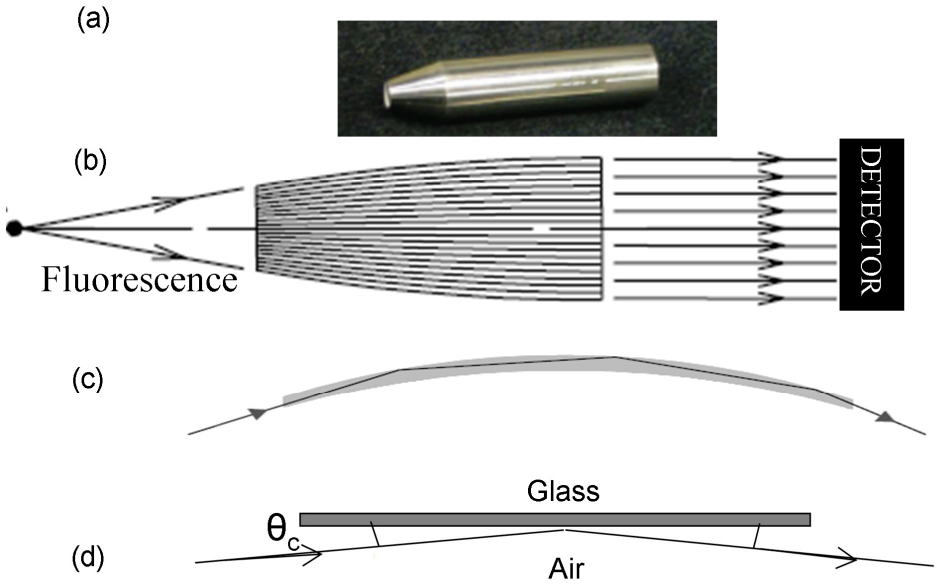

Figure 2.1 Details of focusing using a polycapillary optic. (a) Photograph of the XOS® polycapillary optic. (b) Schematic of how a polycapillary optic achieves its focus. (c) Schematic of the propagation of an X-ray along a capillary tube through multiple total external reflections. (d) Schematic of the critical angle. Parts (b), (c) and (d) are reproduced from reference 4.

2.2.2 Spoked channel array (SCA)

Most (or almost all) XFI reported to date have used polycapillary X-ray optics to define the confocal volume, but this method limits the scope of CXFI due to the limited and energy-dependent depth-resolution. The highest resolution offered by a state-of-the-art XOS® polycapillary is ~8 μm at ~ 17.5 keV with a working distance of ~2 mm, while an improvement in resolution may result in shorter and possibly impractical working distances (equation 2.2). Furthermore, the polycapillary derived resolution is inversely proportional to the X-ray energy (equations 2.1 and 2.2). The best reported polycapillary resolution at the low energy regime (2 - 5 keV) is ~20 μm.[2] To overcome the limitation of spatial resolution imposed by a polycapillary, this thesis implemented a novel focusing optic, a spoked channel array (SCA) designed and fabricated at CHESS.[2] This trapezoidal shaped optic is fabricated via standard lithographic techniques and deep reactive ion etching (DRIE). It consists of an array of rectangular channels, arranged like spokes of a wheel directed to a focal point as shown in the schematic diagram of

Figure 2.2. The X-ray fluorescence emitted from the confocal volume transmits through the collimating channels to the detector. In the limit of zero reflection from the channels, the resolution of the SCA only depends on the length and width of the channels.[2] In the first experimental realization of the SCA optic,[2] three designs with 1, 2, and 5-μm wide channels ranging from 30 to 50 μm in depth and 2 mm in length were tested. A nearly energy-independent depth resolution of ~1.7 μm was achieved for the energy range of 4.5 to 10 keV. This represented an order-of-magnitude improvement over the polycapillary.[2] However, the optics demonstrated a limited practical appeal due to the limited collection efficiency and extremely small working distance of ~0.2 mm. In a later experiment,[5] a new SCA design, in which collimating channels were formed by a staggered array of pillars with side-walls tapered away from the channel axis (Figure 2.3), were tested. The new design resulted in improved collection efficiency and better working distances of up to 1.5 mm (chapter 6), while maintaining excellent spatial resolution.[5] The optics reported in references 2 and 5 were fabricated from silicon, and were thus expected to operate well only up to 12 keV according to ray-tracing simulations. In a recent improvement implemented to the design, SCAs were fabricated from germanium so that the optics can operate well up to 30 keV. Currently, a new design comprising the channel widths up to 50 μm, which may be suitable for using in non-synchrotron based CXFI, is being planned for future fabrication.

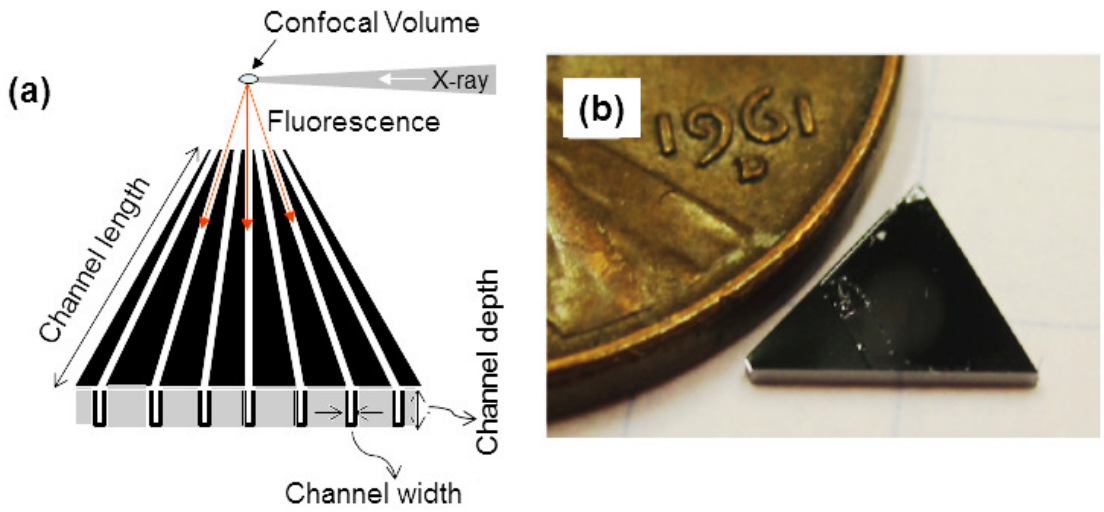

Figure 2.2 The SCA optics. (a) A schematic diagram showing X-ray fluorescence emitted from the confocal volume transmits through the SCA channels, which are shown by the white lines etched on a substrate such as silicon shown in black. (b) Photograph of a SCA optic reproduced from reference 2.

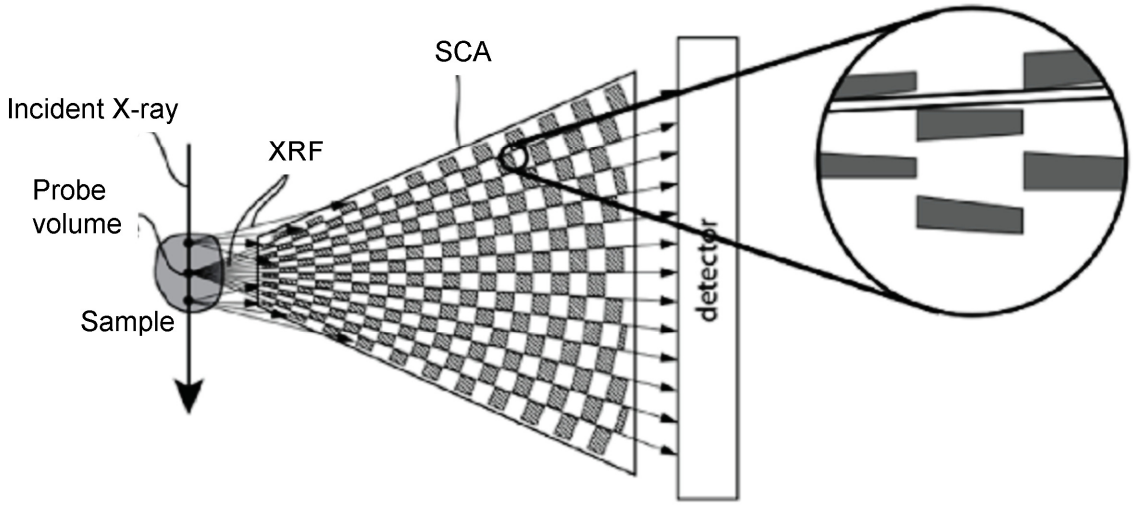

Figure 2.3 The schematic diagram of an improved SCA design. The collimating channels are formed by a series of staggered absorbing pillars. The inset shows that the pillar edges are tapered away from the axis of each channel. This figure is reproduced from reference 5.

2.2.3 Polycapillary vs. spoked channel array

Either a polycapillary or an SCA optic is used to construct the probe volume in a CXFI experiment. While each has its own advantages and disadvantages, it is upon the user to decide which optic better suits a specific experiment. A comparative discussion between the optics is provided below.

Mechanism of function: X-ray photons in a polycapillary optic propagate through numerous hollow glass channels by the process of total external reflection at the glass surface. Total external reflection occurs when the incident beam strikes the glass at an angle equal to or smaller than the critical angle. A detailed description of the mechanism can be found elsewhere.[3] In contrast, X-rays in a SCA optic transmits through the collimating channels lithographically created in silicon or germanium. In the limit of zero reflection from the channel walls, the degree of collimation and optic's resolution is solely determined by the length and width of channels. A detailed mechanism is available elsewhere.[1] A consequence of the different mechanisms of function is that in the case of the polycapillary the transmission depends on X-ray energies (equation 2.1), but no such dependency exists in case of the SCA optic.

Resolution: The size of polycapillary focal spot, which is inversely proportional to energy and proportional to focal distance, determines the resolution (equation 2.2).[1] A state-of-the-art XOS® polycapillary offers the highest resolution of ~8 μm with ~2 mm focal distance at Mo K_α (~17.5 keV). According to equation 2.2, further improvements in resolution would result in shorter focal or working distances. Additionally, since the polycapillary resolution is inversely proportional to energy, resolution is worst in the low energy (2 - 5 keV) regime. The best polycapillary resolution reported in that regime is upwards of 20 μm.[2] On the other hand, the focal spot or resolution of a SCA optic is solely determined by its length and width,[2] thus avoiding energy dependency. The highest resolution demonstrated by a SCA optic is ~1.7 μm at 4 -10 keV.[2] This is particularly valuable for the study of biologically relevant light elements such as P, S, Cl, K and Ca in intact samples, which are expected to show spatial variation in 1 μm scale. The higher resolution of a SCA optic is not only valuable in resolving ~ 1 μm scale features in elemental mapping, but also in collecting highly localized microstructure specific chemical speciation information from a CXAS experiment.

Working distance: The working distance is the distance between the tip and focal spot of the optic. A reasonable working distance is important for sample translation or installation of a sample cooling stage. Regardless of the type of focusing optics, improved working distance comes at the expense of poorer resolution, or vice versa. Polycapillaries with poorer resolving capacity, tend to have better working distances (e.g. 9 mm for a 25 µm focal spot size) compared with about 0.2 mm for the initially tested 5 µm SCAs or about 1.5 mm in the improved design 5 µm SCAs. An SCA optic has some advantages over a polycapillary with the same working distance due to the SCA's compact design and lack of metal coating. The new SCA design, in which collimating channels are formed by the staggered arrays of pillars,[5] has improved the working distance to a manageable value of about 1.5 mm. Although this improvement will significantly extend its application, the scope of installing a sample cooling stage or measuring a sample with uneven surface will still remain challenging.

Collection efficiency: A comparison between the intensities (amount of fluorescence) collected by a SCA optic and polycapillary from the same confocal volume at a constant energy would favor the latter. The higher efficiency for a polycapillary can be primarily attributed to its higher acceptance from the vertical solid angle. Although the collection efficiency of a SCA optic with regard to its collection from the horizontal solid angle would be similar to a polycapillary, the collection from the vertical solid angle would be somewhat less. The key factor limiting the vertical collection is the SCA optic depth, which vary from 30-50 µm for channel widths of 1-5 µm.[2] These depths are limited by the typical aspect ratios for DRIE.[2,5] In order to achieve deeper channels with routinely-achievable trench aspect ratios, a new mask design was implemented in which channels were effectively formed by a series of staggered pillars (Figure 2.3).[5] This staggering increased the trench width without increasing the channel-width, thus resulting in a factor of 10 greater collection efficiency nearly equivalent to a polycapillary.[5] Further improvement in the total count rate for a polycapillary or SCA may be achievable by implementing a detection focusing unit comprising a number of optics (polycapillary or SCA) installed on a mount all focused at the same probe volume in conjunction with a multielement discrete array or Maia-type detector. Such improvement would lead to an extension of the scope of CXFI application.

Fragility: A SCA optic is much more fragile compared to a polycapillary, hence needs extra caution during handling, mounting and experiment. The metal coating on polycapillaries makes them durable. In contrast, SCAs are still undergoing development and current stage has no protective coating.

Ease of mounting and alignment: Due to fragility and very short working distance, the mounting and alignment of a SCA optic need extra caution. In contrast, mounting and alignment is much easier with a polycapillary as they are durable and offer longer working distance.

2.3 Polycapillary Based CXFI / CXAS Studies

Systems studied in this thesis using the polycapillary optic based CXFI included (*a*) zebrafish larvae exposed to organic and inorganic mercury, (*b*) mouse brain sections, (*c*) zebrafish larvae exposed to elevated selenium, and (*d*) archaeological human bones. The exposure of zebrafish to the mercury and selenium compounds and related sample preparations were approved by the University of Saskatchewan's Animal Research Ethics Board and adhered to the Canadian Council on Animal Care guidelines on the care and use of fish in research, teaching, and testing. Ethics approval with regard to studying archaeological bone samples was also obtained from the University of Saskatchewan Biomedical Research Ethics Board prior to the study. Among the list, samples in *a* and *b* were measured at various stages of the development of CXFI setup, and samples in *c* and *d* were measured with a stable CXFI setup. The experiments at the developmental stages have played important role in the improvement of setup, thus in achieving the goal of this thesis. However, as one can imagine, the results from the test experiments were often imperfect due to the limitations present in the setup. On the other hand, the experiments which exploited the stable CXFI setup shed light on better understanding of the important scientific issues. The following sections present the description of experiments.

2.3.1 Measurements at 20ID-B, APS

The CXFI development project reported in this thesis was conducted through a close collaboration with the beamline 20ID-B at APS. This beamline offers several important capabilities suitable for a CXFI application, such as high flux approaching 1×10^{11} photons/s/μm^2,

micro-beam down to 1-2 µm, and access to absorption spectroscopy. A detail of the setup and capabilities of the beamline can be found elsewhere.[6,7] The choice of 20ID-B as our experimental venue was also influenced by the partnership relation between CLS and 20ID-B, APS through the *CLS@APS programme*. The majority of experiments presented in this thesis have exploited the Canadian share of beamtime made available via the Partner User Agreement between CLS and APS. This project contributed to the upgrade of beamline 20ID-B to include the confocal capability in XFI and XAS. The following sections summarize all polycapillary based CXFI / CXAS measurements performed at 20ID-B at various stages of the technique development.

2.3.1.1 Zebrafish larva exposed to organic Hg

This study represents the first test CXFI experiment at 20ID-B, APS. A zebrafish larva exposed to organic mercury (Hg) was chosen as the test sample. This system was previously studied using a conventional XFI experiment to understand the mechanism of the toxicity of organic Hg.[8] The substantial knowledge made available from that previous study influenced the selection of this particular sample as a test specimen. The objective of this test measurement was to repeat the elemental imaging of fish eye using the first installed CXFI setup at 20ID-B and then to compare the results with that of previously published in the conventional XFI study.[8]

The first CXFI setup at 20ID-B, APS: Beamline 20ID-B employs an X-ray microprobe based on a K-B mirror pair. One of the great advantages of K-B mirror is its achromaticity, which allows large energy changes without realignment. This enables employing high excitation energy to excite nearly all elements in an imaging experiment, and then continuing with XAS experiments in which lower excitation energies are exploited. There are two sets of K-B mirror pairs at 20ID-B, a 200 mm long pair typically used for achieving 4 - 6 µm beam spot and a pair of 100 mm long mirrors capable of focusing down to 1 - 2 µm beam spot size.[7] For the detection side focusing optic, a polycapillary purchased from XOS® of focal spot = 25 µm (at Mo K_α), working distance = 10 mm, and collection angle = 20° was employed. The polycapillary was mounted on the snout of a single element Vortex® silicon drift X-ray fluorescence detector. Both the detector and sample were mounted on high precision XYZ motorized stages. An ion chamber I_0, placed between the K-B mirror pair and sample, was used to measure the intensity of incident

X-ray beam. Sample and detector were mounted at 45° and 90º, respectively to the incident X-ray beam. This geometry minimizes the scattering of linearly polarized synchrotron radiation as the scattering cross-section along the e-vector is zero.[9] For the measurement of elemental maps, the sample was spatially rastered in the micro-beam by means of the translation of a high precision XYZ stage. Figure 2.4 shows a photograph of the first CXFI experimental setup at 20ID-B beamline.

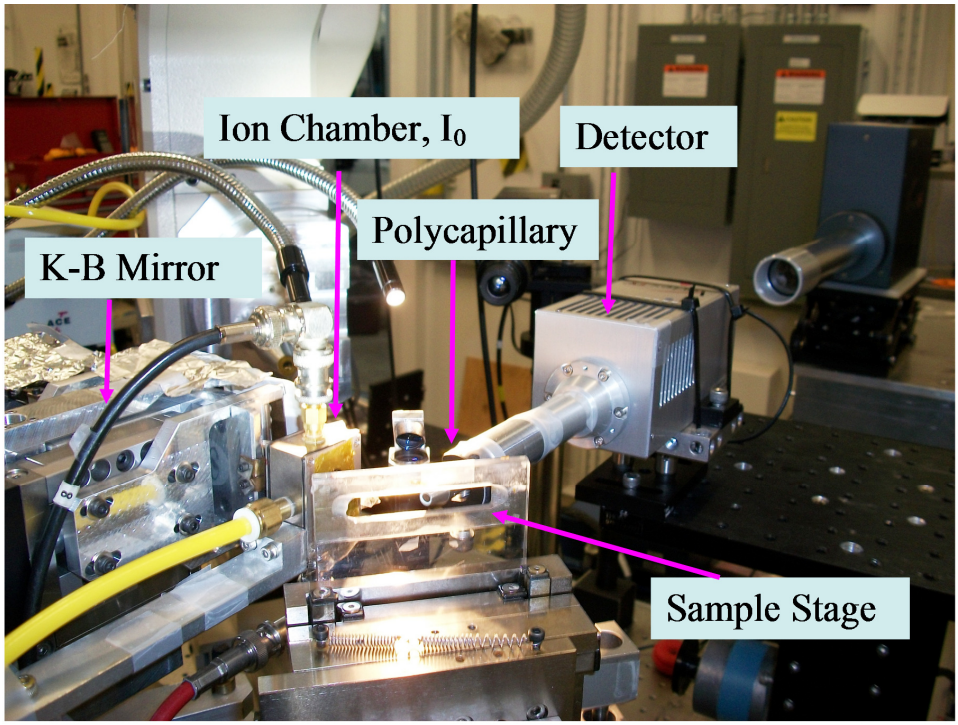

Figure 2.4 A photograph showing the first CXFI setup at beamline 20ID-B, APS.

Methods: Three days old zebrafish larvae were exposed to 0.5 µM methylmercury L-cysteineate solution for 18 hrs. Fish larvae were fixed in 4% paraformaldehyde and finally embedded in 1% agarose gel. The gel block sections containing fish heads were carried to beamline 20ID-B, APS for the experiment. An intact eye was targeted for the CXFI measurements. The experiment was performed using the CXFI setup described above with a beam size of ~ 4 µm (horizontal) × 6 µm (vertical). The alignment of incident and detection focusing optics, K-B mirror and polycapillary, to form the probe volume took approximately 8 hrs of beamtime. A rough estimate of the coordinates confining the volume containing a fish eye was determined by performing several one and two dimensional coarse scans. For depth

profiling, a series of two dimensional maps were collected at every 25 µm depth by translating the sample toward the polycapillary, equivalent to moving the probe volume deeper into the sample. A series of ten sequential two dimensional maps covering the whole eye were collected. Each had an area of 600 µm × 400 µm and took approximately 1.5 hrs of beamtime with 0.4 sec per point integration time. Thus a total of ten maps took approximately 15 hrs of beamtime.

Data were analysed using the SMAK (http://home.comcast.net/~sam_webb/smak.html) and Voxler® (http://www.goldensoftware.com/products/voxler) software packages. The recorded fluorescence counts were normalized to the incident X-ray intensity and were background corrected by subtracting the average intensity of pixels outside the image from the intensity of each pixel of the image.

Results and Discussion: Figure 2.5 shows ten consecutive two dimensional maps collected at every 25 µm depth through the eye. The elemental distribution of Hg, Fe, and Zn are shown in red, blue, and green, respectively. The eye lens started appearing in the third map and continued till the eighth map. The circular shaped bright red blob represents the occurrence of the accumulation of Hg in the eye lens. The bowl-shaped green structure represents the Zn distribution in the retina. A movie showing three dimensional distributions of elements was generated by the stacking of all ten maps. Figure 2.6 shows a snapshot taken from that movie. A comparison of the results with that shown in the previous conventional XFI study[8] shows good agreement. Both studies show a striking preferential accumulation of organic Hg occurring in the outer layer of eye lens and the presence of Zn in the retina.[8] The ability of the employed CXFI setup to reproduce these results was indicative of a successful initiation of CXFI project at 20ID-B.

While the performance of this first CXFI configuration was promising, some irradiation effects such as browning and slight melting on sample at the end of the experiment were observed. In contrast to conventional XFI measurements, the CXFI measurements lead to higher irradiation of the sample as the same path is irradiated multiple times during the course of measuring successive optical sections. The prolonged irradiation results in drying, browning and melting of the sample and embedding material. Therefore, a cooling system was proposed to be

installed in order to improve the performance of the setup in Figure 2.4 when measuring delicate biological samples, a modification which was implemented as described in 2.3.1.2 below.

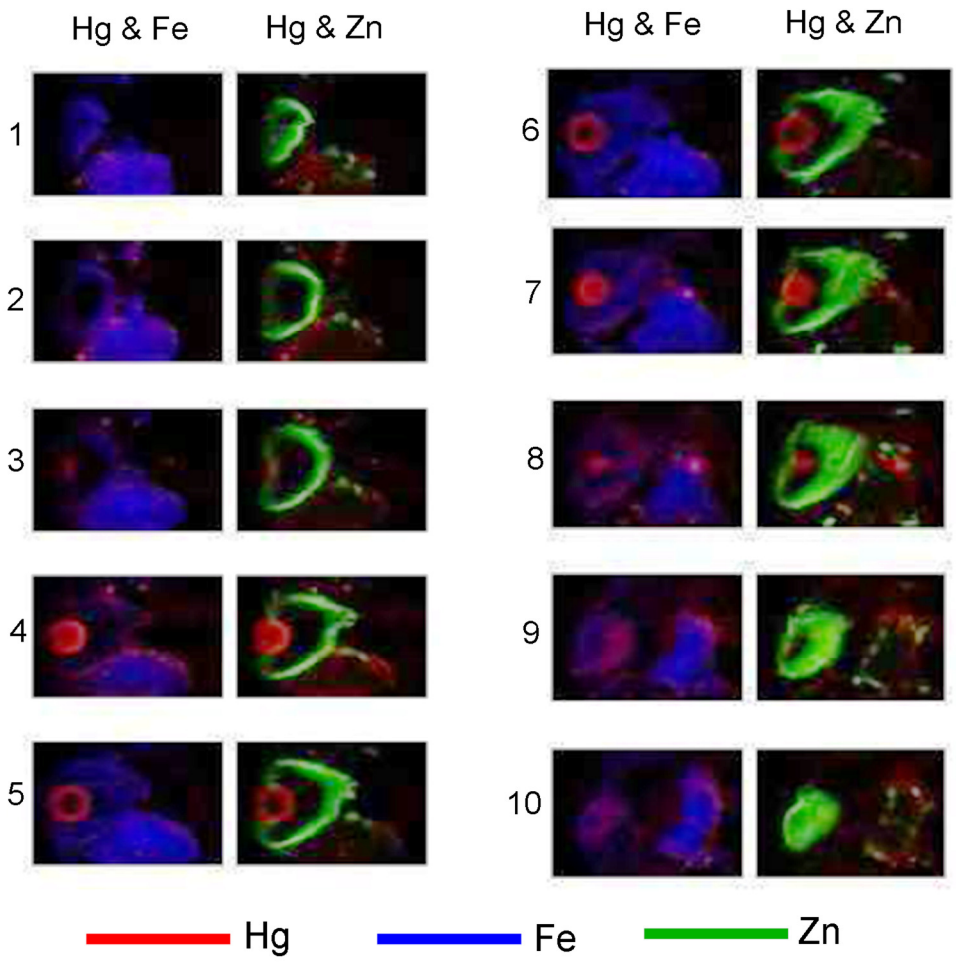

Figure 2.5 Consecutive two dimensional CXFI elemental maps along the depth of an intact zebrafish eye. The numbers on left represent the sequence of optical sections with a depth increment of 25 µm for each. Each map shows an approximate area of 600 µm × 400 µm.

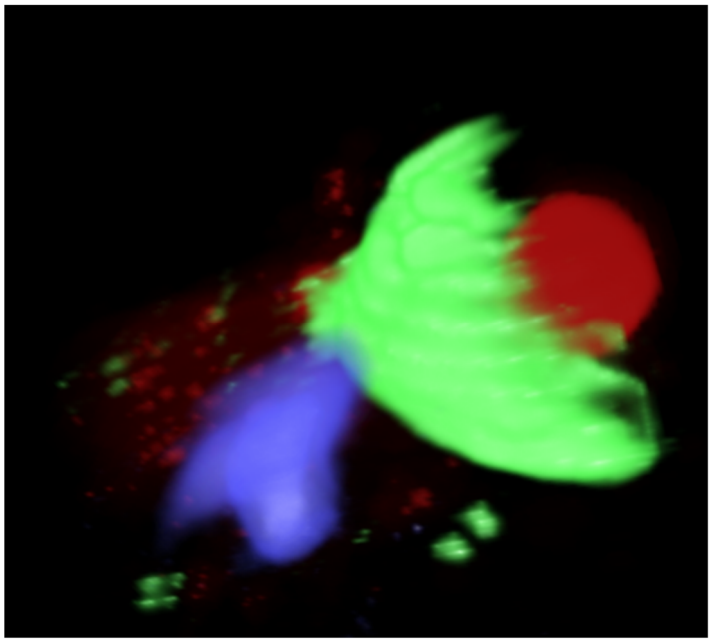

Figure 2.6 A snapshot from the movie constructed by stacking and combining the maps of Figure 2.5. Figure displays the distribution of elements in three dimensions.

2.3.1.2 Zebrafish larva exposed to organic and inorganic Hg

In this stage, the experimental setup described in the previous section (Figure 2.4) was improved by installing a liquid nitrogen based cooling system (Figure 2.7), which was intended to minimize the effect of irradiation on the sample. The objective of this experiment was to test the performance of the newly installed cooling system. A previously studied system was chosen as the subject of the experiment in order to take advantage of the known outcomes. Two zebrafish larvae, one exposed to organic Hg and the other exposed to inorganic Hg were studied to compare the uptake of organic and inorganic forms of Hg in zebrafish larvae. This was previously studied using a conventional XFI experiment.[10]

Method: The CXFI setup at 20ID-B presented in section 2.3.1.1 was employed, with the addition of a newly installed cooling system. The cooling system, as shown in Figure 2.7, comprised of a liquid nitrogen dewar, a LNP4 liquid nitrogen pump, and a Linkam THMS600 stage. The sample was mounted inside the Linkam THMS600 stage, which received a constant liquid nitrogen flow to maintain sample temperature approximately at -80ºC throughout the

experiment. For sample preparation, zebrafish larvae of 3.5 days post fertilization exposed to 1μM mercury chloride ($HgCl_2$) or 1μM methyl mercury chloride (CH_3HgCl) solutions were fixed in 4% paraformaldehyde and embedded in polymer. The established protocol employed for zebrafish fixation and embedding can be found elsewhere.[10] In the experiment, $HgCl_2$ and CH_3HgCl samples were measured to collect respectively 11 and 14 sequential two dimensional maps of area 870 μm × 600 μm and 680 μm × 600 μm at every 25 μm of depth. Approximately, 30 hrs of beamtime was required to accomplish collecting maps for both samples.

Results and Discussion: Figure 2.8 shows snapshots from the movies created by the stacking of depth specific two dimensional elemental maps measured from zebrafish larvae samples exposed to organic CH_3HgCl and inorganic $HgCl_2$ mercury compounds. While the CH_3HgCl-map was extended till the yolk-region, the $HgCl_2$-map was focused only at the eye-region due to the bigger sample size and limited synchrotron beamtime. A comparison between the maps shows a striking fact that the accumulation pattern of Hg in zebrafish varies with its chemical species. No Hg accumulation is observed in the eyes of $HgCl_2$ map, but CH_3HgCl-map shows Hg in lens epithelial region for both eyes. The brain region between two eyes show more Hg and less Zn in case of $HgCl_2$ compared to CH_3HgCl. Regardless of the type of exposure, Se and Zn are predominantly present respectively in the eye lens and retina. These results show close similarity with that of reported previously.[10]

It was observed that the installation of the cooling system greatly helped reducing the irradiation effect, however still a further improvement was felt necessary as the experiment was affected by an abrupt stop necessitated by a sudden temperature rise and consequent melting of sample. The consequence of the abrupt stop is visible in the $HgCl_2$-map, in which although a complete view is available for one eye, the other eye is only partially visible. A follow-up investigation revealed that this abrupt increase in temperature was due to the occurrence of an ice-clogging in the transfer line. This ice-clogging interrupted the liquid nitrogen flow, thus increasing the temperature of the sample. In order to prevent such ice-clogging, the implementation of a better quality and larger diameter transfer line was proposed. The measurement of CH_3HgCl-map was also interrupted by a sample shift, which was thought to be due to the vibrations from the refill of liquid nitrogen dewar every few hours. This refill was

necessitated by the small size (2L) of the dewar as the size was insufficient for many hours long CXFI experiment. Therefore, in addition to a better quality and larger diameter transfer line, the purchase and installation of a bigger dewar was also proposed for future experiments.

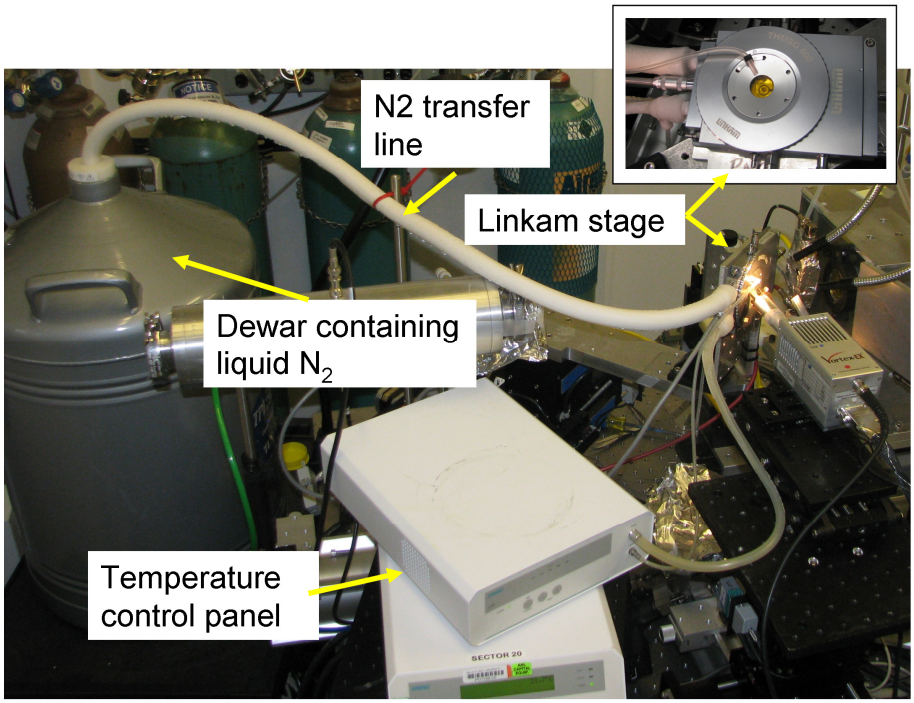

Figure 2.7 A photograph of CXFI setup at 20ID-B, APS with the newly installed sample cooling system. Inset shows a zoomed in view of the Linkam THMS600 sample stage.

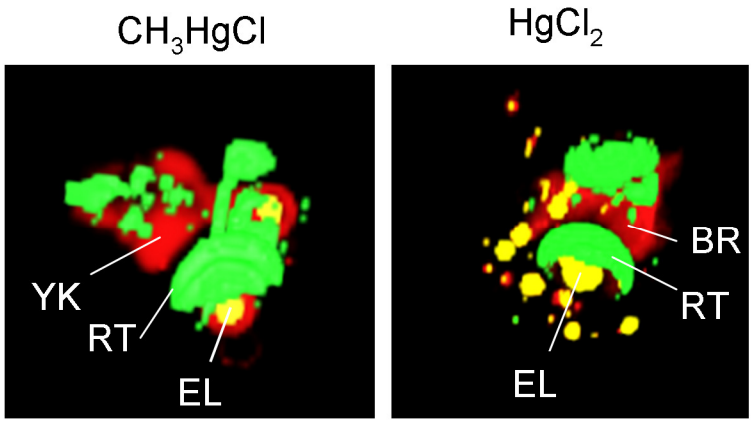

Figure 2.8 Elemental distributions in the snapshots taken from the movies generated through stacking of two dimensional maps measured from zebrafish larvae exposed to CH_3HgCl and $HgCl_2$. Map area: 870 µm × 600 µm for CH_3HgCl and 680 µm × 600 µm for $HgCl_2$. Colour legend: Zn in green, Se in yellow and Hg in red. RT: Retina, EL: Eye lens, BR: Brain and YK: Yolk.

2.3.1.3 Mouse brain

This experiment attempted a feasibility test of measuring a mouse brain sample at 20ID-B, APS using CXFI. This experiment shared the same run of beamtime exploited in the above section 2.3.1.2; hence no reliable cooling system was available due to the problem as a result of ice-clogging. Metal distributions in the hippocampus are critical for the understanding of Alzheimer's or other neurodegenerative diseases,[11] hence the hippocampus area of a mouse brain was targeted in the experiment. A concern in the area of brain tissue research is that, the metal distributions may be altered as a consequence of tissue sectioning.[12] A confocal mode of measurement can be very useful in addressing this concern, as the confocal approach allows avoiding thin sample sectioning by enabling measurement of the intact samples.

Method: The CXFI setup shown in Figure 2.4 without a cooling system was employed. The hippocampus-region section from a freeze dried wild type mouse brain was sandwiched between a metal free plastic coverslip (PET film) and thermanox, which then was measured for metal distributions. The hippocampus area and a lateral ventricle on the right side of the brain

were imaged. Ten depth specific two dimensional elemental maps of area 3 mm × 2 mm were collected at every 25 µm depth. Each map took approximately 3.5 hrs of beamtime, thus a total of approximately 35 hrs of beamtime was required in the experiment.

Results and Discussion: Figure 2.9 shows a snapshot from the movie generated by the stacking of ten depth specific two dimensional maps. A distinct pattern of iron distribution in the map nicely shows the hippocampus structure.[11] Cu is observed in the periventricular regions of the lateral ventricle. These observations are consistent with the findings of Pushie *et al.*[13] and Antharam *et al.*[11] A crack visible in the map can be attributed to the sample drying due to long irradiation. The post measurement examination of sample using microscope showed tearing of sample. It may be worth noting that, a lesser extent of irradiation effect was observed in the freeze dried samples used herein compared to the formalin fixed samples presented in section 2.3.2.1. The observed irradiation effect further emphasizes on the requirement of a cooling system for biological CXFI.

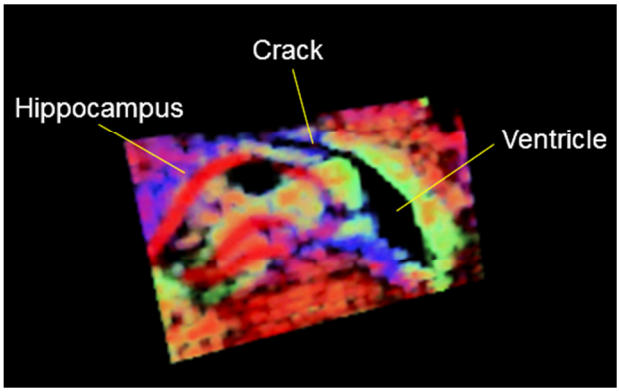

Figure 2.9 Elemental distributions in the vicinity of hippocampus and right lateral ventricle in a mouse brain. Map area = 3 mm × 2 mm. Color legend: Fe in red, Cu in green and Zn in blue.

2.3.1.4 Zebrafish larvae exposed to elevated selenium

This study exploited the first stable CXFI setup installed at 20ID-B, APS. The implementation of a better quality transfer line and bigger dewar allowed achieving a reliable cooling system for the setup. The improved cooling system was successfully used to keep the sample cool at -80 °C by maintaining a constant flow of liquid N_2 throughout the course of this experiment. The experimental setup shown in Figure 2.7 with an improved cooling system, and a beam spotsize and polycapillary depth resolution of ~5 μm × 5 μm and ~40 μm (at Se K_α), respectively was employed.

The study investigated the effect of embryonic exposure to elevated selenium by employing CXFI and CXAS to determine the distribution and localized speciation of Se in intact zebrafish larva sample. The ability to employ an intact sample avoided sample sectioning, enabled investigation of a generic volume element anywhere in the sample and ensured sample integrity. Additionally, the use of confocal geometry led to an increased signal-to-background ratio, as the polycapillary rejected emission or scatter originating from outside of the confocal volume. A successful completion of about 3 days long CXFI measurements with no obvious irradiation effect on sample proved the effectiveness and reliability of the developed cooling system. The CXAS experiment performed herein marked the first implementation of biological CXAS.

Details of this investigation are presented in chapter 3 of this thesis. This study is published in *Environmental Science & Technology* 49: 2255-2261 (2015).

2.3.1.5 Archaeological human bone

This study also exploited a stable CXFI setup at 20ID-B, APS. A cooling system was not used, since the thickness of the sample was too high to fit inside the cooling stage, and bone is expected to be more resistant to radiation compared with the zebrafish larvae or rat brain samples. The experimental setup presented in Figure 2.4 with a micro-beam of ~ 5 μm × 5 μm spot-size and a polycapillary depth resolution of ~40 μm (at Pb L_α) were employed.

Study of the trace element content in archeological samples provides important insight about the health and lifestyles in the past, however the scope of such studies are often limited by the fragile nature of the poorly preserved archaeological samples. Synchrotron based XFI provides greatest element specificity in elemental imaging but the standard technique requires a sample thickness equal to the desired spatial resolution. A fragile archeological sample is therefore a challenge for standard XFI. In this study, a poorly preserved archaeological human bone sample recovered from the Royal Naval hospital Cemetery (c. A. D. 1793 – 1822) near English Harbour, Antigua was measured for elemental mapping using CXFI. The study demonstrated the value of CXFI as a tool for generating high resolution elemental images from a selected section within a thick fragile archaeological bone sample showing excellent details of elemental incorporation into bone microstructures.

Details of this investigation are presented in chapter 4 of this thesis. This study is accepted for publication in *Archaeometry* (**2016**, In press, DOI: 10.1111/arcm.12232).

2.3.2 Measurements at G-Line, CHESS

The G-line at CHESS offers a bigger beam spot size of ~ 25 μm, which is relevant for a bigger biological sample such as a brain. Hence, this experiment was intended to take advantage of a bigger beam at G-Line, CHESS. The additional purpose of this experiment was to gain CXFI expertise from CHESS, since a depth profiling study of a multilayered paint sample was previously reported based on CXFI data produced at CHESS.[14] The following study represents the first biological CXFI measurement at G-line, CHESS.

2.3.2.1 Transgenic mouse brains

Prion protein (PrP^c) has received considerable research attention due to its role in the fatal neurodegenerative disease called prion disease.[13] A previous conventional XFI study showed considerable variation in the localization and concentration of metals in the vicinity of lateral ventricles among the wild-type, prion gene knockout and prion gene over-expressing brain samples.[13] In this study, transgenic mouse brain sections collected from wild-type, prion gene knockout and prion gene over-expressing mice were chosen as test samples. The objective

of the experiment was to test the feasibility of the employed CXFI setup in measuring the elemental distributions of these three types of mouse brains, while taking advantage of the bigger beam size (~25 µm) available at G-Line, CHESS and known outcome of the experiment.

The CXFI setup at G-Line, CHESS: A single bounce monocapillary developed at CHESS,[15] was used to focus the incident beam onto the sample. Monocapillaries are compact and demonstrated to function well at up to 40 keV.[14] Also, monocapillaries offer a working distance of up to several cm and reflection efficiencies of upwards of 90%. Fluorescence was collected by employing a XOS® polycapillary of focal spot ~25 µm, as used at 20ID-B, APS, mounted on a Rontec (Carlisle, MA) Xflash silicon drift detector. The components such as, monocapillary, sample, and detector were mounted on high precision motorized translation stages for the purposes of alignment and scanning. The sample was positioned at 45º to the incident beam and detector. The CXFI measurements at CHESS used ~16 keV of excitation energy. The unattenuated flux on the sample was estimated to be ~2 × 10^{11} photons/s. Figure 2.10 shows a photograph of the CXFI setup at G-line, CHESS.

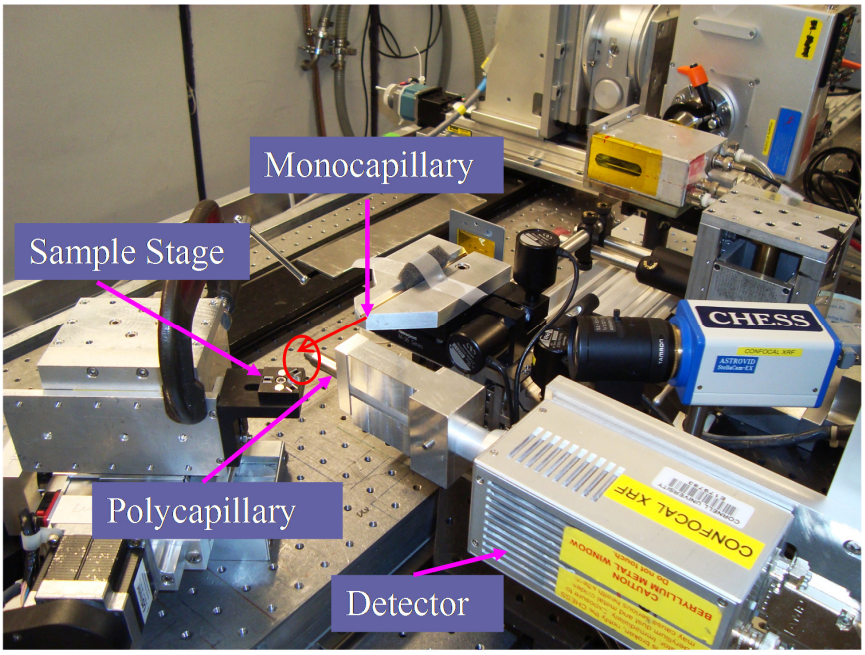

Figure 2.10 A photograph of the CXFI setup at G-line, CHESS.

Method: The formalin fixed transgenic mouse brains were sectioned in 1 mm thick slices using a tissue matrix, and then a single slice from similar brain region per type was sandwiched

between a metal free plastic coverslip (PET film) and thermanox. To prevent the quick drying of brain sections, a small formalin-dipped Kim wipe piece was placed in the corners of sandwiches. In the experiment, these sandwiched brain sections were mounted on the sample stage with the PET film side facing the beam as the PET films are ultrathin and minimize the attenuation of fluorescence. Experiments employed the above CXFI setup with a beam size of approximately 20 μm × 20 μm. The alignment of monocapillary, sample, and polycapillary took approximately 5 to 6 hrs of beamtime. Several coarse scans were performed to identify the coordinates of the volume confining the lateral ventricle in a brain section sample. Depth specific two dimensional elemental maps at every 30 μm of depth were collected by translating the sample on a motorized XYZ stage. Approximately 19 hrs of beamtime per sample was required to accomplish collecting a series of 15 depth specific two dimensional maps of area ~ 2 mm × 2 mm.

Data were analysed using the SMAK (http://home.comcast.net/~sam_webb/smak.html) and Voxler® (http://www.goldensoftware.com/products/voxler) software packages. The recorded fluorescence counts were normalized to the incident X-ray intensity and were background corrected by subtracting the average intensity of pixels outside the image from the intensity of each pixel of the image.

Results and Discussion: Figure 2.11 presents snapshots taken from the movies showing three dimensional distributions of elements in the vicinity of lateral ventricles in the brain section samples of prion gene knockout (a), prion gene over-expressing (b), and wild type (c) mouse brain samples. For comparison, all maps were created with the same color contrast and settings. The comparison shows clear variations in the distributions of Cu and Ca among the samples. Overall, the prion gene knock-out and over-expressing samples respectively show higher and lower concentrations of Cu and Ca around the ventricle compared to the wild type. A considerable colocalization of Cu and Ca is observed in the knock-out and wild type samples. A thin structure appearing as a connecting tissue in the ventricle of over-expressing sample is the choroid plexus,[16] which produces cerebrospinal fluid in the brain and also acts as a filtration system for the removal of metabolic waste and foreign substances from the cerebrospinal fluid.[17] There is evidence that a choroid plexus plays crucial role in metal sequestration and transport into the brain.[17] However, it is difficult to image using a conventional XFI experiment

as it is a delicate structure and often lost during sample sectioning.[12] The appearance of choroid plexus in the present study certainly demonstrates a strength of CXFI. A CXFI experiment is inherently designed to enable the measurement of intact samples, thus is able to play a significant role in imaging delicate biological structures such as a choroid plexus. A comparison of the results with those in the conventional XFI study published previously show good agreement.[13] Both studies show that the over-expressing prion gene sample is greatly different than the wild type with regard to the distributions of Cu and Ca.

Although caution was taken to reduce the sample drying by implementing wet Kim wipes inside the sample sandwiches, some tears were still visible (Figure 2.11 (b)). Measuring the samples with a cryoprotection in place should prevent the brain tissue from tearing.

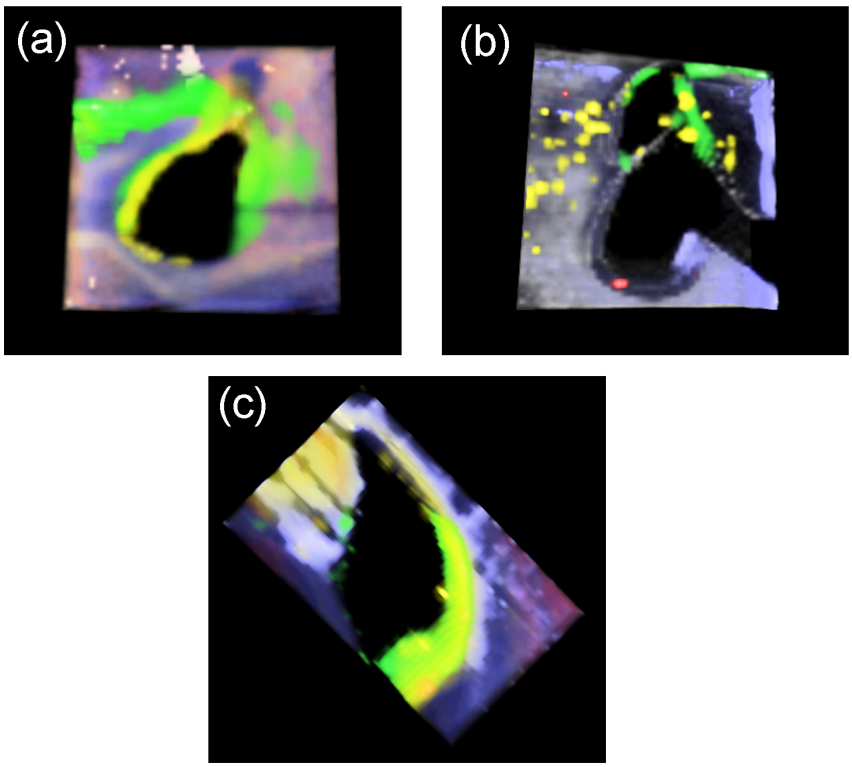

Figure 2.11 CXFI derived elemental distributions in the vicinity of left lateral ventricles in mouse brain samples. (a) A prion gene knockout (2 mm × 2 mm), (b) A prion gene over-expressing (2 mm × 2 mm) and (c) A wild type (1.5 mm × 2.5 mm). Color legend: Cu in green, Zn in blue, Ca in yellow, and Fe in red.

2.4 SCA Based CXFI / CXAS Studies at 20ID-B, APS

The SCA optic (section 2.2.2), developed at CHESS, is a novel alternative of polycapillary detection optic. The implementation of SCA optic was intended to achieve better spatial resolution than a polycapillary in CXFI. Since a brighter synchrotron source supported the better performance of SCA optic, the beamline 20ID-B was the primary venue for implementing this device. Samples studied in this thesis using SCA optics included (a) ancient stained glass and (b) archaeological human bones. The inorganic type ancient stained glass samples were chosen for the first trial due to the higher metal concentrations and less delicate nature compared to the biological counterparts. After a successful initiation of the implementation of the optic, a number of biological samples of contrasting nature were measured by employing SCA optics of varied depth resolutions.

2.4.1 Antique stained glass

This study exploited the first stable SCA based CXFI setup installed at 20ID-B, APS. The implementation of a Linkam cooling stage was neither practical due to the very small working distance available in a SCA based setup nor necessary due to the inorganic nature of sample used in this experiment. A 200 mm long K-B mirror pair for achieving a beam spot size of approximately 5 µm × 5 µm was employed. A SCA optic of 7 µm depth resolution, fabricated from the silicon substrate, comprising 96 channels with a 4 mm channel length and an etch depth of about 200 microns was employed. A working distance of only few hundred microns was available for the sample translation necessitated by alignment and scanning.

Stained glass windows were one of the major pictorial art forms in medieval European culture and many examples still exist in their original form. In order to optimize cleaning, restoration and conservation procedures of these valuables, it is important to explore in-depth non-invasive elemental investigations. This study employed SCA based CXFI and CXAS in stained glass samples from 13^{th} century Paderborn Cathedral, Germany to demonstrate the efficacy of SCA derived superior spatial resolution in depth-profiling of the distribution and speciation of elements. The study represented the first demonstration of SCA based CXAS.

A detail of this investigation is available in chapter 5. This study was published in *Journal of Analytical Atomic Spectrometry* 30: 759-766 (2015).

2.4.2 Archaeological human bone

This study also exploited stable SCA based CXFI setups installed at 20ID-B, APS. The implementation of a Linkam cooling stage was neither practical due to the very small working distance available in a SCA based setup nor necessary as this sample showed no obvious irradiation effect when measured previously using a polycapillary based CXFI setup (section 2.3.1.5). Two CXFI configurations constructed based on two versions of SCA optics comprising 2 µm and 5 µm resolutions both etched from germanium substrates were employed. The 2 µm optic was comprised of 101 channels with channel length of 4 mm. The etch-depth and working distance for this optic was about 200 microns and 1 mm. The 5 µm optic had 75 channels of channel length 1.5 mm, and an etch depth and working distance of about 300 microns and 1.5 mm, respectively. Two sets of K-B mirror pairs; a 200 mm long pair for achieving approximately 5 µm × 5 µm beam spot to use with the 5 µm SCA optic, and a pair of 100 mm long mirrors for producing approximately 2 µm × 2 µm beam spot size to use with the 5 µm SCA optic, were employed.

The poorly preserved archaeological bone samples recovered from the Royal Naval Hospital cemetery (c. A.D. 1793-1822) near English Harbour, Antigua were previously studied using polycapillary based CXFI and presented in section 2.3.1.5. These samples are further studied here to take advantage of SCA derived superior resolution CXFI. By employing CXFI and CXAS, respectively, the three dimensional elemental distributions and the highly localized chemical forms of Pb were measured. This study demonstrated the first application of germanium based SCAs, which enabled studying higher energy fluorescence such as Sr Kα. This study enabled collecting subcellular resolution maps and bone microstructure specific speciation information with an improved signal to noise. The CXAS experiment performed here marked the first SCA based biological CXAS.

A detail of this investigation is available in chapter 6.

2.5 Acknowledgements

The author is greatly indebted to her supervisors Drs. I. J. Pickering, G. N. George and I. Coulthard for their guidance, scientific input and funding for the research. The SCA optics employed in this research are designed and fabricated by a Cornell group; the author is grateful to Dr. A. R. Woll and his student D. A. Budu for making the SCA optics available for this research, providing help during experiments and valuable discussion. The author is also grateful to Dr. E. Hallin for making available his technique development beamtimes at 20ID-B, APS, providing training on PyMCA data analysis toolkit and valuable discussion. The samples reported in this research were obtained from varied sources: author is thankful to Drs. M. Korbas and T. MacDonald for providing zebrafish samples reported in sections 2.3.1.1 and 2.3.1.2, Drs. M. J. Hackett and M. J. Pushie for providing brain samples reported in sections 2.3.1.3 and 2.3.2.1, Dr. J. Hormes for providing antique stained glass sample reported in section 2.4.1, Drs. T. Swanston and T. Varney for proving bone samples reported in sections 2.3.1.5 and 2.4.2. The author is grateful to Dr. P. Krone's Lab and Dr. D. Janz's Lab for zebrafish sample preparation. Thanks to Dr. J. K. Thomas and N. J. Sylvain for proving training in preparing zebrafish samples reported in section 2.3.1.4. Thanks to Dr. O. Ponomarenko for helping with the data collection and providing a script for easier CXAS data analysis for the project mentioned in section 2.3.1.4. The author would like to thank Dr. M. J. Hackett for helping with data collection for the experiments mentioned in sections 2.3.1.2, 2.3.1.3 and 2.3.2.1. The author is very thankful to beamline scientists Drs. R. Gordon and Z. Finfrock at 20ID-B, APS and Dr. A. R. Woll at G-line, CHESS.

Most of the data were collected at 20ID-B, APS. Sector 20 facilities at the Advanced Photon Source, and research at these facilities, are supported by the US Department of Energy - Basic Energy Sciences, the Canadian Light Source and its funding partners, the University of Washington, and the Advanced Photon Source. Use of the Advanced Photon Source, an Office of Science User Facility operated for the U.S. Department of Energy (DOE) Office of Science by Argonne National Laboratory, was supported by the U.S. DOE under Contract No. DE-AC02-06CH11357. Data reported in section 2.3.2 were collected at the G-line, CHESS. CHESS is

supported by the NSF & NIH/NIGMS via NSF award DMR-1332208, and the MacCHESS resource is supported by NIGMS award GM-103485.

This research was supported by NSERC Discovery Grants (to GNG and IJP), a Social Sciences and Humanities Research Council (SSHRC) Insight Development Grant (#430-2012-0236), and Canada Foundation for Innovation through funding for BioXAS: Life Science Beamline for X-ray Absorption Spectroscopy at the Canadian Light Source Inc. The author is a fellow in the Canadian Institutes of Health Research Training grant in Health Research Using Synchrotron Techniques (CIHR-THRUST).

2.6 References

(1) Paul, S. J.; David, G. M.; Walter, G. M.; Ning, G.; Huapeng, H.; Igor, P. Y. Overview of polycappilary X-ray optics. *Powder Diffr.* **2002**, *17*, 70–80.

(2) Woll, A. R.; Agyeman-Budu, D.; Bilderback, D. H.; Dale, D. 3D X-ray fluorescence microscopy with 1.7 µm resolution using lithographically fabricated micro-channel arrays. *SPIE Optics and Photonics* **2012**, *8502*, 85020K–1 – 85020K–14.

(3) MacDonald, C. A. Focusing polycapillary optics and their applications. *X-Ray Opt. Instrum.* **2010**, *2010*, 1–17.

(4) *X-ray Spectrometry: Recent Technological Advances*; Kouichi, T.; Injuk, J.; Grieken, R. Van, Eds.; John Wiley & Sons, Ltd: West Sussex, England, 2004.

(5) Woll, A. R.; Agyeman-Budu, D.; Choudhury, S.; Coulthard, I.; Finnefrock, A. C.; Gordon, R.; Hallin, E.; Mass, J. Lithographically-fabricated channel arrays for confocal X-ray fluorescence microscopy and XAFS. *J. Phys.: Conf. Ser.* **2014**, *493*, 012028 (1–4).

(6) Heald, S.; Stern, E.; Brewe, D.; Gordon, R.; Crozier, D.; Jiang, D.; Cross, J. XAFS at the Pacific Northwest Consortium-Collaborative Access Team undulator beamline. *J. Synchrotron Rad.* **2001**, *8*, 342–344.

(7) Heald, S. M.; Cross, J. O.; Brewe, D. L.; Gordon, R. A. The PNC/XOR X-ray microprobe station at APS sector 20. *Nucl. Instr. Meth. Phys. Res.* **2007**, *582*, 215–217.

(8) Korbas, M.; Blechinger, S. R.; Krone, P. H.; Pickering, I. J.; George, G. N. Localizing organomercury uptake and accumulation in zebrafish larvae at the tissue and cellular level. *Proc. Natl . Acad. Sci . U. S. A.* **2008**, *105*, 12108–12112.

(9) Haller, M.; Knochel, A. X-ray fluorescence analysis using synchrotron radiation (SYXRF). *J. Trace Microprobe Tech.* **1996**, *14*, 461–488.

(10) Korbas, M.; Macdonald, T. C.; Pickering, I. J.; George, G. N.; Krone, P. H. Chemical form matters: differential accumulation of mercury following inorganic and organic mercury exposures in zebrafish larvae. *ACS Chem. Biol.* **2012**, *7*, 411–420.

(11) Antharam, V.; Collingwood, J. F.; Bullivant, J.; Davidson, M. R.; Chandra, S.; Mikhaylova, A.; Finnegan, M. E.; Batich, C.; Forder, J. R.; Dobson, J. NeuroImage High field magnetic resonance microscopy of the human hippocampus in Alzheimer's disease : Quantitative imaging and correlation with iron. *NeuroImage* **2012**, *59*, 1249–1260.

(12) Spector, R.; Keep, R. F.; Robert Snodgrass, S.; Smith, Q. R.; Johanson, C. E. A balanced view of choroid plexus structure and function: Focus on adult humans. *Exp. Neurol.* **2015**, *267*, 78–86.

(13) Pushie, M. J.; Pickering, I. J.; Martin, G. R.; Tsutsui, S.; Jirik, F. R.; George, G. N. Prion protein expression level alters regional copper, iron and zinc content in the mouse brain. *Metallomics* **2011**, *3*, 206–14.

(14) Woll, A. R.; Mass, J.; Bisulca, C.; Huang, R.; Bilderback, D. H.; Gruner, S.; Gao, N. Development of confocal X-ray fluorescence (XRF) microscopy at the Cornell high energy synchrotron source. *Appl. Phys. A* **2006**, *83*, 235–238.

(15) Bilderback, D. H. Review of capillary X-ray optics from the 2nd International Capillary Optics Meeting. *X-ray Spectrom.* **2003**, *32*, 195–207.

(16) Robison, G.; Zakharova, T.; Fu, S.; Jiang, W.; Fulper, R.; Barrea, R.; Marcus, M. A; Zheng, W.; Pushkar, Y. X-ray fluorescence imaging: a new tool for studying manganese neurotoxicity. *PloS one* **2012**, *7*, e48899–1 – e48899–9.

(17) *The Blood-Cerebrospinal Fluid Barrier*; Zheng, W.; Chodobski, A., Eds.; Taylor & Francis Group: Boca Raton, FL, 2005.

CHAPTER 3. Selenium Preferentially Accumulates in the Eye Lens Following Embryonic Exposure: A Confocal X-ray Fluorescence Imaging Study

3.1 Preface

This chapter illustrates the implementation of first confocal X-ray fluorescence setup at beamline 20ID-B, APS, as described in section 2.3.1.4. The study utilized CXFI and demonstrated first demonstration of biological CXAS in studying Se distribution and speciation in intact zebrafish larvae received elevated selenium through maternal transfer. A possible causality between the exposure to elevated Se and Se-induced ocular impairments is discussed based on a preferential accumulation of Se detected in the eye lens.

3.2 Manuscript Author Contributions

This chapter has been published in *Environmental Science and Technology:* Choudhury, S.; Thomas, J. K.; Sylvain, N. J.; Ponomarenko, O.; Gordon, R. A.; Heald, S. M.; Janz, D. M.; Krone, P. H.; Coulthard, I.; George, G. N.; Pickering, I. J. Selenium preferentially accumulates in the eye lens following embryonic exposure: A confocal X-ray fluorescence imaging study. *Environmental Science and Technology* 2015, *49*, 2255–61. DOI: 10.1021/es503848s. The chapter is reprinted with permission and has been reformatted from the published version for inclusion in the thesis.

The author contributions are provided below.

S. Choudhury prepared samples, collected and analyzed the data, and drafted the manuscript.

J. K. Thomas exposed maternal zebrafish to elevated selenium and collected eggs.

N. J. Sylvain assisted with sample preparation.

O. Ponomarenko provided a script for easier XAS data analyses.

R. A. Gordon and S. M. Heald assisted with experimental setups at the beamline.

D. M. Janz and P. H. Krone provided resources from their laboratories to produce and prepare samples.

I. J. Pickering submitted the manuscript and revisions to the journal.

I. Coulthard, G. N. George, and I. J. Pickering supervised this research, providing guidance, scientific input, comments for improving manuscript, and funding.

3.3 Abstract

Maternal transfer of elevated selenium (Se) to offspring is an important route of Se exposure for fish in the natural environment. However, there is a lack of information on the tissue specific spatial distribution and speciation of Se in the early developmental stages of fish, which provide important information about Se toxicokinetics. The effect of maternal transfer of Se was studied by feeding adult zebrafish a Se-elevated or a control diet followed by collection of larvae from both groups. Novel confocal synchrotron-based techniques were used to investigate Se within intact preserved larvae. CXFI was used to compare Se distributions within specific planes of an intact larva from each of the two groups. The elevated Se treatment showed substantially higher Se levels than the control; Se preferentially accumulated to highest levels in the eye lens, with lower levels in the retina, yolk and other tissues. CXAS was used to determine that the speciation of Se within the eye lens of the intact larva was a selenomethionine-like species. Preferential accumulation of Se in the eye lens may suggest a direct cause-and-effect relationship between exposure to elevated Se and Se induced ocular impairments reported previously. This study illustrates the effectiveness of confocal X-ray fluorescence methods for investigating trace element distribution and speciation in intact biological specimens.

3.4 Introduction

Selenium (Se) is an essential trace element but exhibits toxicity at elevated levels with only a narrow margin in concentration between its essentiality and toxicity.[1–6] Elevated Se in the aquatic environment mainly originates from its mobilization via anthropogenic activities such as metal and coal mining, petroleum refining and agricultural drainage.[1–7] Trace amounts entering the aquatic environment tend to bioaccumulate through aquatic food webs, accumulating to the highest levels in top predators such as fish, aquatic birds and amphibians.[1–7] The adverse effect

of elevated Se in fish can manifest itself in different ways, including developmental abnormalities,[1] decreased swim performance,[5,6] reproductive failure[2] and ocular problems.[2] Maternal transfer of Se is a major route of environmental exposure in fish, in which dietary consumption of higher levels of Se by adult female fish results in incorporation of elevated Se in eggs during vitellogenesis or yolk deposition.[8] Developing embryos are sensitive to the elevated Se in the yolk; developmental problems can occur during early development as yolk is utilized as an energy source.[8] An understanding of the Se toxicokinetics following such maternal transfer of elevated Se is therefore essential in order to explain why certain developmental problems would occur, but to date information regarding Se distribution and speciation during this critical early life stage in fish is lacking. It is likely that, following embryonic exposure, there will be a significant spatial heterogeneity in Se distribution and speciation among different larval tissues. The ability to reveal this information will significantly contribute to the understanding of Se toxicokinetics, and is the subject of this paper.

Zebrafish (*Danio rerio*) is a common model organism for the study of vertebrate toxicology.[9] Zebrafish have been used to evaluate the toxicity of various agents[9] including Se.[5,6,10] Here, we investigate the effect on zebrafish larva of embryonic exposure to elevated Se by examining larval Se distribution and speciation. This was achieved by exposing adult female zebrafish to a diet spiked with selenomethionine, chosen because it is the major form of organoselenium in aquatic food and tissues of invertebrates and fish.[3,11–13] Although maternal dietary exposure to other Se species will occur, dietary selenomethionine thus represents the dominant Se exposure scenarios of adult and embryo-larval fishes inhabiting many Se elevated aquatic environments. An environmentally relevant dietary concentration of 30 μg Se/g dry mass[5,6,11] was chosen based on similar concentrations reported in fish prey collected from Se affected sites.[1,2,14] Previous studies have demonstrated that similar exposure via maternal transfer resulted in egg Se concentrations of 21.9 and 34.1 μg Se/g dry mass when adult zebrafish were fed respectively 26.6 and 27.5 μg Se/g dry mass selenomethionine-spiked diets.[11,15] These previous studies also have shown that exposure to these levels of selenomethionine resulted in immediate and persistent toxicities, such as increased larval deformity and mortality, and significantly reduced swimming performance and tailbeat amplitude in first generation larval fish.[11,15]

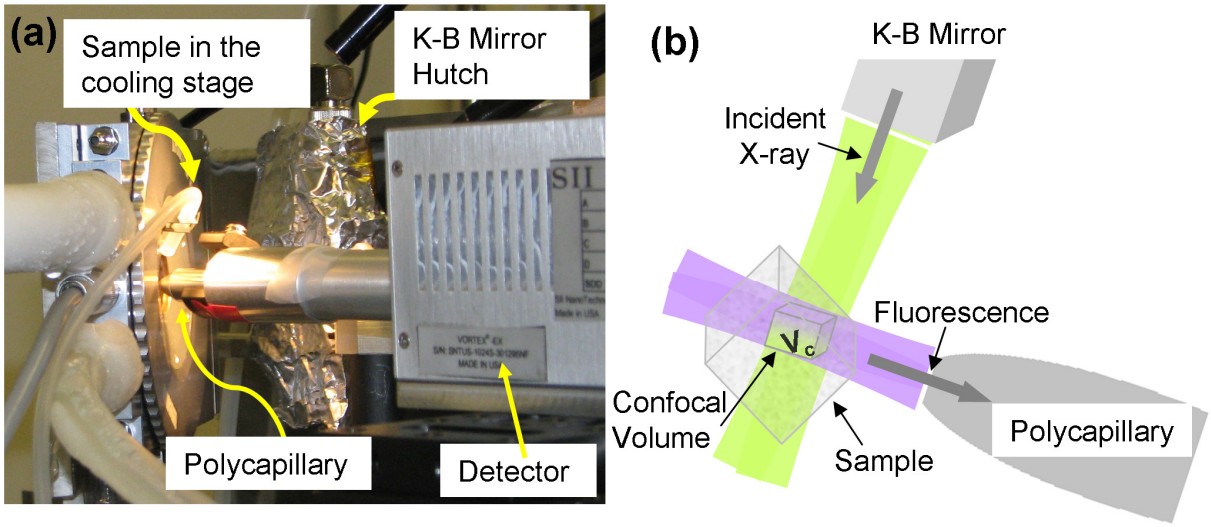

Figure 3.1 Experimental arrangement for CXFI at beamline 20-ID, APS. (a) A photograph showing the arrangement of K-B mirror (incident focusing optic), polycapillary (detection focusing optic), sample stage and detector. (b) Focal spots of two focusing optics intersect to form the confocal volume (Vc) inside the sample. In confocal mode, detection is limited to the confocal volume.

In this study, we demonstrate the use of synchrotron-based CXFI and CXAS to determine the tissue specific distribution and speciation of Se, respectively. Although conventional XFI has been used previously to study elements in sectioned zebrafish larvae,[16–19] CXFI[20–22] enables the study of a specific layer within an intact larva, excluding unwanted signal contribution from outside of the confocal volume to yield an improved signal-to-noise ratio. In addition, the use of confocal geometry with XAS gives information on the chemical form in a specific volume element of the larva. By using confocal synchrotron X-ray techniques to study zebrafish larvae following maternal transfer of Se, we observed that the highest degree of Se accumulation occurs in the eye lens, in a selenomethionine-like form. The observed preferential accumulation in the eye lens may suggest a direct causality between the exposure to elevated Se and the ocular impairments, as we will discuss.

3.5 Materials and Methods

Zebrafish Preparation: Adult zebrafish, purchased from a local supplier, were housed in an environmental chamber with controlled temperature (28.0 ± 1.0 °C) and photoperiod (14 h light, 10 h dark). Fish were introduced into four 25 L glass aquaria (12 fish/tank) with continuous aeration and filtration, after which treatments were randomly assigned to aquaria, with n = 2 aquaria replicates per treatment. During a 2 week acclimatization to laboratory conditions, fish were fed Nutrafin basic flake food (Hagen Inc., Montreal, QC, Canada).

Diet Preparation and Feeding: The experimental diet was prepared by dissolving seleno-L-methionine (purity > 98%, Sigma Aldrich, Oakville, ON, Canada) in deionized distilled water and then adding to Nutrafin flake food (30 µg Se/g dry mass), as described previously.[5,6] The control diet was prepared by adding an equivalent volume of water without selenomethionine to food. Food was lyophilized in a freeze-dryer (Dura- Dry MP, FTS Systems, Stone Ridge, NY, USA). Freeze-dried diets were crushed into flakes and stored at -20 °C in airtight containers.

Se Exposure: All methods applied in the present study were approved by the University of Saskatchewan's Animal Research Ethics Board, and adhered to the Canadian Council on Animal Care guidelines for humane animal use. Fish were fed twice daily (5% body weight/day ration) with either control or selenomethionine spiked food for 25 days. Fish were allowed to feed for 2 h, after which excess food was siphoned from the aquarium bottom. During the feeding experiment, 75% of water was renewed from each aquarium every day to minimize aqueous selenomethionine exposure to fish.[6] After 25 days, adult fish from each treatment group were bred; fertilized eggs were collected, cleaned and staged following standard procedures.[23] After staging, the two groups were reared in separate Petri dishes at 28°C until 72 h post fertilization (hpf).

Sample Preparation: Fish larvae samples were prepared for XFI measurements following an established protocol of zebrafish fixation and embedding described elsewhere.[16] Larvae (72 hpf) from both Se and control groups were fixed in 4% paraformaldehyde for 18 h at 4 °C. Fixed larvae were then dehydrated in a series of solutions of ethanol (0%, 25%, 50%, 75% and 100%) in Phosphate Buffered Saline Tween (PBST; 30 mM PBS and 0.1% Tween 20) solution for 5

min each, and stored in 100% ethanol at −20 °C. Prior to embedding, stored larvae were rehydrated in PBST following the reverse steps of dehydration. Initial embedding of larvae was in 1% agarose gel. Next, the gel blocks of larvae were dehydrated in 100% ethanol by gentle shaking for 8 h at 4 °C. The blocks were then infiltrated overnight in an infiltration solution (prepared by adding 100 mL of JB-4 solution A to 1.25 g of catalyst followed by 10 min of stirring) on a rotating stirrer at 4 °C, followed by an additional 6 h with fresh solution. For JB-4 embedding, infiltrated blocks were placed in embedding molds filled with mounting solution (prepared by adding 1 mL of JB-4 solution B to 25 mL of fresh infiltration solution) and left overnight at 4 °C. Following solidification, polymer blocks containing fish larvae were obtained. This sample preparation procedure can be detrimental to the elemental chemical form; hence care must be taken in interpretation of the results. Next, a Hillquist thin section machine with an ultrathin diamond blade was used to cut the polymer blocks into pieces, each containing a single larva. In the final step carried out under the microscope, excess polymer around each larva was trimmed off using a straight edge razor blade.

Data Collection: Synchrotron-based CXFI was used to determine the elemental distribution within the samples. Measurements were carried out at the 20ID-B beamline of the APS at Argonne National Laboratory, Argonne, IL with the storage ring operating in continuous top-up mode at 102 mA and 7.0 GeV. The incoming beam was tuned to the desired excitation energy by using a liquid-nitrogen-cooled Si (111) double crystal monochromator with the second crystal detuned by 15% to reduce harmonic contamination. A microbeam spotsize of 5×5 μm^2 was produced using Rh-coated silicon K-B style focusing mirrors, which also served to provide additional harmonic rejection. The incident energy was set at 13.45 keV with an estimated intensity of ~10^{12} photons/s. Samples were mounted on a Linkam THMSG 600 stage at 45° to the incident beam and were kept cool at −80 °C by maintaining a constant flow of liquid N2. The Se Kα emission and other fluorescence X-rays were monitored by a Si-drift Vortex detector (SII NanoTechnology USA Inc., CA, USA) placed at 90° with respect to the incident X-ray beam. Spectral regions of interest were set for the Kα fluorescence lines of Se, zinc (Zn), iron (Fe), copper (Cu) and calcium (Ca) as well as scatter. A polycapillary (XOS) of nominal 25 μm focal spot (at Mo Kα, 17.4 keV) on the sample was mounted in front of the detector to complete the confocal geometry, which yielded a confocal volume of approximately $5 \times 5 \times 40$ μm^3 at Se Kα

(11.2 keV). Maps were obtained by spatially rastering the sample through the confocal volume. The experimental arrangement is presented in Figure 3.1.

The CXAS data from zebrafish eye lens at the Se Kedge were collected with the above setup. The spectra were energy calibrated with reference to the first inflection point of a hexagonal elemental Se foil (EXAFS Materials Inc.), which was assumed to be 12 658.0 eV. Near-edge spectra were taken with 0.5 eV steps through the near-edge region and to 150 eV below and 137 eV above for linear background removal and normalization to edge jump. Spectra for the Se standards were collected at beamline 7-3 at SSRL, as previously described.[24,25]

Data Analysis: XFI data were analyzed using the SMAK software (http://home.comcast.net/~sam_webb/smak.html). Fluorescence counts were normalized to the incident intensity measured simultaneously using an ionization chamber and were background-corrected by subtracting the average intensity from pixels outside the image of the sample. Intensity attenuation of the incident and fluorescent beams arising from the additional depth into the sample was calculated using the Beer-Lambert law, which can be expressed as $A = \log(I_0/I) = \sigma\rho t$, where A is the absorbance and I_0 and I are the intensities measured before and after crossing the absorbing medium. The additional path length of X-rays through the medium, t is related to the separation of the confocal planes in the experiment. The density of the medium, ρ, is approximated as that of PMMA (poly (methyl methacrylate), the embedding material). Values of σ, the total absorption cross section of the medium, for both incident and fluorescent X-ray energies were calculated using the McMaster program in EXAFSPAK (http://www-ssrl.slac.stanford.edu/exafspak.html). Intensities of the maps of all optical sections were placed in same relative scale using the SMAK software. XAS data were analyzed using the XAFSPAK suite of programs.

3.6 Results and Discussion

3.6.1 CXFI

XFI[26] without confocal geometry detects elements along the entire path of the beam. All maps presented herein were measured in confocal mode,[21] with fluorescence detected only from

the microscopic confocal volume of approximately 5 × 5 × 40 μm^3 defined by the incident and focusing optics. There are several advantages to this approach. Confocal geometry leads to an increase of signal-to-background ratio, as the polycapillary rejects emission or scatter originating from outside of the confocal volume.[20–22] In addition, it allows the selection of a specific plane within an intact, unsectioned object, rather than measuring fluorescence from every point in the trajectory of the incident beam.[20–22] Our ability to use the intact zebrafish sample enabled us to avoid sample sectioning, which is necessitated for optimum spatial resolution in conventional XFI. It also allowed the possibility of investigating a generic volume element anywhere in the sample. Additionally, the use of an intact sample ensured the integrity of the sample by protecting it from any possible tissue damage or contamination that might result from physical sectioning.

The tissue specific spatial distribution of Se accumulation was determined in 72 hpf zebrafish larvae, for which Se had been maternally transferred by feeding adult females selenomethionine-spiked food or for which adult females had received a baseline Se diet. Figure 3.2 shows CXFI maps obtained for both the control and Se-group larvae. The upper two panels represent the depth-selective measurements of two consecutive coronal optical sections, separated by 60 μm, within an intact Se group larva. To compare the Se level with the control group, maps from a control fish larva are presented in the bottom panels. The spatial resolution for all scans, both horizontally and vertically, was 5 μm with an integration time per point of 0.5 s; the average total measurement time for each section was approximately 9 h. Along with the Se map in the left column, Figure 3.2 also shows the distribution of Zn from the same planes. Maps of other elements (e.g., Fe, Cu and Ca) are not shown, as they displayed low fluorescent intensity and no significant anatomical variation; low abundance of these elements in zebrafish larvae is in agreement with previous studies.[16] The color legend at the bottom of Figure 3.2 shows the color scale representation of the relative elemental concentrations, which are plotted on the same relative scale for a given element. The fluorescence signal depends not only on the amount of the element within the confocal volume but also on the attenuation of both incident and fluorescent beams by the object; it is thus complex to quantify total amounts of elements. However, the incident and fluorescent X-ray beams for the second optical section of the Se group, displayed in the middle panel of Figure 3.2, exhibited some additional attenuation, as this section is situated

60 μm deeper into the sample relative to the first section. This additional attenuation of the incident and fluorescent X-ray beams is accounted for, as described in the data analysis section.

Several anatomical features, such as eye lens (EL), retina (RT), ear (ER), brain (BR), swim bladder (SB), pectoral fins (PF) and yolk (YK) are identified (Figure 3.2). It is clear that the distributions of Se and Zn are spatially heterogeneous and differ from each other. Zn is relatively abundant in biological tissues and is observed throughout the body. However, elevated levels of Zn are observed in the yolk sac and retinal pigmented epithelium, as observed previously.[16] Se also appears at considerably higher levels in the yolk compared to most other tissues; this is of significance because all of the excess Se initially was transferred maternally to the yolk, which is utilized as the energy source during the early development of larva. The observed lumpiness in the yolk map represents the natural heterogeneity of the yolk. However, the most striking observation is the preferential accumulation of Se in the eye lens, with the highest concentrations in the lens core, and moderate concentrations in the lens epithelium. As expected, the distributions of elements for both eyes are similar. Because the data collection time for each optical section (9 h) precluded the detailed scanning of an entire larva, additional optical sections were scanned with a coarser step size (not shown) but no other region of elevated Se was observed. The bottom panels show the distribution of Zn and Se in the section of a control fish larva (Figure 3.2). The distribution of Zn resembles the pattern observed in the Se-group maps. The concentration of Se is close to the background level in this case, with intensities of all maps placed for comparison on the same relative scale as discussed in the data analysis section; the inset shows the same Se map with intensity increased by a factor of 10. In a previous study using similar treatment conditions, the Se concentration in eggs from fish fed a control diet was found to be 2.1 ± 0.1 μg Se/g dry mass, compared with 34.1 μg Se/g dry mass for eggs from the selenomethionine-spiked diet.[11,15] Thus, our observed intensity differential is consistent with projected concentrations in the larva, assuming proportionately similar transfer from egg to larva in both treatments. The inset shows that the low-level Se in the control is broadly distributed in the yolk and retina, but is not observed in the eye lens, which is identified within the characteristic Zn retina distribution. From the comparison between maps from the maternally fed Se group and control group larvae, it can be concluded that the Se observed in the maps of Se group originates from maternal transfer.

3.6.2 CXAS

XAS is a sophisticated tool that can be used to determine the chemical forms of elements.[24,25,27,28] The near edge (within approximately 50 eV of the absorption edge) part of an XAS spectrum can be particularly sensitive to the type of chemical species of the element concerned.[24,25,27,28] A "fingerprint" spectrum obtained for a sample of unknown composition can be compared with standard spectra of known compounds to determine the type of chemical species. In the case of a mixture of chemical forms, quantitative information about the different chemical species can be obtained from least-squares curve fitting of a linear combination of standard spectra.[27,28]

In this study, the use of the confocal detection mode allowed depth-selective μ-XAS from a micro volume that enabled higher detection sensitivity compared to conventional XAS on a thin section sample due to superior rejection of background signal. The confocal geometry supported ease of return to a specific volume element of interest (the coordinates of high Se concentration points, in this case) in order to perform spatially resolved XAS measurements. Although CXFI and fluorescence tomography[29] both can measure three dimensional elemental distributions, spatially resolved XAS of a dilute element would be highly challenging in tomography since reconstruction of spectra from multiple angles is required. Figure 3.3 compares Se K near-edge XAS spectra of the zebrafish larva eye lens with selected Se model compounds. Distinct variations in the Se K edge features among different model compounds are apparent,[25,28] which are indicative of the rich variability in the local electronic structures. The spectrum of the eye lens shows closest resemblance with that obtained from selenomethionine in aqueous solution. A small difference may be due to the eye lens and standard spectra being collected at different beamlines. To simulate the different beamline resolution due to the use of different monochromator crystal cuts on SSRL 7-3 and APS 20-ID, the selenomethionine spectrum has been broadened by convolution with a 1.5 eV half-width-half-maximum Gaussian

that has resulted in improvement in resemblance. Including spectra of other Se species did not improve the fit.

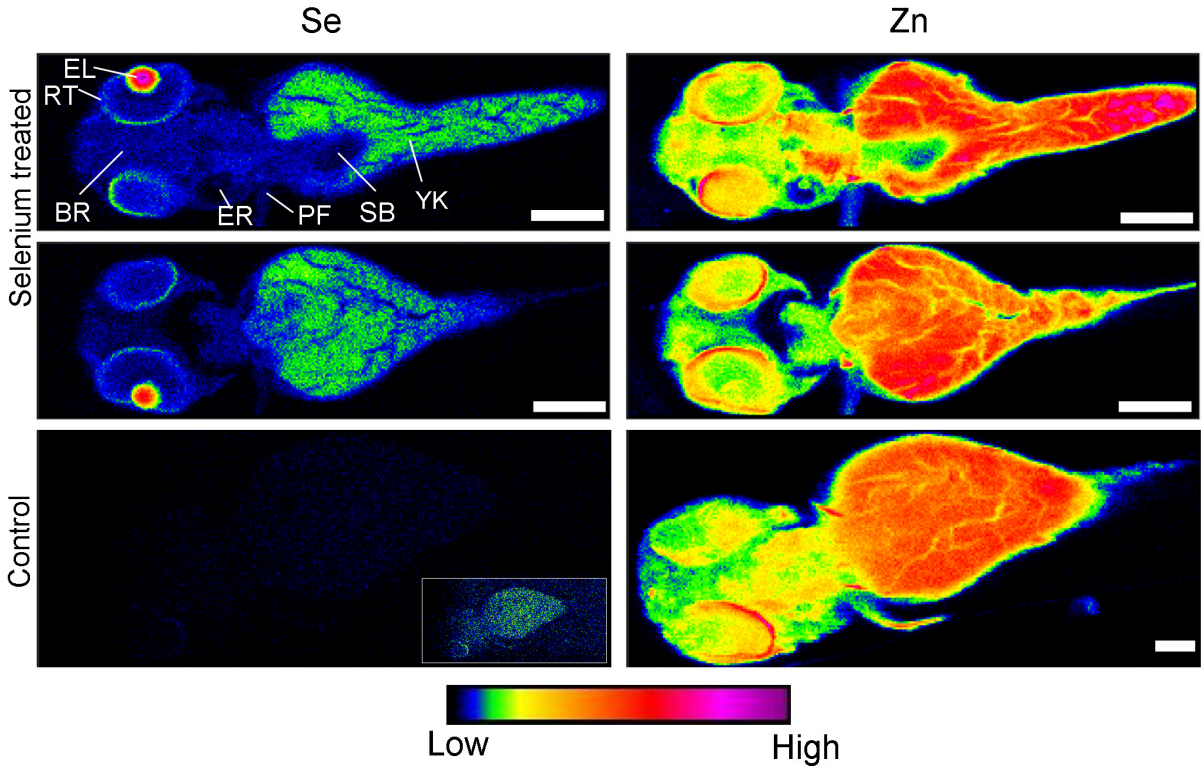

Figure 3.2 CXFI maps showing the distribution of Se and Zn in intact (not physically sectioned) 72 hpf zebrafish larvae. Bottom row: control zebrafish, scalebar (same for both Se and Zn) = 100 μm. Upper rows: two confocal sections, displaced by 60 μm, of a larva that received Se through maternal transfer, scalebar =200 μm. In each row, left and right images show Se and Zn, respectively. Se panels are plotted on same relative intensity scale (see text for details). Inset shows control Se image displayed with greater (×10) sensitivity. Brain (BR), retina (RT), eye lens (EL), ear (ER), pectoral fin (PF), swim bladder (SB), yolk (YK).

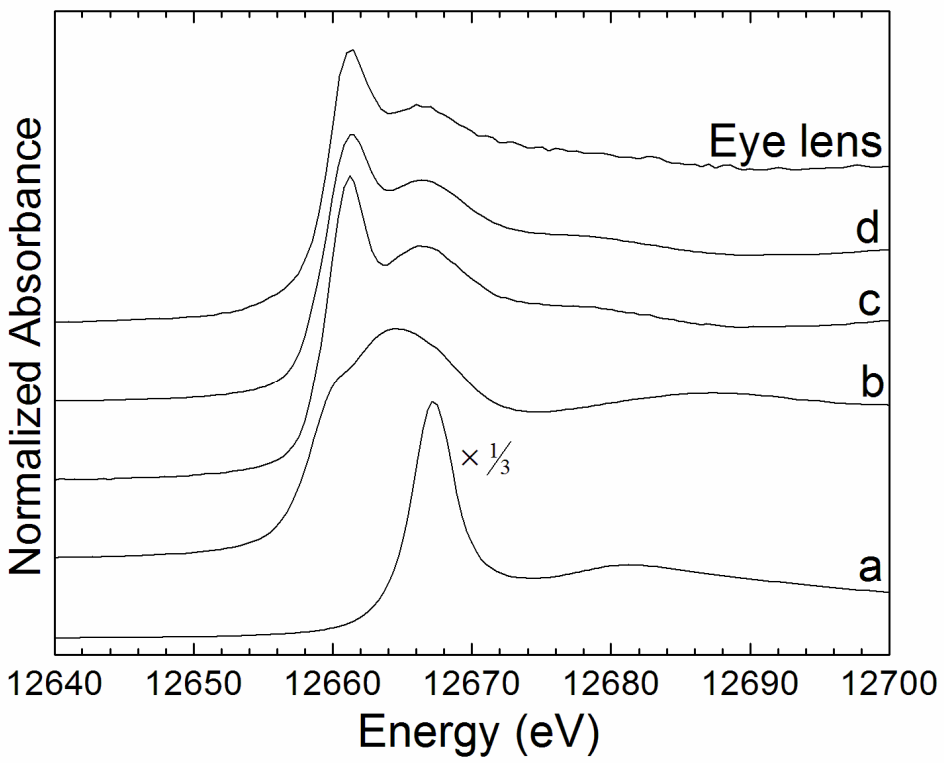

Figure 3.3 Comparison of Se K-edge XAS spectra of eye lens measured in confocal mode with selected standard Se species (a, selenate; b, selenocysteinate; c, selenomethionine; d, broadened selenomethionine) measured using bulk XAS. The eye lens spectrum shows the best correspondence with the broadened selenomethionine spectrum; the broadening by convolution with a 1.5 eV half-width-half-maximum Gaussian simulates the different beamline resolution due to the use of different monochromator crystal cuts on SSRL 7-3 and APS 20-ID. Vertical offset is added for better comparison.

3.6.3 Preferential accumulation in the eye lens

Although more statistics are required for confirmation, our observations strikingly show that the eye lens is the main target for excess Se at this developmental stage. We hypothesize that the preferential accumulation of Se in the eye lens is due to substitution for the naturally occurring sulfur (S) in the eye lens. Reportedly, γ-crystallin constitutes approximately 71% of total zebrafish eye lens protein;[30,31] moreover, γ-crystallin contains S-containing methionine and cysteine amino acid groups.[32] Although S cannot be detected in our confocal experiment because fluorescence from this light element in our buried sections is too strongly absorbed by the matrix,

the presence of endogenous S in the eye lens has been observed previously in XFI elemental mapping of a section of control zebrafish eye.[16,17] The chemical similarity between selenomethionine and methionine, and the ease with which selenomethionine can substitute for methionine, has resulted in its routine substitution as a method to solve the phase-problem in X-ray crystallography of biological macromolecules.[33] The incorporation of selenocysteine in place of cysteine can also be used but is relatively difficult as it confers high reactivity.[34] Double labeling using both selenomethionine and selenocysteine also can be used when there are too few methionine residues in the protein.[33] As selenomethionine readily replaces methionine, it is highly likely that the chemical form of Se in the eye lens would be selenomethionine-like, as determined in our XAS experiment. The ease of potential incorporation of Se into S-rich proteins in the eye is also facilitated by the larval life stage at which establishment of vision is a high priority in order to facilitate food acquisition and to evade predation. The cells in the eye lens are considered one of the most rapidly dividing cell types[16] and therefore, it is likely that the excess Se is preferably incorporated into proteins by these cell types. More work is needed to investigate this hypothesis.

The investigation of organomercury uptake and accumulation in zebrafish larvae under different experimental conditions also reported preferential accumulation in the eye but in different cell types.[16–18] In these experiments, larvae were directly exposed to methylmercury in water for 48 h. Following exposure, XFI showed preferential accumulation of methylmercury in lens epithelial cells,[16] whereas a later higher resolution experiment more precisely located accumulated mercury to the secondary fiber cells immediately underlying the lens epithelial cells.[18] Comparing previous methylmercury work with the present study, both routes and the times of exposure differ, with exogenous solution and defined time periods in the mercury study contrasting with maternal transfer via the yolk sac and consequent continuous exposure in the present study. Although the cell types targeted and the physiological mechanisms both differ, it is noteworthy that both organoselenium and organomercury species target the eye lens.

3.6.4 Connection to ocular impairments

Our observations suggest that the observed accumulation of Se in the eye lens may have a direct connection to previously reported ocular impairments related to elevated Se both in

fish[1,2,5,6,35] and in humans.[36–38] Se is discussed in connection with ocular impairments in many reports, where both deficiency and excess of Se are demonstrated as potential risks for cataractogenesis.[1,2,5,6,35–37,39] As an essential trace element, Se prevents cataract formation by preventing oxidative damage; thus, Se deficiency may cause cataractogenesis.[40] Conversely, excess Se is found to be responsible for the formation of cataracts presumably due to redox cycling.[37] Other ocular impairments, such as glaucoma in humans,[36] and exophthalmia and microphthalmia in fish,[2] are also found to have a connection with exposure to excess Se. High Se content in the human eye has been shown to be related to cataracts.[38] It seems likely that the direct incorporation of Se into the eye lens, which we hypothesize is due to selenomethionine incorporation into the lens crystallin proteins, may be the cause of these ocular impairments. It is known that the oxidation of protein methionine to methionine sulfoxide is a major contributing factor in cataract formation,[41] whereas oxidation of selenomethionine is easier than its sulfur counterparts.[42] Hence, we hypothesize that differing susceptibilities of selenomethionine to oxidation and reduction compared with methionine may form the basis of the mechanism of Se-induced cataract formation. Further studies are needed to delineate the mechanism, which we intend to explore in future work.

3.6.5 Environmental implications

In nature, maternal transfer of elevated Se to offspring is a major route of Se exposure. Although based on limited observations, our work shows that following the maternal transfer, excess Se is widely distributed in the larval body but to the highest levels within the eye lens in the form of selenomethionine. As selenomethionine is more easily oxidized than its sulfur counterparts, it is highly likely that oxidation of selenomethionine would disrupt the strictly organized structure of the eye lens protein, crystallin. As a consequence, opacification of the eye lens or cataract would occur. Although more work is necessary for a conclusive statement, our results suggest that there is a causative relation between this preferential accumulation and previously reported cataracts in fish inhabiting Se elevated aquatic environments. Our work also demonstrates the effectiveness of confocal X-ray techniques to study trace element distribution and speciation in intact biological tissues.

3.7 Acknowledgements

We thank members of the George, Pickering, Krone, and Janz research groups at the University of Saskatchewan for their assistance and helpful discussions. S.C. is a Fellow in the Canadian Institutes of Health Research (CIHR) Training grant in Health Research Using Synchrotron Techniques (CIHR-THRUST). G.N.G. and I.J.P. are Canada Research Chairs. This work was supported by the Natural Sciences and Engineering Research Council of Canada (NSERC), the CIHR and the Saskatchewan Health Research Foundation. This work was also supported by the Canada Foundation for Innovation through funding for BioXAS: Life Science Beamline for X-ray Absorption Spectroscopy at the Canadian Light Source Inc. CXFI data were collected at beamline 20ID-B, Advanced Photon Source (APS). Sector 20 facilities at the APS, and research at these facilities, are supported by the U.S. Department of Energy (DOE) - Basic Energy Sciences, the Canadian Light Source and its funding partners, the University of Washington, and the Advanced Photon Source (APS). Use of the APS, an Office of Science User Facility operated for the U.S. DOE Office of Science by Argonne National Laboratory, was supported by the U.S. DOE under Contract No. DE-AC02- 06CH11357. Standard spectra were measured at the Stanford Synchrotron Radiation Lightsource (SSRL), a Directorate of SLAC National Accelerator Laboratory and an Office of Science User Facility operated for the U.S. DOE Office of Science by Stanford University. The SSRL Structural Molecular Biology Program is supported by the DOE Office of Biological and Environmental Research, and by the National Institutes of Health (NIH), National Institute of General Medical Sciences (NIGMS) (including P41GM103393). The contents of this publication are the responsibility of the authors and do not necessarily represent the official views of NIGMS or NIH.

3.8 References

(1) Lemly, A. D. A teratogenic deformity index for evaluating impacts of selenium on fish populations. *Ecotox. Environ. Safe.* **1997**, *37*, 259–266.

(2) Lemly, A. D. Symptoms and implications of selenium toxicity in fish: the Belews lake case example. *Aquat. Toxicol.* **2002**, *57*, 39–49.

(3) Phibbs, J.; Wiramanaden, C. I. E.; Hauck, D.; Pickering, I. J.; Liber, K.; Janz, D. M. Selenium uptake and speciation in wild and caged fish downstream of a metal mining and milling discharge. *Ecotox. Environ. Safe.* **2011**, *74*, 1139–1150.

(4) Muscatello, J. R.; Belknap, A. M.; Janz, D. M. Accumulation of selenium in aquatic systems downstream of a uranium mining operation in northern Saskatchewan, Canada. *Environ. Pollut.* **2008**, *156*, 387–393.

(5) Thomas, J. K.; Janz, D. M. Dietary selenomethionine exposure in adult zebrafish alters swimming performance, energetics and the physiological stress response. *Aquat. Toxicol.* **2011**, *102*, 79–86.

(6) Thomas, J. K.; Wiseman, S.; Giesy, J. P.; Janz, D. M. Effects of chronic dietary selenomethionine exposure on repeat swimming performance, aerobic metabolism and methionine catabolism in adult zebrafish (*Danio rerio*). *Aquat. Toxicol.* **2013**, *130-131*, 112–122.

(7) Lemly, A. D. Ecological basis for regulating aquatic emissions from the power industry: the case with selenium. *Regul. Toxicol. Pharm.* **1985**, *5*, 465–486.

(8) Janz, D. M. *Fish Physiology: Homeostasis and Toxicology of Essential Metals*; Elsevier, San Diego, CA, 2012; pp. 327–374.

(9) Hill, A. J.; Teraoka, H.; Heideman, W.; Peterson, R. E. Zebrafish as a model vertebrate for investigating chemical toxicity. *Toxicol. Sci.* **2005**, *86*, 6–19.

(10) Ma, Y.; Wu, M.; Li, D.; Li, X.; Li, P.; Zhao, J.; Luo, M.; Guo, C.; Gao, X.; Lu, C.; Ma, X. Embryonic developmental toxicity of selenite in zebrafish (*Danio rerio*) and prevention with folic acid. *Food Chem. Toxicol.* **2012**, *50*, 2854–2863.

(11) Thomas, J. K. Effects of dietary and in ovo selenomethionine exposure in zebrafish (*Denio rerio*). Ph.D. Thesis, University of Saskatchewan, Saskatoon, SK, 2014.

(12) Misra, S.; Peak, D.; Chen, N.; Hamilton, C.; Niyogi, S. Tissue-specific accumulation and speciation of selenium in rainbow trout (*Oncorhynchus mykiss*) exposed to elevated dietary selenomethionine. *Comp. Biochem. Phys. C* **2012**, *155*, 560–565.

(13) Fan, T. W.-M.; Teh, S. J.; Hinton, D. E.; Higashi, R. M. Selenium biotransformations into proteinaceous forms by foodweb organisms of selenium-laden drainage waters in California. *Aquat. Toxicol.* **2002**, *57*, 65–84.

(14) Hamilton, S. J. Review of selenium toxicity in the aquatic food chain. *Sci. Total Environ.* **2004**, *326*, 1–31.

(15) Thomas, J. K.; Janz, D. M. In ovo exposure to selenomethionine via maternal transfer increases developmental toxicities and impairs swim performance in F1 generation zebrafish (*Danio rerio*). *Aquat. Toxicol.* **2014**, *152*, 20–29.

(16) Korbas, M.; Blechinger, S. R.; Krone, P. H.; Pickering, I. J.; George, G. N. Localizing organomercury uptake and accumulation in zebrafish larvae at the tissue and cellular level. *Proc. Natl . Acad. Sci . U. S. A.* **2008**, *105*, 12108–12112.

(17) Korbas, M.; Krone, P. H.; Pickering, I. J.; George, G. N. Dynamic accumulation and redistribution of methylmercury in the lens of developing zebrafish embryos and larvae. *J. Biol. Inorg. Chem.* **2010**, *15*, 1137–1145.

(18) Korbas, M.; Lai, B.; Vogt, S.; Gleber, S.-C.; Karunakaran, C.; Pickering, I. J.; Krone, P. H.; George, G. N. Methylmercury targets photoreceptor outer segments. *ACS Chem. Biol.* **2013**, *8*, 2256–2263.

(19) Korbas, M.; Macdonald, T. C.; Pickering, I. J.; George, G. N.; Krone, P. H. Chemical form matters: differential accumulation of mercury following inorganic and organic mercury exposures in zebrafish larvae. *ACS Chem. Biol.* **2012**, *7*, 411–420.

(20) Vekemans, B.; Vincze, L.; Brenker, F. E.; Adams, F. Processing of three-dimensional microscopic X-ray fluorescence data. *J. Anal. At. Spectrom.* **2004**, *19*, 1302–1308.

(21) Janssens, K.; Alfeld, M.; Van der Snickt, G.; De Nolf, W.; Vanmeert, F.; Radepont, M.; Monico, L.; Dik, J.; Cotte, M.; Falkenberg, G.; Miliani, C.; Brunetti, B. G. The use of synchrotron radiation for the characterization of artists' pigments and paintings. *Annu. Rev. Anal. Chem.* **2013**, *6*, 399–425.

(22) Woll, A. R.; Mass, J.; Bisulca, C.; Huang, R.; Bilderback, D. H.; Gruner, S.; Gao, N. Development of confocal X-ray fluorescence (XRF) microscopy at the Cornell high energy synchrotron source. *Appl. Phys. A* **2006**, *83*, 235–238.

(23) Kimmel, C. B.; Ballard, W. W.; Kimmel, S. R.; Ullmann, B.; Schilling, T. F. Stages of embryonic development of the zebrafish. *Dev. Dynam.* **1995**, *203*, 253–310.

(24) Pickering, I. J.; Wright, C.; Bubner, B.; Ellis, D.; Persans, M. W.; Yu, E. Y.; George, G. N.; Prince, R. C.; Salt, D. E. Chemical form and distribution of selenium and sulfur in the selenium hyperaccumulator *Astragalus bisulcatus*[1]. *Plant Physiol.* **2003**, *131*, 1460–1467.

(25) Pickering, I. J.; George, G. N.; Van Fleet-Stalder, V.; Chasteen, T. G.; Prince, R. C. X-ray absorption spectroscopy of selenium-containing amino acids. *J. Biol. Inorg. Chem.* **1999**, *4*, 791–794.

(26) Pushie, M. J.; Pickering, I. J.; Korbas, M.; Hackett, M. J.; George, G. N. Elemental and chemically specific X-ray fluorescence imaging of biological systems. *Chem. Rev.* **2014**, *114*, 8499–8541.

(27) George, G. N.; Singh, S. P.; Myers, G. J.; Watson, G. E.; Pickering, I. J. The chemical forms of mercury in human hair: a study using X-ray absorption spectroscopy. *J. Biol. Inorg. Chem.* **2010**, *15*, 709–715.

(28) George, G. N.; MacDonald, T. C.; Korbas, M.; Singh, S. P.; Myers, G. J.; Watson, G. E.; O'Donoghue, J. L.; Pickering, I. J. The chemical forms of mercury and selenium in whale skeletal muscle. *Metallomics* **2011**, *3*, 1232–1237.

(29) Jonge, M. D. De; Holzner, C.; Baines, S. B.; Twining, B. S.; Ignatyev, K.; Diaz, J.; Howard, D. L.; Legnini, D.; Miceli, A.; Mcnulty, I.; Jacobsen, C. J.; Vogt, S. Quantitative 3D elemental microtomography of *Cyclotella meneghiniana* at 400-nm resolution. *Proc. Natl . Acad. Sci . U. S. A.* **2010**, *107*, 15676–15680.

(30) Wages, P.; Horwitz, J.; Ding, L.; Corbin, R. W.; Posner, M. Changes in zebrafish (*Danio rerio*) lens crystallin content during development. *Mol. Vis.* **2013**, *19*, 408–417.

(31) Lin, Y.-R.; Mok, H.-K.; Wu, Y.-H.; Liang, S.-S.; Hsiao, C.-C.; Huang, C.-H.; Chiou, S.-H. Comparative proteomics analysis of degenerative eye lenses of nocturnal rice eel and catfish as compared to diurnal zebrafish. *Mol. Vis.* **2013**, *19*, 623–637.

(32) Mahler, B.; Chen, Y.; Ford, J.; Thiel, C.; Wistow, G.; Wu, Z. Structure and dynamics of the fish eye lens protein, γM7-crystallin. *Biochemistry* **2013**, *52*, 3579–3587.

(33) Strub, M.-P.; Hoh, F.; Sanchez, J.-F.; Strub, J. M.; Böck, A.; Aumelas, A.; Dumas, C. Selenomethionine and selenocysteine double labeling strategy for crystallographic phasing. *Structure* **2003**, *11*, 1359–1367.

(34) Johansson, L.; Gafvelin, G.; Arnér, E. S. J. Selenocysteine in proteins-properties and biotechnological use. *Biochim. Biophys. Acta* **2005**, *1726*, 1–13.

(35) Woock, S. E.; Garrett, W. R.; Partin, W. E.; Bryson, W. T. Decreased survival and teratogenesis during laboratory selenium exposures to bluegill, *Lepomis macrochirus. B. Environ. Contam. Tox.* **1987**, *39*, 998–1005.

(36) Bruhn, R. L.; Stamer, W. D.; Herrygers, L. A.; Levine, J. M.; Noecker, R. J. Relationship between glaucoma and selenium levels in plasma and aqueous humour. *Brit. J. Ophthalmol.* **2009**, *93*, 1155–1158.

(37) Flohé, L. Selenium, selenoproteins and vision. *Dev. Ophthalmol.* **2005**, *38*, 89–102.

(38) Dawczynski, J.; Winnefeld, K.; Königsdörffer, E.; Augsten, R.; Blum, M.; Strobel, J. Selenium and cataract-risk factor or useful dietary supplement? *Klin. Monbl. Augenheilkd.* **2006**, *223*, 675–680.

(39) Ostadalova, I.; Babicky, A.; Obenberger, J. Cataract induced by administration of a single dose of sodium selenite to suckling rats. *Specialia* **1978**, *15*, 222–223.

(40) Srivastava, S. K.; Lal, A. K.; Ansari, N. H. Defense system of the lens against oxidative damage: effect of oxidative challenge on cataract formation in glutathione peroxidase deficient-acatalasemic mice. *Exp. Eye Res.* **1980**, *31*, 425–433.

(41) Kantorow, M.; Hawse, J. R.; Cowell, T. L.; Benhamed, S.; Pizarro, G. O.; Reddy, V. N.; Hejtmancik, J. F. Methionine sulfoxide reductase A is important for lens cell viability and resistance to oxidative stress. *Proc. Natl . Acad. Sci . U. S. A.* **2004**, *101*, 9654–9659.

(42) Greenwood, N. N.; Earnshaw, A. *Chemistry of the Elements*; Elsevier, Burlington, MA, U. S. A., 2005.

CHAPTER 4. Confocal X-ray Fluorescence Imaging Facilitates High Resolution Elemental Mapping in Fragile Archaeological Bone

4.1 Preface

The previous chapter demonstrated the benefit of employing CXFI in studying distribution of elements within an intact sample. This chapter illustrates how CXFI can be advantageous in studying poorly preserved archaeological bones which are fragile and hence challenging for creating thin sections, which is a prerequisite for optimum resolution conventional XFI. A comparison with the results from conventional XFI shows that CXFI yields images of higher resolution, which can be insightful in distinguishing biogenic and diagenetic uptake of Pb.

4.2 Manuscript Author Contributions

The contents of this chapter have been accepted for publication as an article in the journal *Archaeometry*: Choudhury S., Swanston T., Varney T., Cooper D. M. L., George G. N., Pickering I. J., Grimes V., Bewer B. and Coulthard I. CXFI facilitates high resolution elemental mapping in fragile archaeological bone. The manuscript ID for the accepted paper is ARCH-06-0078-2015.R1; accepted date: November 10, 2015. The paper has been reformatted from the accepted version for inclusion in the thesis.

The author contributions are provided below.

S. Choudhury collected and analyzed the data, and drafted the manuscript.

T. Swanston provided ICP MS results, prepared bone samples for CXFI and participated in some of the data collection.

T. Varney provided samples and commented on improving the manuscript.

D. M. L. Cooper provided inputs in interpreting data.

V. Grimes provided the R4NL sample.

B. Bewer performed quantitative analysis.

I. Coulthard submitted the manuscript and changes to the journal.

I. Coulthard, G. N. George, and I. J. Pickering supervised this research, providing guidance, scientific input, comments for improving manuscript, and funding.

4.3 Abstract

Synchrotron based standard XFI can be a sophisticated tool for mapping distributions of trace elements in archaeological bone; however, thin samples are normally required to achieve high spatial resolution results. Poorly preserved or fragile archaeological samples can be challenging to measure using this standard technique since producing a sufficiently thin section may be difficult. We discuss the implementation of CXFI as a successful strategy for high resolution elemental mapping in poorly preserved archaeological bone. The implementation of the confocal method additionally can facilitate localized quantification and speciation of elements, which are also discussed.

4.4 Introduction

Study of the trace elements in archaeological bone samples can provide insight into diet, environmental exposure and other determinants of health in the past.[1,2] The uptake of trace elements into bone microstructures through continuous remodeling during life makes bone a dynamic reservoir of trace elements. Since the elemental distribution in bone microstructures carries information about the temporal history of trace element deposition, our ability to extract such information enables us to potentially comment on lifestyle, health and diet of a subject. In particular, secondary osteons, also known as Haversian systems, are important structural units of bone where elemental deposition occurs.[3] The 'secondary' status of these structures is a reference to the fact that they replace existing bone and thus provide a window on changes that occur even after growth of the skeleton is completed. Secondary osteons are roughly cylindrical microstructures oriented along the long axis of bone comprising concentric layers, called lamellae, surrounding a central canal that provides housing for blood vessels and nerves. The deposition of trace elements that occurs during life, referred to as biogenic uptake, is our key interest for extracting information about life history. However, *post-mortem* contamination due

to leaching of trace elements from the burial environment, referred to as diagenesis, constitutes a confounding factor for this area of research. In order for an accurate reconstruction of the lifestyle of a subject, diagenesis needs to be addressed prior to the use of data.[4] High resolution maps of elemental distribution are thus essential to the analysis of the incorporation of elements in bone microstructures.

Experimental techniques commonly applied to study trace elements in archaeological bone samples include: laser ablation inductively coupled plasma mass spectrometry (LA-ICP-MS);[5,6] atomic absorption spectrophotometry (AAS);[7,8] scanning electron microscopy (SEM);[9,10] and synchrotron XFI.[3,11–16]. While useful, techniques such as LA-ICP-MS and AAS are inherently destructive in nature. Depending on the elemental concentration in a sample, AAS may require substantially more sample than is generally available from fragile archaeological samples. Although SEM is considered non-destructive, it is limited to surface characterization and involves extensive sample preparation. Synchrotron based standard XFI is a powerful tool for non-invasive investigation of elemental distribution with minimal sample preparation; fundamentals of the technique can be found elsewhere.[17] While thick samples can in fact be measured, high resolution results showing the incorporation of elements in microstructures are acquired in standard XFI only from very thin samples.[18] The use of a thick sample (e.g. a ground bone section) results in a blurry image due to the superposition of fluorescence originating from features at a range of depths within the sample.[19] Swanston *et al.* reported an application of standard XFI by utilizing archaeological bone sections carefully ground down to ~100 microns thickness.[14] However, preparing a section of micron-scale thickness from an archaeological bone may not always be feasible due to the state of preservation of the sample. Besides, archaeological samples are often valuable, necessitating minimum processing. Therefore, there is an increasing demand for non-invasive techniques for elemental analysis which improve spatial resolution while minimizing both sample quantity and sample preparation.

In this study, we apply the synchrotron based CXFI technique [20,21] to determine the spatial elemental distribution in archaeological bone samples obtained from several different sites, the most prominent being the Royal Naval Hospital cemetery (c. A.D. 1793-1822) near English Harbour, Antigua. Historical sources indicate that this hospital provided care to British

military personnel and the surrounding general populace during the Napoleonic Wars, wherein the British suffered huge losses due to tropical diseases and other illnesses.[22] Lead (Pb) contamination is believed to have contributed to the demise of the British military, since Pb was commonly present in eating and cooking utensils, water catchment systems and alcohol distillation equipment in that era.[22,23] For these reasons we have chosen Pb as a representative element to demonstrate the efficacy of this imaging technique, although other archeologically and biologically important trace elements such as: calcium, zinc, strontium, barium and bromine can also be measured simultaneously following the described methodology. The implementation of CXFI not only avoids physical thin sectioning of the sample but also produces elemental maps showing accumulation of Pb in bone microstructures with excellent detail. A comparison between standard and CXFI results is presented to demonstrate the advantage of the confocal method. The resultant high resolution is due to confocal detection, which facilitates not only optical sectioning of sample but also superior rejection of scatter. Synchrotron based CXFI can be a valuable addition to the toolkits of bioarchaeologists, especially in unravelling elemental distribution within fragile samples.

4.5 Materials and Methods

4.5.1 Samples

Four bone samples were analyzed from 3 distinct sites in 3 different countries. The table below describes the sites by name, location and sample name analyzed using this technique in this study. The most prominent site in terms of available number of samples was the Royal Naval Hospital cemetery (c. A.D. 1793-1822) near English Harbour, Antigua. Samples were recovered during the mitigation of the cemetery due to encroachment by modern construction. Ethics approval was obtained from the University of Saskatchewan Biomedical Research Ethics Board for all samples prior to analysis. Samples were specifically chosen for this study representing several different sites with very different burial environments, soil conditions, and weather in order to demonstrate the efficacy of this technique regardless of variances in these factors. All bones utilized were long bones such as fibula and ulna with outer cortical layers and similar microstructural features.

Table 4-1 Samples analyzed using CXFI arranged by site names and site locations.

Site Name	Site Location	Name of Sample	Approx. Sample Thickness (microns)
Royal Naval Hospital Cemetery	English Harbour, Antigua	B3	140 (non-confocal) 1980 (confocal)
Royal Naval Hospital Cemetery	English Harbour, Antigua	B18	450 (confocal)
Harney Site	Montserrat	H1	1550 (confocal)
South Side Naval Cemetery	Newfoundland, Canada	R4NL	680 (confocal)

4.5.2 ICP-MS

Initial testing of the samples included a bulk analysis of the Pb concentrations using standard methodologies at the ICP-MS Laboratory in the Department of Geological Sciences at the University of Saskatchewan.[14] Quality control standard BCR-2 shows that the long term analytical error for Pb is ± 7%.

4.5.3 Standard XFI

Experiments were carried out at the 20ID-B beamline of the APS at the Argonne National Laboratory (Illinois, USA), with the storage ring operating in continuous top-up mode at 102 mA and 7.0 GeV. The incoming beam was tuned to the desired excitation energy of 16.5 keV (with an estimated intensity of ~10^{12} photons/sec) by using a liquid-nitrogen-cooled Si (111) double crystal monochromator with a second crystal detuned by 15% to reduce harmonic contamination. A micro-beam of approximately 5 µm × 5 µm spot-size was produced using Rh-coated silicon based K-B-style focusing mirrors, which also served to provide additional harmonic rejection. Samples were mounted on a motorized stage at 45º to the incident beam. The Pb Lα fluorescent emission lines at 10.55 and 10.44 keV and other fluorescence X-rays were monitored using a Si-drift Vortex® detector (SII NanoTechnology USA Inc.) placed at 90º with respect to the incident X-ray beam in the horizontal plane. An ionization chamber monitored the intensity of the incident X-ray beam, I_0, which was used for the normalization of the fluorescence; this process eliminates the impact of any possible flux variations of the source.

4.5.4 CXFI

CXFI experiments were also carried out at the 20ID-B beamline with the following modifications. To create the confocal geometry, an additional focusing optic, a polycapillary (XOS®) of nominal 25 μm diameter focal spot (at Mo Kα; 17.4 keV), was installed in front of the Si-drift Vortex® detector. Figure 4.1 shows a schematic diagram and a photograph of the CXFI experiment at 20ID-B, APS. The arrangement for a standard XFI experiment differed only in the absence of the polycapillary, which is not required for the standard technique. The sample was positioned at an orientation of 45º to both the incident X-ray beam and detector, with the detector at 90º to the incident beam in order to minimize the inelastic scattering of linearly polarized synchrotron radiation, as the scattering cross-section along the **e**-vector is zero.[24] Figure 4.1 shows: 1) K-B mirror: a focusing optic on the incident beam to produce micro-focused beam; 2) ionization chamber I_0: a unit that measures incident beam intensity; 3) sample stage: a platform that holds the sample and allows its XYZ translation; 4) detector: an energy dispersive fluorescence detector that measures fluorescence emitted from sample; and 5) polycapillary: a second focusing optic on the detection side for confocal detection. Figure 4.1a schematically shows the formation of confocal volume (V_c), within the sample.

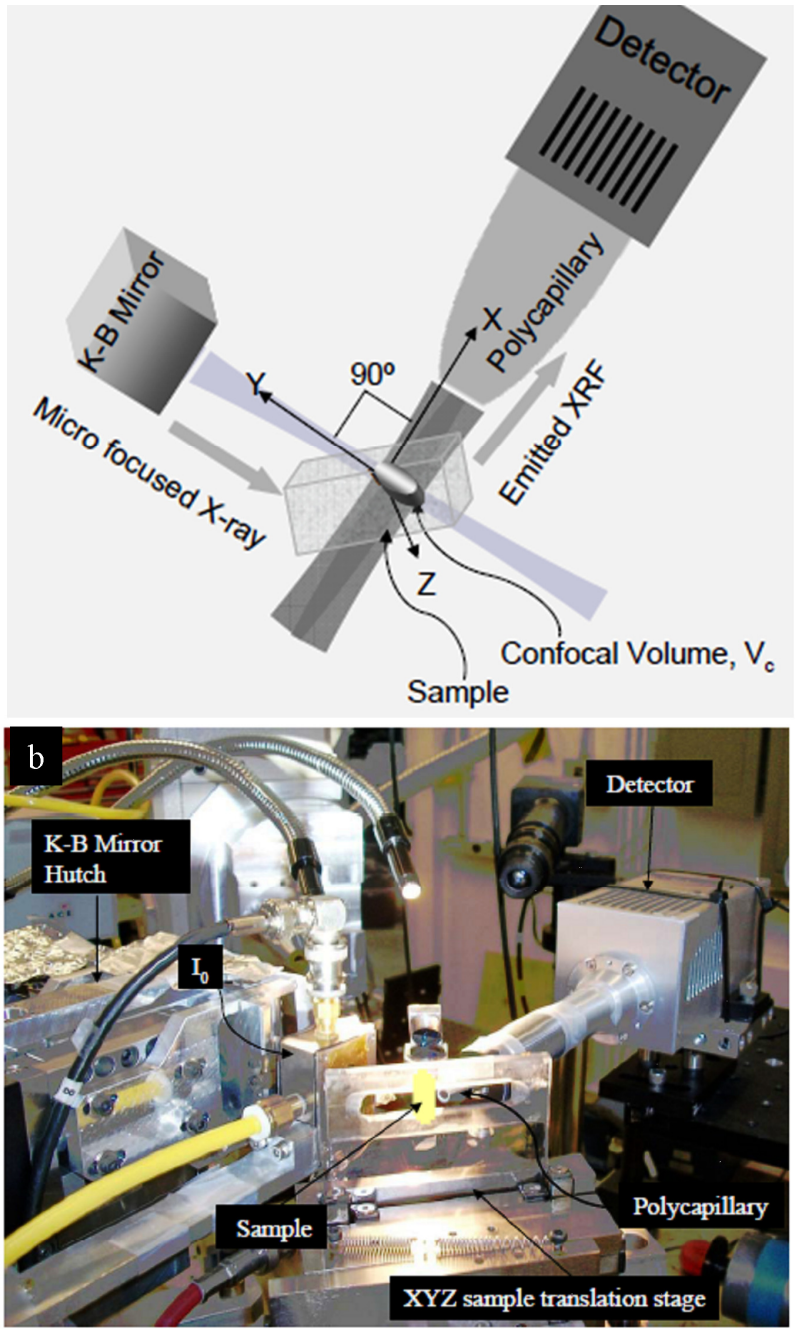

Figure 4.1 The CXFI arrangement at beamline 20ID-B, APS, shown as (a) a schematic diagram and (b) a photograph. The sample is at 45º to the incident beam and detector. The schematic diagram shows the formation of the confocal volume (Vc) within the sample through the intersection of foci of incident and detection focusing optics, K-B mirror and polycapillary, respectively. The sample can be rastered along XYZ directions through V_c to produce elemental maps along desired planes.

4.5.5 Data analysis

Data from both experimental configurations were analyzed using the SMAK software package (http://home.comcast.net/~sam_webb/smak.html). The recorded fluorescence counts were normalized to the incident intensity I_0 (Figure 4.1) and were background corrected by subtracting the average intensity of pixels outside the image from the intensity of each pixel of the image.

Quantification was performed by first normalizing the sample measurement to the known reference material with respect to incident photon flux, dwell time, and detector sensitivity. Sample fluorescence signal loss from absorption due to confocal depth within the sample was corrected for by using the known surface calcium count rate compared to the count rate measured at each point to determine the local depth for each pixel. The measured Pb count rate for the reference material could then be compared to the measured Pb count rate for the sample and using the known concentration of the reference the sample concentration was determined.[25]

4.6 Results and Discussion

A small portion of certain samples was sacrificed for the ICP-MS measurement, which determined the bulk levels of Pb in samples B3 and B18 to be 75 and 58 ppm, respectively. The amount of material sacrificed was approximately 0.05-0.1 g by weight and was always taken from a section of bone immediately adjacent to the section of bone analyzed with XRF. While the presence of Pb in bone may indicate that subject was exposed to Pb while living, diagenesis could also be the source of Pb. Quantification of the Pb levels using the CXFI image for sample B18 yielded whole bone Pb concentration levels consistent with the ICP-MS level though typically 10-25 % lower.[25] Of greater interest is the ability to glean localized Pb concentration methods from this method. The quantification method yielded localized maxima of Pb concentrations of several hundreds of ppm at the canal walls of some osteons with the highest observed localized concentration being ~600 ppm.

In a standard XFI experiment, which lacks a focusing optic on the detector, fluorescence emitted from the range of sample depths interrogated by the incident beam is collected directly

by the detector. Mapping is accomplished by rastering the area of interest through the incident micro-beam with simultaneous measurement of fluorescence. Since the fluorescence lines of elements are at well-defined energies, this technique offers excellent element specificity. However, although standard XFI is a widely used technique for elemental mapping, it is not designed to discriminate information originating from different depths within the sample. Fluorescence emitted from microstructures at a range of depths are detected and superposed on a two dimensional map resulting in a blurry image. In order to minimize this problem, the thickness of sample used for the standard XFI measurement can be reduced by physical sectioning. However, preparation of thin sections is frequently not possible; for example, sample B18 in this study was deemed to be too fragile to be sectioned. We therefore have employed CXFI to accomplish elemental mapping in sample B18.

Figure 4.2 represents Pb elemental maps obtained from sample B3 by employing standard (Fig. 4.2a) and CXFI (Fig. 4.2b), respectively. Two separate pieces of sample B3 were utilized, one thinned to 140 microns of thickness and the other left intact with a thickness of 1980 microns. A ~2 mm × 2 mm area of interest from each piece of sample B3 was mapped with a 20 µm step-size where each map took approximately 2.5 hrs. The comparison between standard- and confocal-derived maps in this figure demonstrates that CXFI (Fig. 4.2b) yields an elemental map with significantly improved spatial resolution compared with standard XFI (Fig. 4.2a), showing excellent details of the incorporation of Pb in various bone microstructures. Structural detail observed in the confocal map (Fig. 4.2b) includes younger osteons, older osteons, cement lines and osteonal canals. A younger osteon can be identified as a continuous closed-ring structure with a central canal, whereas an older osteon appears as a discrete broken-ring structure with or without a central canal formed during regular bone tissue maintenance or turnover. The osteonal canals are easily identified as holes at the center of the osteons. Cement lines are observed as the boundary lines of osteons, with some broken cement lines observed as the remnants of old osteons

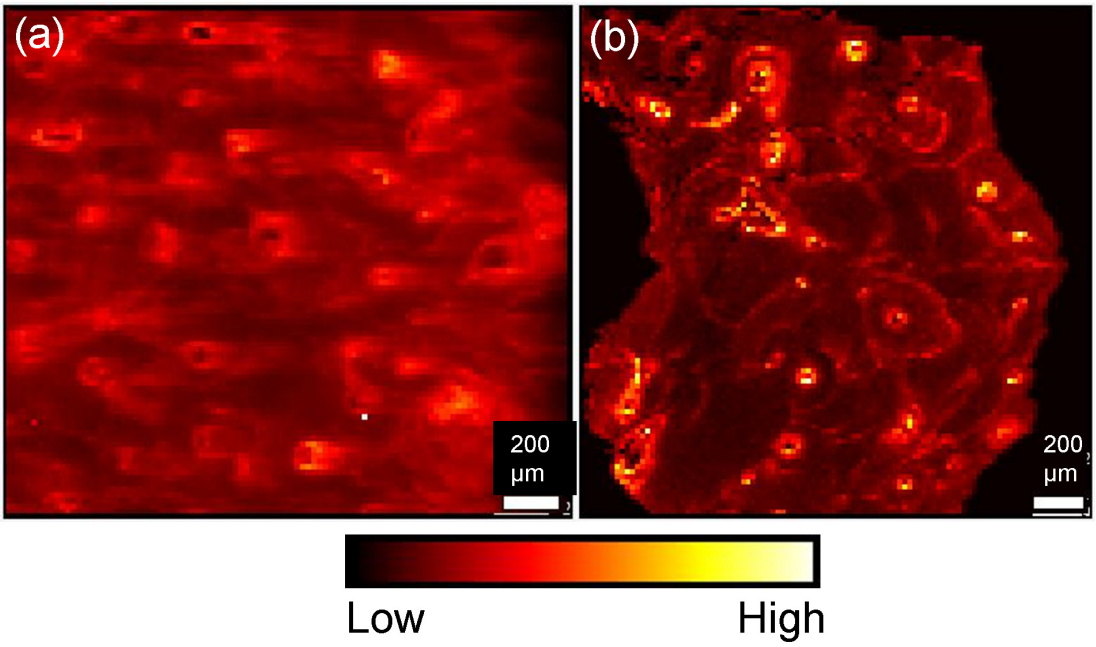

Figure 4.2 X-ray fluorescence maps showing Pb distribution in bone micro-structures: 2 mm × 2 mm areas of (a) sample B3 measured using standard mode and (b) sample B3 measured using confocal mode. Comparison between 2a and 2b demonstrates the advantage of CXFI in generating high resolution elemental maps from fragile archaeological bone. The intensity scale shows the relative amounts of Pb from black (lowest Pb) through shades of red, orange and yellow to white (highest Pb).

Figure 4.2a-b shows clear accumulation of Pb in bone microstructures but no accumulation in the periosteal surface (the right sample surface in Fig. 4.2b) which are the outer surfaces of the bone fragment that were most directly exposed to the burial environment. Pb is observed in most canal walls and cement lines, while few osteons show Pb enrichment throughout the entire structure. Although most canals show clear Pb accumulation, a few show little or no accumulation at all. These results are consistent with previous results on archaeological bone where such patterns of Pb were attributed to be indicative of biogenic uptake.[14] They are also strikingly similar to results where the samples were modern bone from cadavers which had not been exposed to a burial environment and the subsequent diagenetic factors.[15]

In comparison, Fig. 4.2a shows a standard XFI map obtained from sample B3. Clearly, the spatial resolution in this map is considerably degraded compared to the confocal one. The three dimensional structure of osteons, comprising cylindrical structures of varying diameter and three dimensional angular orientation arranged throughout the depth of sample, explains the blurred appearance of the map. If an irregular three dimensional structure is viewed by a standard imaging technique, the resulting image is a juxtaposition of fluorescence from different features situated at different depths within the sample. While some three dimensional information, such as the angular orientation of the cylindrical structures in the sample, might be extractable from such an image, the ability to resolve individual features is significantly reduced. This map (Fig. 4.2a) thus demonstrates the challenge of employing standard XFI in investigating an irregular three dimensional feature within a thicker sample, which is significantly improved using confocal detection in Fig. 4.2b.

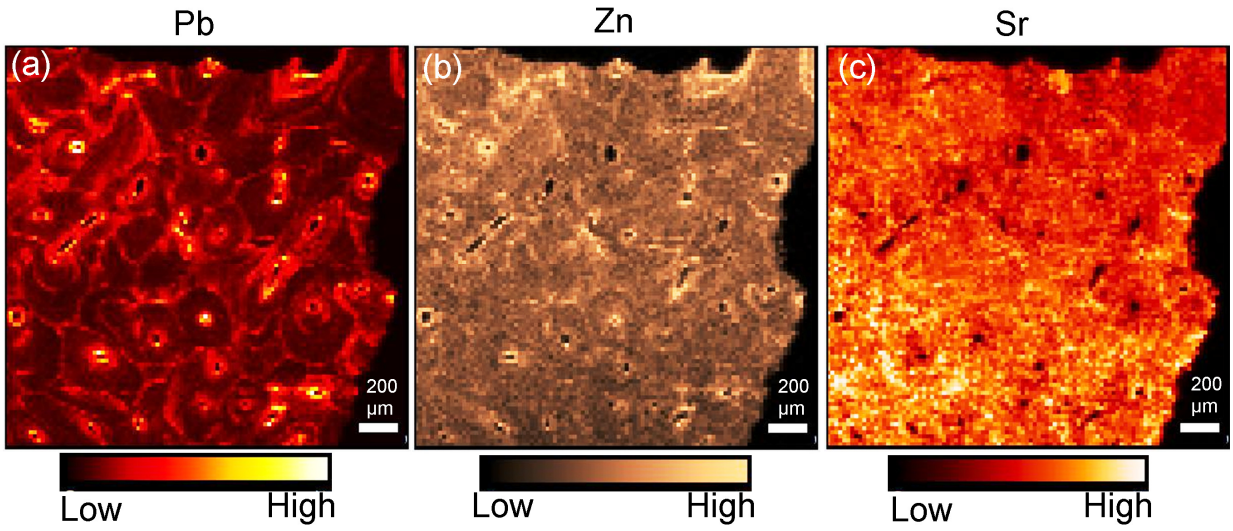

Figure 4.3 X-ray fluorescence maps showing distribution of Pb (a), Zn (b), and Sr (c) in bone micro-structures of sample B18. Scan size is 2 mm × 2 mm. In all images, the intensity scale shows the relative amounts of the elements with darkest coloration being the lowest amounts and lightest coloration being higher with white being the highest.

Figure 4.3 shows confocal images of sample B18 for multiple elements taken simultaneously demonstrating that while the emphasis in this paper has been on showing Pb accumulation images, the power of the energy dispersive type detector used means that the fluorescence signal from all elements within the sample are analyzed at the same time. This makes this data available for all elements and all samples and also assures that all maps of all elements overlap each other without offset. The position of the confocal focusing optic relative to the sample and the detector also assures that all images for all elements are confocal images. Figure 4.4 shows Pb CXFI images for a pair of samples (H1 and R4NL) from different locations (Table 4.1) other than the Naval Hospital Site in Antigua, demonstrating that the technique works perfectly well for samples taken from a diverse variety of locations and burial conditions and is not only applicable to a narrow set of samples collected or found under ideal or extremely specific conditions.

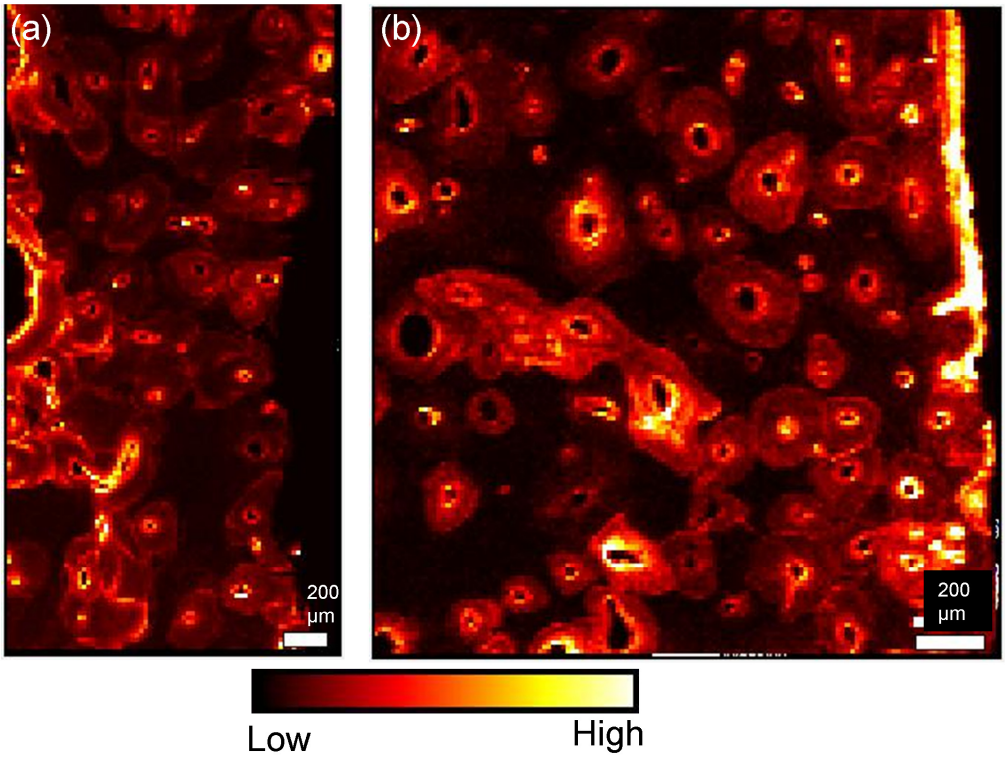

Figure 4.4 X-ray fluorescence maps showing distribution of Pb in the bone microstructures of samples R4NL (a) and H1 (b). Scan sizes are ~2 mm × 2 mm but were slightly modified to account for sample shape. In both images, the intensity scale shows the relative amounts of Pb with darkest coloration being the lowest amounts and lightest coloration being higher with white being the highest.

In CXFI experiments, excitation and detection coincide only at the intersecting volume, commonly known as the confocal volume, defined by the foci of the incident (K-B mirror) and detection (polycapillary) focusing optics. Since the focal spot of the polycapillary (25 μm diameter at the Mo Kα energy) is much bigger than the beam spot size (5 μm × 5 μm), the resulting detection volume would be ellipsoidal [26] with an approximate dimension of 40 μm × 5 μm × 5 μm [26] at the energy of Pb L*α*. Elemental maps can be obtained by spatially rastering the sample through the confocal volume along any desired plane within the sample. This technique, therefore, removes the need for physical sectioning of sample through its inherent ability of optical sectioning. Implementation of the confocal technique also greatly helps to improve signal to noise ratio in the resulting maps due to the collimating nature of polycapillary, since fluorescent and scattered photons are collected essentially only from the volume of interest.[27] In comparison, a standard XFI experiment will show a much larger scatter peak as the detector collects fluorescence from a much longer intersection path of the beam through the sample (limited by the absorption length). Besides, as the detection solid angle in a standard XFI experiment is much larger compared to the confocal, scatter originated from other sources such as mounts, windows, air or other gas and other beamline equipment may also be detected. A superior signal to noise ratio is particularly important for the detection of low concentration elements in the sample. Further this optical form of sectioning clearly gives better results in terms of co-localizing the elements to the microstructural features of the bone.

The variation in Pb accumulation in bone microstructures may carry significant information regarding health, lifestyle or diagenesis. However, a detailed observation of the incorporation of Pb throughout the various components of bone microstructures is necessary in order to be able to comment on what might be the underlying reason for such variations. We emphasize here the potential of CXFI in producing high resolution maps which will make such observation possible. Additionally, a high resolution confocal map may exclude the need for a matching histological image, which was necessary for the interpretation of a standard XFI map in a previous study.[14]

Another important advantage of employing CXFI is its ability to make XAS possible for an element of interest within a very specific detection volume from within the sample, allowing

assessment of the localized chemical form of elements.[26] CXAS may thus aid in differentiating between the biogenic and diagenetic nature of elements in archaeological samples by looking for differences in speciation of elements at specific structural features of the bone such as: osteon canal wall, cement line, and periosteal surface. Moreover, localized quantitative information about the elements is available from CXFI maps given that self-absorption of incident and fluorescent X-rays can be estimated.[28] Quantitative elemental analysis may aid in the differentiation of acute or chronic exposure to toxic elements. Further improvements in the spatial resolution of CXFI can be achieved by implementing a novel detection focusing optic, a micro-channel array.[29] We intend to explore this potential in future studies.

4.7 Conclusions

This paper demonstrates the potential of synchrotron based CXFI as a tool to generate high spatial resolution elemental maps from fragile archaeological bone samples showing excellent details of elemental incorporation into bone microstructures. Fragile or poorly preserved archaeological samples cannot be processed to create sufficiently thin sections for elemental mapping using standard XFI experiments. CXFI, which inherently produces optical sections, avoids the need for physical sectioning. Besides enabling optical sectioning, the confocal mode also aids in generating maps of a higher signal-to-noise ratio by considerably reducing the background scatter. This technique should help elucidate the origins of observed elements in the bone samples, and whether they are biogenic, diagenetic, or a combination of both.

4.8 Acknowledgements

This research was supported by a Social Sciences and Humanities Research Council (SSHRC) Insight Development Grant (#430-2012-0236), by NSERC Discovery Grants (to GNG and IJP), and by the Canada Foundation for Innovation through funding for BioXAS: Life Science Beamline for X-ray Absorption Spectroscopy at the Canadian Light Source Inc.. SC is a fellow in the Canadian Institutes of Health Research Training grant in Health Research Using Synchrotron Techniques (CIHR-THRUST, IJP and others). GNG, IJP and DMLC are Canada Research Chairs. This work was also supported by the Canada Foundation for Innovation

through funding for BioXAS: Life Science Beamline for X-ray Absorption Spectroscopy at the Canadian Light Source Inc. Sector 20 facilities at the Advanced Photon Source, and research at these facilities, are supported by the US Department of Energy - Basic Energy Sciences, the Canadian Light Source and its funding partners, and the Advanced Photon Source. Use of the Advanced Photon Source, an Office of Science User Facility operated for the U.S. Department of Energy (DOE) Office of Science by Argonne National Laboratory, was supported by the U.S. DOE under Contract No. DE-AC02-06CH11357.

4.9 References

(1) Rasmussen, K. L.; Skytte, L.; Pilekær, C.; Lauritsen, A.; Boldsen, J. L.; Leth, P. M.; Thomsen, P. O. The distribution of mercury and other trace elements in the bones of two human individuals from medieval Denmark - the chemical life history hypothesis. *Herit. Sci.* **2013**, *1*, 10.

(2) Lanzirotti, A.; Bianucci, R.; LeGeros, R.; Bromage, T. G.; Giuffra, V.; Ferroglio, E.; Fornaciari, G.; Appenzeller, O. Assessing heavy metal exposure in Renaissance Europe using synchrotron microbeam techniques. *J. Archaeol. Sci.* **2014**, *52*, 204–217.

(3) Martin, R. R.; Naftel, S. J.; Nelson, A. J.; Sapp III, W. D. S. Comparison of the distributions of bromine , lead , and zinc in tooth and bone from an ancient Peruvian burial site by X-ray fluorescence. *Can. J. Chem.* **2007**, *85*, 831–836.

(4) Zapata, J.; Pérez-Sirvent, C.; Martínez-Sánchez, M. J.; Tovar, P. Diagenesis, not biogenesis: Two late Roman skeletal examples. *Sci. Total Environ.* **2006**, *369*, 357–368.

(5) Koenig, A. E.; Rogers, R. R.; Trueman, C. N. Visualizing fossilization using laser ablation-inductively coupled plasma-mass spectrometry maps of trace elements in Late Cretaceous bones. *Geology* **2009**, *37*, 511–514.

(6) Kohn, M. J.; Moses, R. J. Trace element diffusivities in bone rule out simple diffusive uptake during fossilization but explain in vivo uptake and release. *Proc. Natl. Acad. Sci. U.S.A.* **2013**, *110*, 419–424.

(7) Arnay-de-la-Rosa, M.; Gonzalez-Reimers, E.; Velasco-Vazquez, J.; Barros-Lopez, N.; Galindo-Martin, L. Bone trace element pattern in an 18th century population sample of Tenerife (Canary Islands): comparison with a prehistoric one. *Biol. Trace Elem. Res.* **1998**, *65*, 45–51.

(8) Arnay-de-la-Rosa, M.; González-Reimers, E.; Yanes, Y.; Romanek, C. S.; Noakes, J. E.; Galindo-Martín, L. Paleonutritional and paleodietary survey on prehistoric humans from

Las Cañadas del Teide (Tenerife, Canary Islands) based on chemical and histological analysis of bone. *J. Archaeol. Sci.* **2011**, *38*, 884–895.

(9) Freestone, I. C.; Middleton, A. P.; Museum, B. Mineralogical applications of the analytical SEM in archaeology. *Miner. Mag.* **1987**, *51*, 21–31.

(10) Bell, L. S. Palaeopathology and diagenesis: an SEM evaluation of structural changes using backscattered electron imaging. *J. Archaeol. Sci.* **1990**, *17*, 85–102.

(11) Kanngießer, B.; Malzer, W.; Reiche, I. A new 3D micro X-ray fluorescence analysis set-up – First archaeometric applications. *Nucl. Instrum. Meth. B* **2003**, *211*, 259–264.

(12) Grolimund, D.; Senn, M.; Trottmann, M.; Janousch, M.; Bonhoure, I.; Scheidegger, A. M.; Marcus, M. Shedding new light on historical metal samples using micro-focused synchrotron X-ray fluorescence and spectroscopy. *Spectrochim. Acta B* **2004**, *59*, 1627–1635.

(13) Bertrand, L.; Robinet, L.; Thoury, M.; Janssens, K.; Cohen, S. X.; Schöder, S. Cultural heritage and archaeology materials studied by synchrotron spectroscopy and imaging. *Appl. Phys. A* **2011**, *106*, 377–396.

(14) Swanston, T.; Varney, T.; Coulthard, I.; Feng, R.; Bewer, B.; Murphy, R.; Hennig, C.; Cooper, D. Element localization in archaeological bone using synchrotron radiation X-ray fluorescence: identification of biogenic uptake. *J. Archaeol. Sci.* **2012**, *39*, 2409–2413.

(15) Pemmer, B.; Roschger, A.; Wastl, A.; Hofstaetter, J. G.; Wobrauschek, P.; Simon, R.; Thaler, H. W.; Roschger, P.; Klaushofer, K.; Streli, C. Spatial distribution of the trace elements zinc, strontium and lead in human bone tissue. *Bone* **2013**, *57*, 184–193.

(16) Martin, R. R.; Naftel, S.; Macfie, S.; Jones, K.; Nelson, A. Pb distribution in bones from the Franklin expedition: synchrotron X-ray fluorescence and laser ablation/mass spectroscopy. *Appl. Phys. A-Mater.* **2013**, *111*, 23–29.

(17) Pushie, M. J.; Pickering, I. J.; Korbas, M.; Hackett, M. J.; George, G. N. Elemental and chemically specific X-ray fluorescence imaging of biological systems. *Chem. Rev.* **2014**, *114*, 8499–8541.

(18) Vekemans, B.; Vincze, L.; Brenker, F. E.; Adams, F. Processing of three-dimensional microscopic X-ray fluorescence data. *J. Anal. At. Spectrom.* **2004**, *19*, 1302–1308.

(19) Wittmers, L. E.; Aufderheide, A. C.; Pounds, J. G.; Jones, K. W.; Angel, J. L. Problems in determination of skeletal lead burden in archaeological samples: an example from the First African Baptist Church population. *Am. J. Phys. Anthrolpol.* **2008**, *136*, 379–386.

(20) Woll, A. R.; Mass, J.; Bisulca, C.; Huang, R.; Bilderback, D. H.; Gruner, S.; Gao, N. Development of confocal X-ray fluorescence (XRF) microscopy at the Cornell high energy synchrotron source. *Appl. Phys. A* **2006**, *83*, 235–238.

(21) Janssens, K.; Proost, K.; Falkenberg, G. Confocal microscopic X-ray fluorescence at the HASYLAB microfocus beamline: characteristics and possibilities. *Spectrochim. Acta B* **2004**, *59*, 1637–1645.

(22) Varney, T. L.; Nicholson, D. V. Caribbean Archaeology,. *Proc. XVIII Int. Congr. Caribb. Archaeol. Grenada, WI* **1999**, 329–335.

(23) Varney, T. L.; Swanston, T.; Cooper, D. M. L.; Graham, N.; Pickering, I. J.; Reginald, A. A preliminary investigation of lead poisoning in a Napoleonic era Naval Cemetery in Antigua , W . I . *Caribb. Connect. A Publ. F. Res. Cent. 2(1) Spec. Issue Focus. Bioarchaeology Caribbean.* **2012**, *II* (1).

(24) Haller, M.; Knochel, A. X-ray fluorescence analysis using synchrotron radiation (SYXRF). *J. Trace Microprobe Tech.* **1996**, *14*, 461–488.

(25) Bewer, B. Quantification estimate methods for synchrotron radiation X-ray fluorescence spectroscopy. *Nucl. Instrum. Meth. B* **2015**, *347*, 1–6.

(26) Silversmit, G.; Vekemans, B.; Nikitenko, S.; Schmitz, S.; Schoonjans, T.; Brenker, F. E.; Vincze, L. Spatially resolved 3D micro-XANES by a confocal detection scheme. *Phys. Chem. Chem. Phys.* **2010**, *12*, 5653–5659.

(27) Wilke, M.; Appel, K.; Vincze, L.; Schmidt, C.; Borchert, M.; Pascarelli, S. A confocal set-up for micro-XRF and XAFS experiments using diamond-anvil cells. *J. Synchrotron Radiat.* **2010**, *17*, 669–675.

(28) Samber De, B.; Silversmit, G.; Schamphelaere De, K.; Evens, R.; Schoonjans, T.; Vekemans, B.; Janssen, C.; Masschaele, B.; Hoorebeke Van, L.; Szalóki, I.; Vanhaecke, F.; Rickers, K.; Falkenberg, G.; Vincze, L. Element-to-tissue correlation in biological samples determined by three-dimensional X-ray imaging methods. *J. Anal. At. Spectrom.* **2010**, *25*, 544–553.

(29) Woll, A. R.; Agyeman-Budu, D.; Choudhury, S.; Coulthard, I.; Finnefrock, A. C.; Gordon, R.; Hallin, E.; Mass, J. Lithographically-fabricated channel arrays for confocal X-ray fluorescence microscopy and XAFS. *J. Phys. Conf. Ser.* **2014**, *493*, 012028 (1–4).

CHAPTER 5. Application of a Spoked Channel Array to Confocal X-ray Fluorescence Imaging and X-ray Absorption Spectroscopy of Medieval Stained Glass

5.1 Preface

This chapter demonstrates the first confocal X-ray fluorescence experimental setup at 20ID-B, APS that employed a novel focusing optic, the SCA, for achieving a higher spatial resolution compared to the traditionally used state-of-the-art polycapillary optics. The first experiment with this setup studied the oxidation state of Fe in the corrosion layer of a medieval stained glass sample using CXFI and CXAS. The choice of an inorganic sample was deliberate due to the high elemental concentrations. The results demonstrate the advantages of employing SCA derived improved spatial resolution and energy-independent probe volume in studying elemental distribution and speciation from precious ancient samples in a highly nondestructive manner.

5.2 Manuscript Author Contributions

This chapter was published in the *Journal of Analytical Atomic Spectrometry*: Choudhury, S.; Hormes, J.; Agyeman-Budu, D. N.; Woll, A. R.; George, G. N.; Coulthard, I.; Pickering, I. J. Application of a spoked channel array to confocal X-ray fluorescence imaging and X-ray absorption spectroscopy of medieval stained glass. *Journal of Analytical Atomic Spectrometry* 2015, *30*, 759–766. DOI: 10.1039/C4JA00389F. The chapter is reproduced by permission of The Royal Society of Chemistry (RSC) on behalf of the Centre National de la Recherche Scientifique (CNRS) and the RSC. The paper has been reformatted from the accepted version for inclusion in the thesis. The author contributions to the manuscript are provided below.

S. Choudhury collected and analyzed the data, and drafted the manuscript.

J. Hormes provided the sample, and insights on the interpretation of data.

D. N. Agyeman-Budu and A. R. Woll designed and fabricated the SCA optics.

I. J. Pickering and G. N. George performed the deconvolution of pre-edge spectra shown in Figure 5.4(B).

I. J. Pickering submitted the manuscript and changes to the journal.

I. Coulthard, G. N. George, and I. J. Pickering have supervised this research, providing guidance, scientific input, comments for improving manuscript, and funding.

5.3 Abstract

CXFI can determine the spatial distribution of elements in a depth selective manner. The closely related technique of CXAS can reveal the chemical form of an element at a specific volume element in three dimensional space. Confocal measurement offers increased accuracy and avoids physical sectioning or ablative depth profiling methods, thus preserving sample integrity. At present, a polycapillary mounted on the detector is the common optical element used to complete the confocal configuration. Here we demonstrate implementation of a novel collection optic, a lithographically fabricated SCA optic, to achieve the confocal configuration at beamline 20-ID, APS. The advantages of employing SCA optics include improved spatial resolution and energy independent probing volume. By employing this optic, three dimensional distributions of Fe, Ca and Mn and the localized chemical form of Fe were measured in the intact corrosion layer of an ancient stained glass sample obtained from 13th Century Paderborn Cathedral, Germany. Implementation of the optic enabled superior resolution depth selectivity in the intact corrosion layer and measurement of elemental distribution and speciation in a highly localized manner within the layer with improved signal to noise. The results show that both the composition and the chemical form vary as a function of three dimensional location in the corrosion layer. This observation is contrary to expectations from simple corrosion models assuming leaching processes and indicates that metal chemistry in these layers is quite complex.

5.4 Introduction

The implementation of synchrotron based techniques to investigate artefacts of historical interest is an area of significant growth. Bright and tunable synchrotron X-rays enable greatly improved sensitivity in trace elemental detection together with techniques not possible using

conventional X-ray sources. XFI is a non-destructive tool for studying two dimensional trace element distribution.[1] CXFI,[2,3] a more recent variant, enables depth selective investigation of the spatial distribution of elements from a thick or intact sample with improved spatial resolution, and is particularly useful for fragile or valuable objects for which sectioning is challenging or undesirable. Although confocal micro-analysis is a relatively new technique, its application in investigating cultural heritage samples is of increasing interest due to the non-destructive nature and depth-profiling capability of this method. Some examples of such studies include: paint layers in ancient Indian Mughal miniatures,[4] depth profiling of historic paintings,[3] Chinese faux bamboo paint,[5] corrosion layers of reverse glass paintings,[6] Japanese lacquerware *Tamamushi-nuri*,[7] Portuguese polychrome glazed ceramics,[8] and Persian polychrome underglaze painted tiles.[9]

Confocal detection requires the use of an additional focusing optic placed in front of the detector in conjunction with the focusing optic at the incident side. The spatial resolution of a CXFI experiment is defined by the size of the probing volume, which depends on the focal spot sizes of the incident and collection focusing optics.[3] Although a number of optics are in use for focusing the incident synchrotron X-ray beam, a polycapillary has been the predominant choice of optic for the collection of fluorescent X-rays. A novel collection optic, a lithographically fabricated SCA, recently has been reported as a practical alternative for confocal micro X-ray analysis.[10] The basic principles and fabrication methods for SCAs have been described previously.[11] Employing this optic for CXFI enables a much smaller probing volume, allowing investigation of highly localized features as small as ~2 μm, whereas the best-reported spatial resolution achieved from a polycapillary is ~10 μm at 10 keV.[3,12,13] Additionally, the SCA optic renders the probing volume nearly independent of energy, resulting in a constant spatial resolution for different elements.[10] In contrast, a polycapillary derived probing volume is always energy dependent due to the energy dependency of the critical angle of total external reflection. This dependence is especially problematic for fluorescence energies below about 5 keV, for which the best reported resolution is greater than 20 μm.[3,12,13]

XFI can be used in conjunction with XAS, which is a non-destructive tool for determination of the chemical form of an element. One of the strengths of the confocal detection

scheme is that it enables XAS determination of the chemical form in a highly localized volume element within a thick or intact sample, which is particularly useful if heterogeneity in chemical form is expected on a scale of a few microns. Polycapillary based CXAS has been used previously for depth resolved chemical speciation of elements in geological and cultural heritage samples, such as Fe K XAS studies of mineral inclusions within rare natural diamonds,[14] Np L_3 XAS to determine the valence state of Np within granite,[15] and Cu K XAS in investigating the chemical state of coloring agents in blue and blue-green zones of Persian polychrome underglaze painted tiles.[9] The current paper comprises the first demonstration of SCA based CXAS; implementation of SCA allows superior spatial localization coupled with an energy independent probing volume. Although not demonstrated in this paper, the energy independency of probing volume will allow more straightforward correlation of chemical forms determined using more than one absorption edge.

In this paper, we demonstrate SCA based CXFI and CXAS in investigating the distribution and speciation of elements in a medieval stained glass sample obtained from the 13th century cathedral in Paderborn, Germany. This sample, in addition to three others from the same cathedral, was previously studied to determine the concentrations of elements using both LA-ICPMS and synchrotron based XFI, as well as the chemical form of elements using XAS.[16] Elemental concentration results obtained from two techniques showed significant variation,[16] which was thought to be due to the presence of concentration gradients originating from corrosion or leaching layers combined with the differing surface sensitivities of the two techniques. The investigation of chemical forms of elements[16] employed conventional (non-confocal) XAS and highlighted the potential of the technique for revealing information on how various elements play roles in glass degradation. The XAS results[16] showed that although most elements in glass are found in their most stable oxidic forms, Ti and Pb show exceptions. Stained glass windows were one of the major pictorial art forms in medieval European culture with many examples still existing in their original form, for instance in churches, cathedrals and other public places. In order to optimize the cleaning, restoration and conservation procedures for these precious historical art forms and to better understand the techniques that were used in their fabrication process, it is important to explore in-depth elemental investigations as such study facilitates our understanding of the manufacturing and underlying degradation mechanisms.

The corrosion of historical glasses is a complex process determined and controlled by numerous factors such as chemical composition and characteristics of the glass, climatic conditions and atmospheric pollution.[17,18] The basic "corrosion mechanism" described in the literature is a two-step process in which an initial step is an ion exchange process between hydrogen-bearing species from the water film on a glass and (mainly) network-modifying ions, such as alkali and earth-alkali atoms. After the evaporation of the water film these products form a solid weathering crust. In a subsequent step, the silica network is broken up by hydroxyl ions forming Si-OH groups and thus dissolving the glass.[19] To better understand the details of the mechanism of the corrosion process, depth profiling of all elements involved in this process is of interest. We demonstrate that SCA derived higher spatial resolution is useful in studying the three dimensional distribution of elements in the corrosion layer as well as their localized chemical states. Our imaging results show significant variations, within the ~100 μm outer thickness of the corrosion layer, in the concentration of iron (Fe), manganese (Mn) and calcium (Ca) which are the predominant non low-Z elements observed in the sample. In addition, spatially resolved XAS shows variation in the chemical form of Fe in the corrosion layer as a function of depth and position. This variation indicates a more complex chemistry of elements in the corrosion layer than previously described in the literature.[17,19] This paper demonstrates that the capability of a confocal approach in studying cultural heritage samples can be further enhanced by implementing lithographically fabricated SCA optics.

5.5 Materials and Methods

The stained glass sample labelled as 'Paderborn 11' studied in this paper was recovered from an archaeological excavation at the Paderborn Cathedral, Germany carried out between 1978 and 1980.[20] The sample looked light green in colour under the corrosion layer. A picture of the sample is available elsewhere.[16]

CXFI and CXAS experiments were carried out at the 20ID-B beamline of the APS at the Argonne National Laboratory, with the storage ring operating in continuous top-up mode at 102 mA and 7.0 GeV. The incoming beam was tuned to an incident energy of 10 keV (estimated intensity of ~10^{12} photons/sec) by using a liquid-nitrogen-cooled Si (111) double crystal monochromator with a second crystal detuned by 15% to reduce harmonic contamination. A

micro-beam of approximately 5 × 5 μm^2 spot-size was produced using Rh-coated silicon based K-B style focusing mirrors, which also served for additional harmonic rejection. The fluorescent emission lines were monitored using an energy-dispersive single element Si-drift Vortex® detector (SII NanoTechnology USA Inc.) placed at 90º with respect to the incident X-ray beam in the horizontal plane. To arrange the confocal geometry, a trapezoidal-shaped SCA optic, described in the next paragraph, was mounted immediately in front of the detector snout. The sample was mounted on a motorized stage at 30º to the incident beam, an angle chosen to maximize space for sample translation. An I_0 ionization chamber, mounted downstream of the K-B mirrors to monitor the incident monochromatized X-ray beam intensity, was used to normalize the fluorescence; this process eliminates the impact of any possible flux variations of the X-ray source on the various fluorescence spectra. A variable magnification camera focused on the sample surface was employed during set-up to view the position of beam and SCA optic relative to the sample surface, the relative positions of which were critical given the very small working distance.

The SCA optic, etched from a silicon wafer, is comprised of 96 channels each approximately 7 μm × ~200 μm × 4 mm (width × depth × length) in size,[10] and fabricated using standard lithographic techniques, including DRIE. The optic has a working distance of 1.0 mm, with channels separated by 9 mrad. Previous tests of this optic[10] demonstrated that the angular selectivity of the channels is 3.3 mrad, somewhat larger than their geometric selectivity of 1.75 mrad, and a total, effective solid angle of collection of as much as 0.14% of 4π at 9 keV. Care was taken to block virtually all other radiation (from outside the probing volume) from reaching the detector, which is generally more challenging for SCAs than for polycapillaries. The working distance for the SCA optic used in these measurements was only a few hundred microns, although in newer versions this has been increased to about a millimeter.

Figure 5.1 shows a schematic of the confocal XFI/XAS experimental arrangement with the SCA collection optic. An initial alignment procedure allowed the intersection of focal spots of incident (K-B mirror) and collection (SCA) focusing optics in order to form the probing volume. The sample was mounted on a high precision motorized XYZ translation stage, which allowed the translation of the sample through the probing volume in three directions. The

energy-independent dimension of the ellipsoidal probing volume for this configuration was ~ 5 × 7 × 4 μm^3 ($D_B \times D_A \times D_V$). Here D_B is one of the minor axes of the ellipsoid defined by the FWHM of the incident beam, D_A is the major axis of the ellipsoid defined by the FWHM of the acceptance of SCA optic, and D_V is the other minor axis of the ellipsoidal probing volume, which can be calculated from the relationship $(1/D_V)^2 = (1/D_A)^2 + (1/D_B)^2$.[14] In the XYZ description presented in this paper, D_B, D_A and D_V respectively correspond to X, Y and Z. Elemental maps were obtained by spatially rastering the sample through the probing volume along any desired plane within the sample. For the Fe K-edge CXAS measurement, motors were driven to the location of interest chosen from the XFI derived map with spectra recorded by scanning the energy at the XYZ location. Multiple XAS sweeps were collected at each location to verify if oxidation state is affected by X-ray irradiation, but no such indication was observed. Data were taken with 0.3 eV steps and 3 s per pt integration time through the near-edge region and to 150 eV below and 186 eV above for linear background removal and normalization to edge jump. Spectra were energy calibrated with reference to the first inflection point of a simultaneously measured Fe foil, for which the value was assumed to be 7111.3 eV. Standard spectra were reported previously.[21]

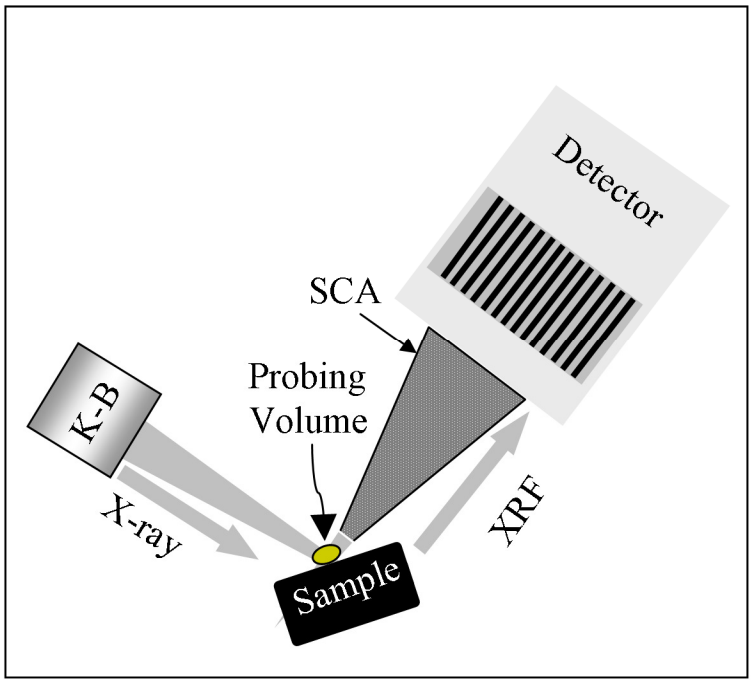

Figure 5.1 A schematic diagram showing SCA based confocal XFI/XAS set-up. Foci of the incident (K-B) and collection (SCA) focusing optics intersect to form the probing volume.

CXFI data were analyzed using the SMAK software package.[22] Recorded fluorescence counts were normalized to the incident intensity and were background corrected by subtracting the average intensity of pixels outside the image from the intensity of each pixel of the image. Fe K near-edge XAS (also called Fe K-edge X-ray absorption near edge structure, or XANES) data were background subtracted and analyzed using the EXAFSPAK suite of programs.[23] In brief, fluorescence counts were first normalized to the incident intensity. Multiple sweeps were examined for possible spectral changes indicative of beam-induced changes, and when none were detected, the multiple sweeps were averaged. To remove background due to scatter and fluorescence from other absorption edges, a function was fitted to the below-edge region of the spectrum and was extrapolated through the remainder of the spectrum such that when subtracted, the above-edge region followed the Victoreen theoretical absorption cross-section function. Spectra were normalized by fitting a spline function through the above-edge region and then dividing by the value of the spline at 7125 eV.

The pre-edge peak region was deconvoluted similarly to the methods of Wilke *et al.*[24] using the EXAFSPAK program EDG_FIT. For each spectrum, a 20 eV region encompassing the pre-edge peaks was fit using least-squares minimization to a background function and one or two pseudo-Voigt peak functions. Refined parameters for the peaks were the height, half-width at half height, and position. Following the method of Wilke *et al.*[24] the pseudo-Voigt mixing (amount of Gaussian versus Lorenzian) was fixed at 50% and where two or more peaks were required to fit a spectrum, the widths of the peaks were constrained to be equal. Following the calculation of peak areas, the peak centroid was calculated as the mean of the peak positions, weighted by the areas. The fit error is the sum of squares of the differences between the data and fit, normalized to the number of points in the fitted range.

Fluorescence self-absorption (also called fluorescence thickness effects) may be of concern when XAS spectra are measured on specimens which are both thick and concentrated in the target element, such that the absorption cross-section of the matrix changes significantly as a function of energy across the target absorption edge.[1] The phenomenon manifests itself as attenuation of high intensity spectral features concomitant with enhancement of lower intensity features. While CXAS samples are inherently "thick", in our case the matrix is predominantly composed of Si, O and other non-Fe elements, such that self-absorption of Fe should be minimized. Evidence to substantiate this comes from the spectra collected at different depths, which do not appear to show any significant suppression of high intensity features or enhancement of low intensity features which would be symptomatic of this spectral artifact. Hence, no special data analysis was used to account for self-absorption in these samples.

5.6 Results and Discussion

5.6.1 CXFI

Figure 5.2 shows elemental maps of Fe, Ca and Mn in a 400 × 400 μm^2 scan area measured from a plane parallel to the surface, situated at a depth of ~15 µm. The map was obtained by scanning the horizontal (X) and vertical (Y) sample position motors with a 5 µm step size and a 1 s integration time, with a total acquisition time of 2 h and 14 min. The bottom-right map shows the superposition of all three elements in which Fe, Ca and Mn are respectively

presented as red, green and blue. The images reveal spatial variation of the elements within the mapped area. Depth profiling of elemental distributions was achieved by recording maps of seven parallel planes, consecutively 10 µm apart. The specimen shows significant heterogeneity in the distribution of the measured elements within this scanned volume. In particular, in Figure 5.2 an oval area shows a significant enrichment in both Ca and Mn compared with surrounding areas.

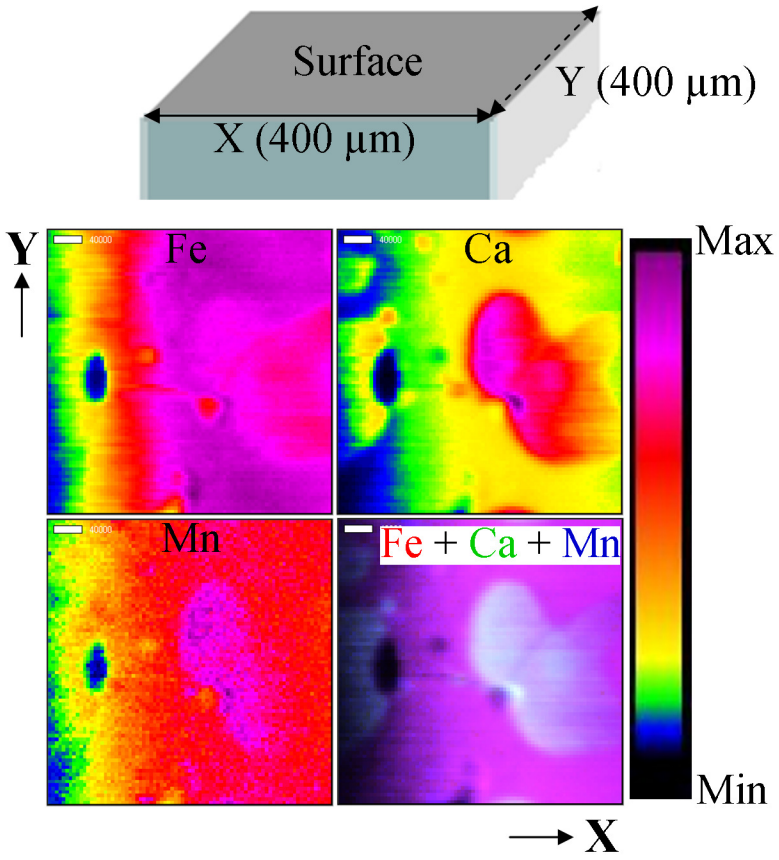

Figure 5.2 Elemental maps of Fe, Ca, and Mn measured from a plane parallel to the surface at a depth of ~15 µm. The bar to the right gives the relative intensity scale. The bottom right map shows a superposition of Fe (red), Ca (green) and Mn (blue). The sketch at the top shows the scanning directions relative to the sample surface. Scalebar = 40 µm.

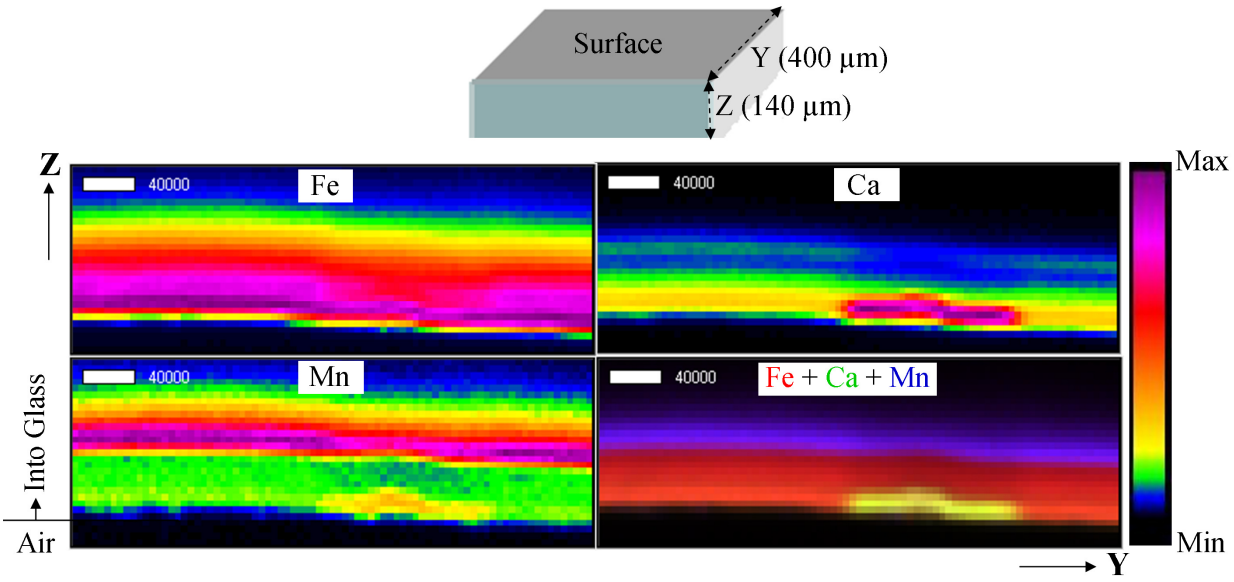

Figure 5.3 Elemental maps of Fe, Ca, Mn measured in a plane normal to the surface. The bar to the right gives the relative intensity scale. The bottom right map shows a superposition of Fe (red), Ca (green) and Mn (blue). The sketch at the top shows scanning directions relative to the sample surface. Zero intensity (dark) at low values of Z originates due to air. Scalebar = 40 µm.

Figure 5.3 represents elemental maps measured in a sample plane perpendicular to the plane presented in Figure 5.2, obtained by scanning vertical (Y) vs. normal to the sample surface (Z) axes. The direction Z corresponds to depth from the sample surface, hence this figure depicts a spatially resolved depth profile of the elemental distributions in a two dimensional view. A 400 (Y) × 140 (Z) μm^2 area was mapped using the same acquisition settings used for Figure 5.2, with an acquisition time of 50 min. The scan range of ~ 100 µm into the sample (Z) covers a significant part of the corrosion layer, which is visible by eye as a less transparent weathering crust on the surface. In Figure 5.3, the interface between air and the corrosion layer at the sample surface is apparent as the sharp boundary between zero and higher intensity (dark to blue/yellow). Once again, a significant heterogeneity in the elemental distribution is observed. In particular, Fe is seen to be enriched at the surface but decreases with distance away from the surface. Conversely, Mn shows lower concentration close to the surface and a narrow band of enrichment, approximately 10 µm wide at approximately 60 µm below the surface. Ca also

shows a high intensity band at the surface with an isolated enrichment of approximately 150 µm wide and only about 10 µm deep. The bands of each element persist across the entire width of the measured sample indicating a layered pattern.

The medieval glass sample investigated in this study belongs to the category of wood ash glasses, which are characterized as a mixture of sand and ash from various trees; ash would have been added to the sand in order to lower the melting temperature of the glass batch.[16] The origin of Ca is therefore most likely from the ash.[25] The presence of Fe could be due to its deliberate addition in order to achieve the green colouration of the glass[26] or simply as an impurity of silica.[27] Mn similarly could be an impurity in the starting materials or added on purpose to compensate the green colour caused by Fe.[28] The leaching of Ca in the corrosion layer as an ion exchange process with hydrogen bearing species is a well understood phenomenon,[17,19] hence the observed presence of Ca in the surface region (Figure 5.3) is expected. Although the presence of alkaline earth ions such as Ca in the corrosion layer is well understood, a limited number of studies is available on the leaching of transition metals such as Fe or Mn into the corrosion layer.[29,30] Our work shows that Fe is concentrated on the surface and gradually decreases as a function of depth, whereas the concentration of Mn is low at the surface, with a buried high concentration band followed by a gradual decrease with further depth. The area of high concentration Ca with co-localized Mn evident in Figure 5.2 in the near surface region is another noticeable detail, whereas the high concentration Mn band does not appear to show such co-localization. More statistics are needed to draw conclusions about such apparent patterns. A larger scale study will generate an improved understanding of the role of transition metals in the corrosion layer.

5.6.2 CXAS

Figure 5.4A shows confocally collected spatially resolved Fe K near-edge XAS measured from selected volume elements of interest in the intact sample. The acquisition time for each spectrum was 16 min. The locations were chosen according to the map shown in the inset to Figure 5.4, labelled *a* through *e*. Pronounced co-localization of Ca with Fe is observed in *a* whereas co-localization of Mn with Fe is observed in *d*. Locations *a* and *b* are close to the surface of the corrosion layer while *c*, *d* and *e* are successively deeper into the corrosion layer

and closer to the actual glass part of the sample. Figure 5.4A shows clear variation in the Fe K near-edge XAS spectra, especially the position and intensity of the pre-edge peaks as well as some shifts in the rising part of the spectrum. Also presented in Figure 5.4A are spectra of Fe standard species. XAS can provide speciation information of elements *in situ* as spectra have characteristic features that depend on chemical environment.[14,31–33] The spectra of locations *a*, *b* and *c* show marked similarity to the octahedral oxygen-coordinated Fe(III) standard (Figure 5.4), indicating that Fe at or near the surface of the corrosion layer is in this coordination environment. The spectra from *d* and *e* are quite distinct from those in *a* through *c*, in particular with more pronounced intensity in the region of the pre-edge peaks. The pre-edge peaks are commonly referred to 1s $\rightarrow$ 3d transitions, formally dipole-forbidden, quadrupole allowed $\Delta l = +2$ transitions which can gain dipole-allowed intensity from admixture of 4p orbitals in non-centrosymmetric transition metal sites.[24]

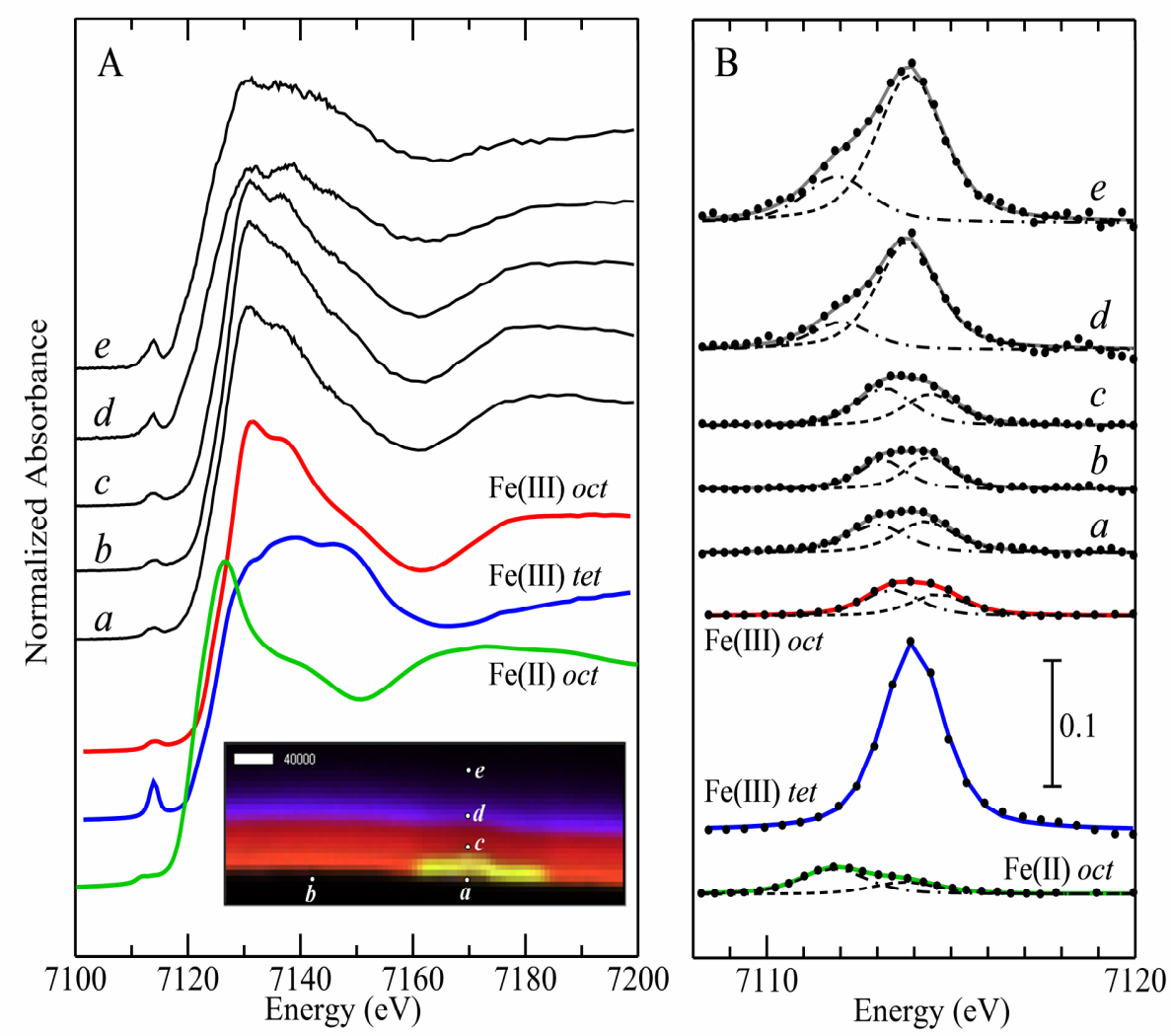

Figure 5.4 A: Confocal Fe K-edge X-ray absorption spectra from different locations within the sample (*a*-*e*), as indicated in the inset (also shown in Figure 5.3). Spectra of Fe standards coordinated by O shown are: octahedral Fe(III) in iron substituted aluminium phosphate [Fe(III)-*oct*]; tetrahedral Fe(III) in iron substituted sodalite [Fe(III)-*tet*]; and octahedral Fe(II) in aqueous ferrous sulfate [Fe(II)-*oct*]. B: Expanded region showing the pre-edge 1s→3d peak region of the same spectra as in A, together with the results of peak-fitting (numerical values shown in Table 1). Each deconvoluted spectrum shows: data points (filled circles); fit (solid grey or coloured line); and pseudo-Voigt fitted peaks (dashed and dot-dashed lines). Both data and fit have had a background function subtracted to isolate the pre-edge features.

Table 5-1 Pre-edge characteristics for Fe at selected locations in the glass corrosion layer in comparison with standards as shown in Figure 5.4. Peak heights are normalized to an edge jump of unity. Width corresponds to the half-width at half-height. Where more than one peak is fitted for a sample, the widths of the two peaks were floated but were constrained to the same value. The fit error is the sum of squares of the differences between the data and the fitted curve, normalized to the number of points in the fitted range.

Location	Height	Position (eV)	Width (eV)	Area	Total area	Centroid (eV)	Fit error
a	0.0220	7112.98	0.946	0.0548	0.1164	7113.68	1.29×10^{-6}
	0.0247	7114.30	0.946	0.0616			
b	0.0230	7113.15	0.751	0.0455	0.0958	7113.80	8.91×10^{-7}
	0.0254	7114.39	0.751	0.0503			
c	0.0300	7113.20	0.890	0.0704	0.1299	7113.78	8.61×10^{-7}
	0.0254	7114.46	0.890	0.0596			
d	0.0219	7112.02	0.973	0.0562	0.2759	7113.44	9.10×10^{-6}
	0.0857	7113.81	0.973	0.2197			
e	0.0369	7111.92	1.070	0.1040	0.4368	7113.42	7.77×10^{-6}
	0.1180	7113.88	1.070	0.3327			
Standard	Height	Position (eV)	Width (eV)	Area	Total area	Centroid (eV)	Fit error
Fe(III)-*oct*	0.0213	7113.40	0.890	0.0500	0.0915	7113.97	3.57×10^{-7}
	0.0177	7114.65	0.890	0.0415			
Fe(III)-*tet*	0.1500	7113.97	0.980	0.3874	0.3874	7113.97	9.37×10^{-6}
Fe(II)-*oct*	0.0204	7111.82	1.060	0.0570	0.0843	7112.44	1.07×10^{-7}
	0.0098	7113.74	1.060	0.0273			

The region of the pre-edge peaks is shown on an expanded energy scale in Figure 5.4B. In several studies of the pre-edge features in materials with iron-oxygen coordination,[24,34,35] the region of the pre-edge peaks has been found to be particularly insightful in providing information both on oxidation state and on coordination environment. Similar to these previous analyses,[24,34,35] Figure 5.4B also includes the results of deconvolution by fitting pseudo-Voigt peak functions to these features, the numerical results of which are shown in Table 1. Previous work has shown that, for single Fe species, the centroid of the pre-edge peaks is a relatively good indicator of the Fe(II) versus Fe(III) oxidation state, independent of the number or geometry of the oxygen ligands. After shifting to our calibrated energy scale, the mean centroid energies for Fe(III) and Fe(II) states are 7113.7 and 7112.3 eV respectively;[24] other workers[35] show values within ±0.1 eV. The observed centroid values for the Fe(III) and Fe(II) standards in our study, at

7114.0 and 7112.4 eV (Table 1), therefore are in good agreement with the previous observations.[24,34,35] The observed centroid values for all points in the glass, which range from 7113.4 to 7113.8 eV, therefore are indicative of a predominantly Fe(III) oxidation state. However, the average energy for the two deeper points, *d* and *e* (7113.4 eV), is slightly lower than the average energy of *a*, *b* and *c* (7113.8 eV) which lie closer to the surface.

Within a given oxidation state, the integrated intensity of the pre-edge feature has been found to be indicative of the coordination geometry of the Fe-O site.[24,34,35] For Fe(III), the non-centrosymmetric tetrahedral sites give rise to the greatest intensity (around 0.26 - 0.36) while the centrosymmetric octahedral sites are lowest in intensity (around 0.06 to 0.13).[24] Our integrated intensity values of 0.39 and 0.09 for tetrahedral and octahedral Fe(III) standards are thus in excellent agreement. For the glass samples, spectra *a*, *b* and *c* show intensities of 0.12, 0.10 and 0.13, consistent with octahedral coordination. In contrast, the intensities of *d* and *e* are 0.28 and 0.44, which indicate a more non-centrosymmetric site and numerically show the most consistency with a tetrahedral coordination. However, whereas our tetrahedral Fe(III) standard and those of Wilke *et al.* show a single prominent peak in the pre-edge region, glasses *d* and *e* show intensity distributed between a prominent peak and an additional lower energy feature. This peak might be attributable to a single Fe(III) site which deviates from the ideal tetrahedral Fe(III), either by distortion or by having an intermediate 5-coordination. Alternatively, this may be explained by co-localization of different iron species, in which the dominant form is tetrahedral Fe(III) but with some admixing of another Fe type. Other authors have carried out detailed consideration of the pre-edge region in mixtures of Fe species.[24,34] Unless the spectrum of the pure end-members are known it is challenging to extract quantitative information in this situation.

Hence, our data are consistent with two environments for Fe in the glass. Near the surface of the corrosion layer (*a* through *c*) the spectra are commensurate with Fe(III) in octahedral coordination. Deeper into the corrosion layer (*d* and *e*), the spectra differ from those near the surface, still consistent with a predominantly Fe(III) site but with a modified or mixed coordination environment. Our observation is consistent with that of Abuin et al.[27], though we differ in interpretation. In their non-confocal XAS study performed on various glasses with

various degrees of weathering damage, they observed a shift to lower energies of the absorption edge position as a function of decreased weathering, which they interpret as a trend from Fe(III) in weathered to Fe(II) in unweathered glass. Qualitatively we see a similar trend in a shift to lower edge energy (Figure 5.4) with increased depth into the sample, consistent with decreased weathering for more buried material. However, rather than to a change in oxidation state, we attribute this to a change in coordination environment of the predominantly Fe(III) site; it seems likely that this is also the case in the study of Abuin et al.[27]

The differences observed in the spectra demonstrate variations in the chemical form of Fe in a range of locations within a single specimen of the corrosion layer, indicating that the chemistry of metals within this layer can have significant nuances with more than a single chemical form expected. Corrosion is a complex process where depending on the nature of the glass and environment, the associated physical, chemical and electrochemical phenomena manifest differently and our results are only based on limited observations. Hence, investigation of additional specimens and elements are necessary to improve the understanding of the corrosion processes. However, our preliminary results presented herein show that establishing a relationship[27] between the chemical form of an element and the degradation can be especially complex due to heterogeneity of chemical form as a function of location. In non-confocal mode, determination of the chemical form of elements is limited by the contribution of XAS originating from a range of depths within the sample. Our study demonstrates that the implementation of the SCA optic for CXAS provides high spatial resolution as a function of depth allowing researchers to significantly extend such speciation research on medieval glasses and related specimens of historical interest.

5.7 Conclusions

The exploitation of a SCA as a collection optic in a confocal XFI/XAS experimental configuration results in significant improvement in the spatial resolution of the experiment. Study of samples such as ancient stained glass specimens, which are often unique, fragile and require depth profiling of elements to understand the mechanisms of processes such as glass corrosion, can greatly benefit from the application of a SCA collection optic. Additionally, as the SCA derived probing volume is energy independent, the resulting energy independent spatial

resolution will result in a less complicated quantification procedure compared with a polycapillary based one. In the present work, we have found that the chemical form of iron varies with locations within the sample, which is contrary to the general belief that elements in such samples are expected to be present in their most stable forms. Our results indicate that elucidating the chemical form of an element is complex as it shows spatial variation within a sample. This work is primarily focused on demonstrating the implementation of the SCA optic, and only a small area of a single specimen was investigated. The analysis of mapping and speciation on a larger scale and in additional related specimens will provide significant information with regards to the relationship between corrosion and elements.

5.8 Acknowledgements

This work was supported by the Canada Foundation for Innovation through funding for BioXAS: Life Science Beamline for X-ray Absorption Spectroscopy at the Canadian Light Source Inc. This work was performed in part at the Cornell NanoScale Facility, a member of the National Nanotechnology Infrastructure Network, which is supported by the National Science Foundation (Grant ECCS-0335765). This work is based upon research conducted at the Cornell High Energy Synchrotron Source (CHESS) which is supported by the National Science Foundation and the National Institutes of Health/National Institute of General Medical Sciences under NSF awards DMR-1332208 and DMR-0936384. SC is a fellow in the Canadian Institutes of Health Research – Training grant in Health Research Using Synchrotron Techniques (CIHR-THRUST). IJP and GNG are supported by Canada Research Chair awards and research in the IJP and GNG laboratories is supported by NSERC, SHRF and CIHR. Data were collected at beamline 20ID-B, Advanced Photon Source. Sector 20 facilities at the Advanced Photon Source, and research at these facilities, are supported by the US Department of Energy - Basic Energy Sciences, the Canadian Light Source and its funding partners, and the Advanced Photon Source. Use of the Advanced Photon Source, an Office of Science User Facility operated for the U.S. Department of Energy (DOE) Office of Science by Argonne National Laboratory, was supported by the U.S. DOE under Contract No. DE-AC02-06CH11357.

5.9 References

(1) Pushie, M. J.; Pickering, I. J.; Korbas, M.; Hackett, M. J.; George, G. N. Elemental and chemically specific X-ray fluorescence imaging of biological systems. *Chem. Rev.* **2014**, *114*, 8499–8541.

(2) Janssens, K.; Proost, K.; Falkenberg, G. Confocal microscopic X-ray fluorescence at the HASYLAB microfocus beamline: characteristics and possibilities. *Spectrochim. Acta B* **2004**, *59*, 1637–1645.

(3) Woll, A. R.; Mass, J.; Bisulca, C.; Huang, R.; Bilderback, D. H.; Gruner, S.; Gao, N. Development of confocal X-ray fluorescence (XRF) microscopy at the Cornell high energy synchrotron source. *Appl. Phys. A* **2006**, *83*, 235–238.

(4) Kanngießer, B.; Malzer, W.; Reiche, I. A new 3D micro X-ray fluorescence analysis set-up – First archaeometric applications. *Nucl. Instrum. Meth. B* **2003**, *211*, 259–264.

(5) Wei, X.; Lei, Y.; Sun, T.; Lin, X.; Xu, Q.; Chen, D.; Zou, Y.; Jiang, Z.; Huang, Y.; Yu, X.; Ding, X.; Xu, H. Elemental depth profile of faux bamboo paint in Forbidden City studied by synchrotron radiation confocal μ-XRF. *X-ray Spectrom.* **2008**, *37*, 595–598.

(6) Kanngießer, B.; Mantouvalou, I.; Malzer, W.; Wolff, T.; Hahn, O. Non-destructive, depth resolved investigation of corrosion layers of historical glass objects by 3D Micro X-ray fluorescence analysis. *J. Anal. At. Spectrom.* **2008**, *23*, 814–819.

(7) Nakano, K.; Tsuji, K. Nondestructive elemental depth profiling of Japanese lacquerware “Tamamushi-nuri” by confocal 3D-XRF analysis in comparison with micro GE-XRF. *X-ray Spectrom.* **2009**, *38*, 446–450.

(8) Guilherme, A.; Coroado, J.; Dos Santos, J. M. F.; Lühl, L.; Wolff, T.; Kanngießer, B.; Carvalho, M. L. X-ray fluorescence (conventional and 3D) and scanning electron microscopy for the investigation of Portuguese polychrome glazed ceramics: Advances in the knowledge of the manufacturing techniques. *Spectrochim. Acta B* **2011**, *66*, 297–307.

(9) Reiche, I.; Röhrs, S.; Salomon, J.; Kanngießer, B.; Höhn, Y.; Malzer, W.; Voigt, F. Development of a nondestructive method for underglaze painted tiles-demonstrated by the analysis of Persian objects from the nineteenth century. *Anal. Bioanal. Chem.* **2009**, *393*, 1025–1041.

(10) Woll, A. R.; Agyeman-Budu, D.; Choudhury, S.; Coulthard, I.; Finnefrock, A. C.; Gordon, R.; Hallin, E.; Mass, J. Lithographically-fabricated channel arrays for confocal X-ray fluorescence microscopy and XAFS. *J. Phys.: Conf. Ser.* **2014**, *493*, 012028 (1–4).

(11) Woll, A. R.; Agyeman-Budu, D.; Bilderback, D. H.; Dale, D. 3D X-ray fluorescence microscopy with 1.7 μm resolution using lithographically fabricated micro-channel arrays. *SPIE Optics and Photonics* **2012**, *8502*, 85020K–1 – 85020K–14.

(12) Sugiro, F. R.; Li, D.; MacDonald, C. A. Beam collimation with polycapillary X-ray optics for high contrast high resolution monochromatic imaging. *Med. Phys.* **2004**, *31*, 3288–3297.

(13) Kanngießer, B.; Malzer, W.; Mantouvalou, I.; Sokaras, D.; Karydas, A. G. A deep view in cultural heritage—confocal micro X-ray spectroscopy for depth resolved elemental analysis. *Appl. Phys. A* **2012**, *106*, 325–338.

(14) Silversmit, G.; Vekemans, B.; Nikitenko, S.; Schmitz, S.; Schoonjans, T.; Brenker, F. E.; Vincze, L. Spatially resolved 3D micro-XANES by a confocal detection scheme. *Phys. Chem. Chem. Phys.* **2010**, *12*, 5653–5659.

(15) Denecke, M. A.; Brendebach, B.; De Nolf, W.; Falkenberg, G.; Janssens, K.; Simon, R. Spatially resolved micro-X-ray fluorescence and micro-X-ray absorption fine structure study of a fractured granite bore core following a radiotracer experiment. *Spectrochim. Acta B* **2009**, *64*, 791–795.

(16) Hormes, J.; Roy, A.; Bovenkamp, G.-L.; Simon, K.; Kim, C.-Y.; Börste, N.; Gai, S. Medieval glass from the Cathedral in Paderborn: a comparative study using X-ray absorption spectroscopy, X-ray fluorescence, and inductively coupled laser ablation mass spectrometry. *Appl. Phys. A* **2013**, *111*, 91–97.

(17) Melcher, M.; Wiesinger, R.; Schreiner, M. Degradation of Glass Artifacts : Application of Modern Surface Analytical Techniques. *Acc. Chem. Res.* **2010**, *43*, 916–926.

(18) Lombardo, T.; Loisel, C.; Gentaz, L.; Chabas, A.; Verita, M.; Pallot-Frossard, I. Long term assessment of atmospheric decay of stained glass windows. *Corros. Eng., Sci. Technol.* **2010**, *45*, 420–424.

(19) Schreiner, M. M. and M. *Modern Methods for analysing Archeological and Historical Glass*; Janssens, K., Ed.; Wiley, 2013; pp. 609–651.

(20) Lobbedey, U. *Die Ausgrabungen im Dom zu Paderborn 1978/80 und 1983*; Bonn : R. Habelt, 1986; Vol. 1-4.

(21) Cotelesage, J. J. H.; Pushie, M. J.; Grochulski, P.; Pickering, I. J.; George, G. N. Metalloprotein active site structure determination: synergy between X-ray absorption spectroscopy and X-ray crystallography. *J. Inorg. Biochem.* **2012**, *115*, 127–137.

(22) Webb, S. SMAK version 1.01, Stanford Synchrotron Radiation Laboratory, Menlo Park, CA, USA, **2012**.

(23) Graham N. George, EXAFSPAK, University of Saskatchewan, Saskatoon, SK, Canada, **2001**.

(24) Wilke, M.; Farges, F.; Petit, P.-E.; Brown Jr., G. E.; Martin, F. Oxidation state and coordination of Fe in minerals : An Fe K-XANES spectroscopic study. *Am. Mineral.* **2001**, *86*, 714–730.

(25) Wedepohl, K. H.; Simon, K. The chemical composition of medieval wood ash glass from Central Europe. *Chemie der Erde* **2010**, *70*, 89–97.

(26) Wedepohl, K. H. *Glas in Antike und Mittelalter – Geschichte eines Werkstoffes*; E. Schweizerbart'sche Verlagsbuchhandlung (Nägele u. Obermiller): Stuttgart, 2003.

(27) Abuín, M.; Serrano, A.; Chaboy, J.; García, M. A.; Carmona, N. XAS study of Mn, Fe and Cu as indicators of historical glass decay. *J. Anal. At. Spectrom.* **2013**, *28*, 1118–1124.

(28) Cagno, S.; Nuyts, G.; Bugani, S.; Vis, K. De; Schalm, O.; Joost, C.; Lukas, H.; Cotte, M.; Peter, R.; Janssens, K. Evaluation of manganese-bodies removal in historical stained glass windows via SR-μ-XANES-XRF and SR-μ-CT. *J. Anal. At. Spectrom.* **2011**, *26*, 2442–2451.

(29) Schalm, O.; Proost, K.; De Vis, K.; Cagno, S.; Janssens, K.; Mees, F.; Jacobs, P.; Caen, J. Manganese staining of archaeological glass: the characterization of Mn-rich inclusions in leached layers and a hypothesis of its formation. *Archaeometry* **2011**, *53*, 103–122.

(30) Sterpenich, J.; Libourel, G. Using stained glass windows to understand the durability of toxic waste matrices. *Chem. Geol.* **2001**, *174*, 181–193.

(31) Janssens, K.; Alfeld, M.; Van der Snickt, G.; De Nolf, W.; Vanmeert, F.; Radepont, M.; Monico, L.; Dik, J.; Cotte, M.; Falkenberg, G.; Miliani, C.; Brunetti, B. G. The use of synchrotron radiation for the characterization of artists' pigments and paintings. *Annu. Rev. Anal. Chem.* **2013**, *6*, 399–425.

(32) Wilke, M.; Appel, K.; Vincze, L.; Schmidt, C.; Borchert, M.; Pascarelli, S. A confocal set-up for micro-XRF and XAFS experiments using diamond-anvil cells. *J. Synchrotron Radiat.* **2010**, *17*, 669–675.

(33) Bertrand, L.; Robinet, L.; Thoury, M.; Janssens, K.; Cohen, S. X.; Schöder, S. Cultural heritage and archaeology materials studied by synchrotron spectroscopy and imaging. *Appl. Phys. A* **2011**, *106*, 377–396.

(34) Jackson, W. E.; Farges, F.; Yeager, M.; Mabrouk, P. A.; Rossano, S.; Waychunas, G. A.; Solomon, E. I.; Brown Jr., G. E. Multi-spectroscopic study of Fe(II) in silicate glasses: Implications for the coordination environment of Fe(II) in silicate melts. *Geochim. Cosmochim. Ac.* **2005**, *69*, 4315–4332.

(35) Gabriele, G.; Pratesi, G.; Cipriani, C.; Paris, E. Iron local structure in tektites and impact glasses by extended X-ray absorption fine structure and high-resolution X-ray absorption near-edge structure spectroscopy. *Geochim. Cosmochim. Ac.* **2002**, *66*, 4347–4353.

Chapter 6. Spoked Channel Array Optics Based Confocal X-ray Techniques Enable Superior Resolution Mapping and Highly Localized Speciation of elements: Application to Archaeological Human Bone

6.1 Preface

The study presented in the previous chapter investigated a non-biological sample, a medieval stained glass, using a SCA optic based CXFI and CXAS. As a final step, this thesis aimed at studying a biological sample, an archaeological human bone, using SCA based CXFI and CXAS. By implementing a superior resolution SCA optic, this chapter presents important outcomes such as high resolution elemental maps of bone microstructures, highly localized spectroscopic information within a sample, and advantages of employing SCA optics in studying low Z elements such as Ca.

6.2 Manuscript Author Contributions

A modified version of this chapter will be submitted as a manuscript to a peer-reviewed journal. The author names and contributions are provided below.

Sanjukta Choudhury, David N. Agyeman-Budu, Arthur R. Woll, Robert A. Gordon, Treena Swanston, Tamara Varney, D. M. L. Cooper, Emil Hallin, Graham N. George, Ian Coulthard and Ingrid J. Pickering

S. Choudhury collected and analyzed the data, and drafted the manuscript.

D. N. Agyeman-Budu and A. R. Woll designed and fabricated the SCA optics.

R. A. Gordon assisted with the experimental configurations at the beamline.

T. Swanston provided ICP MS results, and prepared bone samples for CXFI.

T. Varney provided bone samples and results of the craniofacial and pubic symphysis study.

D. M. L. Cooper provided inputs in interpreting bone data.

E. Hallin assisted with the data collection, submitted the proposal for beamtime at 20ID-B, and provided important insights.

I. Coulthard, G. N. George, and I. J. Pickering supervised this research, providing guidance, scientific input, comments for improving manuscript, and funding.

6.3 Abstract

CXFI and CXAS are of particular interest when the localization and speciation of trace elements are to be determined in a biological sample. The confocal mode facilitates preservation of sample integrity by enabling optical sectioning of samples, thus avoiding physical thin sectioning. A higher signal to noise ratio, especially favorable for dilute biological samples, is also a consequence of the selective confocal detection.

Existing confocal X-ray instruments generally employ polycapillary X-ray optics to receive fluorescence emitted only from the small confocal or probe volume. However, these optics both limit and impose variation on the spatial resolution in CXFI and CXAS, restricting their applications. Here, we employ a novel X-ray detection focusing optic, the SCA, in the CXFI and CXAS study of an archaeological human bone sample recovered from the Royal Naval Hospital Cemetery, Antigua. We present a comparison of bone elemental maps, collected using various modes of XFI to demonstrate the advantage of employing SCA optic based CXFI in collecting superior resolution maps. In particular, the use of SCA-based optics, has made collecting superior resolution maps possible for Ca, a light element, due to the SCA confocal volume being essentially independent of energy, unlike that of a polycapillary. Additionally, our CXAS results, which represent the first SCA based biological CXAS, showed Pb speciation data collected from micro-volumes with dimensions comparable to bone microstructures. We speculate that such high resolution results can be beneficial in determining the origin of Pb: whether the observed Pb is biogenic or diagenetic - a question often encountered in the study of archaeological bone. The application of novel SCA optic enhances the current capability of CXFI and CXAS, extending the scope of the techniques to resolutions approaching 2 microns and to light elements.

6.4 Introduction

Increasing interest in the mechanisms and functions of trace elements in biological systems has triggered significant improvement in technologies employed for revealing the distribution and speciation of trace elements in biological systems.[1–7] Trace element concentrations are often determined in biological samples after homogenization of cell types or acid digestion in techniques such as inductively coupled plasma atomic emission spectrometry (ICP AES) and ICP MS;[8] however, this approach is invasive and offers limited resolution.[6] Techniques that employ membrane diffusible fluorescent probes are invaluable for studying elements in live samples,[6] enabling the reporting of subcellular resolution distributions for cations such as zinc[9] or copper.[10,11] However, use of these probes limits the simultaneously detectable number of elements and requires substantial sample preparation.[9–12] In addition, these probes are rather indirect, with the observed response being dependent on the thermodynamic and kinetic availability of the metal ions.[7] Therefore, this strategy may not allow the detection of the entire inventory of an element within a sample as some may be adventitiously labelled, resulting in an anomalous reading.

Conventional XFI[13] allows direct and simultaneous visualization of multiple elements in two dimensions. It is largely non-destructive and can be extended to include the speciation study of elements.[7] However, it lacks depth resolving capability and therefore, for the best spatial resolution results, requires samples to be thinned to a thickness approximately equal to the desired depth resolution.[14] Tomographic XFI,[15–17] a special variant of XFI, provides a means of viewing the elemental distributions in three dimensions, unlike the two dimensional visualization in conventional XFI. While useful, this mode of XFI restricts the sample thickness and density; as the fluorescent X-ray beam must pass through the sample thickness to reach the detector throughout the angular rotation of sample, generally 180 degrees. Additionally, fluorescence tomography is challenging for speciation as this would require reconstruction of spectra from multiple angles. Another special variant of XFI, CXFI,[18,19] avoids some of these restrictions.

CXFI enables depth resolving capability while offering all the advantages available in XFI. It can readily be extended to CXAS to collect speciation data from a localized voxel of interest anywhere within a sample as long as the emitted fluorescence is not completely

attenuated by the overlying sample thickness. A CXFI experiment enables depth resolution by implementing an additional detection focusing optic, traditionally a polycapillary optic,[20,21] between the sample and the detector. The intersection of incident and detection foci creates a voxel, named confocal volume or probe volume, which allows optical sectioning of a thick or intact sample. A CXFI experiment is therefore especially valuable when studying biological samples as it avoids physical thin sectioning or ablative depth profiling methods, thus preserving sample integrity. Moreover, CXFI offers improved signal to noise since the scatter in CXFI arises only from the confocal volume, a particularly favorable feature for measuring dilute biological samples. While a polycapillary optic is well suited as a confocal detection optic since it offers a large solid angle of collection and operates over a large energy range, it imposes a limitation on the achievable depth resolution. The best resolution offered by a commercially available polycapillary is ~8 μm at 17.5 keV with a working distance of ~2 mm.[22] Since the polycapillary resolution decreases with energy,[21] the resolution is severely limited in the low energy regime (2 - 5 keV), for which the highest reported resolution is ~20 μm.[23] While this resolution is sufficient for many applications, an improved resolution is of interest when inhomogeneity on a scale of only a few microns is expected, which is often the case for the biological samples.

This paper demonstrates the scope and advantages of implementing two recent versions of novel SCA detection optics[23–25] in achieving superior resolution mapping and highly localized speciation of elements. A SCA optic, which is fabricated using the electron beam lithographic techniques and DRIE, consists of micron-scale arrays of collimating channels arranged like spokes of a wheel, all focused on a single source position.[23,24] The fundamental difference between a SCA and a polycapillary arises from the use of collimating channels in the former, rather than reflective glass capillaries in the latter, in order to selectively transmit fluorescence from sample to the detector. Additionally, the SCA spatial resolution, which is solely determined by the length and width of the device channels, is nearly energy independent in contrast to polycapillary resolution, which is dependent on the critical angle for total external reflection, thus on energy.[23,24] Two designs of SCA optic, both fabricated from silicon, have been reported to date.[23,24] In the first, an array of micron scale collimating channels etched on a substrate were implemented,[23] whereas in the second, instead of just etching, the collimating channels were

formed by a staggered array of pillars, whose side-walls were tapered away from the channel axis.[24] The latter design offered a higher efficiency through the implementation of deeper channels, together with an increased working distance through the tapering of channels from the channel axis.[24] Recently, a new version of the SCA optic has been fabricated from a germanium substrate in order to achieve operation at higher energies (up to 30 keV) as suggested in "ray"-tracing simulations designed to model SCA behavior.[23] The current study implemented two optics with depth resolutions approximately 7 μm and 2.5 μm, fabricated from silicon and germanium substrates, respectively.

The initial imaging and spectroscopy results measured from a biologically relevant sample, an archaeological human bone, excavated from the Royal Naval Hospital Cemetery (c. A.D. 1793-1822) near English Harbor in Antigua, are presented. Bone samples from this cemetery were previously investigated to shed light on historical questions such as whether lead (Pb) poisoning played a role in the demise of the British military in the West Indies, and whether the observed Pb is deposited during life (biogenic) or through post-mortem contamination (diagenetic).[26,27] One of the studies employed a strategy of matching the Pb distributions with bone microstructures as a way to determine the nature (biogenic or diagenetic) of Pb;[27] however, the results lacked high resolution maps, which could provide improved detail about the Pb incorporation in bone microstructures. Similar reasoning can be applied to another previous XFI study, which reported the evidence of biogenic mercury in a bone sample from the same cemetery.[28] The fragile nature of samples due to poor preservation of archaeological bone precluded the creation of sufficiently thin sample sections (of the order of a few microns thick), which is a prerequisite for high resolution results using conventional XFI. In the present study, various modes of XFI were employed to collect maps of successively improved resolutions, and a 2.5 μm resolution SCA optic was implemented to collect Pb speciation data, which presented the first demonstration of SCA based biological CXAS. The analysis of the results illustrated the potential of applying high resolution CXFI and CXAS to differentiate whether a toxic element has biogenic or diagenetic origins, a topic of key importance in bioarchaeology.

6.5 Materials and Methods

6.5.1 Samples

The archaeological bone samples were recovered from the Royal Naval Hospital cemetery (c. A.D. 1793-1822) near English Harbour, Antigua. These samples were recovered during the mitigation of the cemetery due to encroachment by modern construction. Ethics approval was obtained from the University of Saskatchewan Biomedical Research Ethics Board prior to study. An analysis of craniofacial features indicated the subject to be of European descent, and an assessment of pubic symphysis estimated the subject to be a male with an age range of 40 - 45 years. An initial bulk analysis of bone fibula sample using standard ICP MS method, performed at the Department of Geological Sciences at the University of Saskatchewan, determined the elemental concentrations to be 304,251 ppm for calcium (Ca), 101.9 ppm for Pb, and 364.8 ppm for strontium (Sr). This study reports a rib section thinned to a thickness of 0.18 mm measured using conventional XFI, and a fibula section thinned to 2.95 mm measured using CXFI experiments. Both samples are obtained from the same subject. Details of the thin section preparation have been published previously.[27]

6.5.2 Experiments

All imaging and spectroscopy experiments were carried out at the 20ID-B beamline of the APS at the Argonne National Laboratory (Illinois, USA), with the storage ring operating in continuous top-up mode at 102 mA and 7.0 GeV. The incoming beam was tuned to the desired excitation energy of 16.5 keV (with an estimated intensity of 10^{12} photons/sec and 10^{11} photons/sec respectively for the beamsizes of 5×5 μm^2 and 2×2 μm^2) by using a liquid-nitrogen-cooled Si (111) double crystal monochromator with a second crystal detuned by 15% to reduce harmonic contamination. A micro-beam of desired spot size was produced using Rh-coated silicon based K-B style focusing mirrors, which also served to provide additional harmonic rejection. An ionization chamber filled with nitrogen gas monitored the intensity of the incident X-ray beam, I_0, which was used for the normalization of the fluorescence; this process eliminated the impact of any possible flux variations of the source. The beamline setup offered multiple cameras, which facilitated viewing of the sample during alignment or scanning. Both

sample and detector were mounted on high precision motorized stages. The sample was oriented at 45˚ (for polycapillary based measurements) and 30˚ (in case of SCA based measurements) to the incident beam and detector. The emitted fluorescence were detected using a Si-drift Vortex® detector (SII NanoTechnology USA Inc.) by implementing three different detection strategies described below and sketched in Figure 6.1.

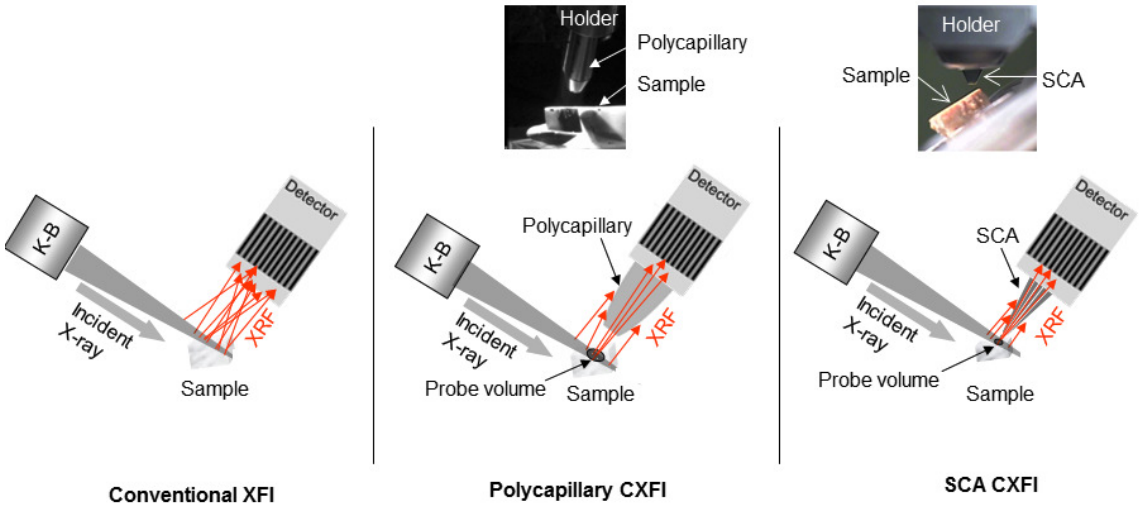

Figure 6.1 Schematic diagram showing differences between conventional XFI, polycapillary and SCA based CXFI setups. Conventional XFI has no detection focusing optic, hence detection of X-ray fluorescence (XRF) may occur at anywhere along the incident X-ray path as long as the spot is within the detection solid angle of the detector. In polycapillary and SCA based CXFI, detection is limited to the respective probe volumes. The SCA optic allows forming a smaller probe volume compared to the polycapillary. Insets show photographs taken by the beamline camera during CXFI experiments.

6.5.2.1 Conventional XFI

For the conventional XFI experiment (left panel, Figure 6.1), the excitation energy was selected to be 16.5 keV, above the K absorption edge of Sr, so that the distribution of Sr in the bone sample can be mapped. A K-B mirror pair[29] was used to create an incident micro-beam of approximately 5 μm × 5 μm spot size, which determined the spatial resolution available in the experiment. Conventional XFI allows the resolution of features in two dimensions, while the third dimension remains unresolved. Therefore the third dimension (say, thickness) of the sample has to be thinned sufficiently to be comparable to the expected resolution along this direction. Data were collected using step scan mode with a pixel resolution of 20 μm × 20 μm and 100 ms per point integration time. The measurement time required for this data set was approximately 2.5 hrs.

6.5.2.2 Polycapillary based CXFI

CXFI configurations are established by implementing an additional focusing optic in front of the detector so that although excitation occurs everywhere along the incident beam path, detection only occurs of photons originating from the probe volume. The spatial resolution available in a CXFI experiment is three dimensional, and determined by the dimensions of ellipsoidal probe volume produced by the intersection of incident and detection foci.[30] Figure 6.2 presents a schematic diagram showing the axes of the ellipsoidal probe volume. The axes *a* and *b* of the ellipsoidal probe volume respectively correspond to the depth resolution of the detection focusing optic and beam size, and the axis *c* is determined from the convolution of *a* and *b* using the formula $(1/c)^2 = (1/a)^2 + (1/b)^2$ as described by Silversmit et al.[30] The volume (V) of the ellipsoid, whose axes are *a*, *b* and *c*, can be calculated as $V= (4/3)\pi abc$.

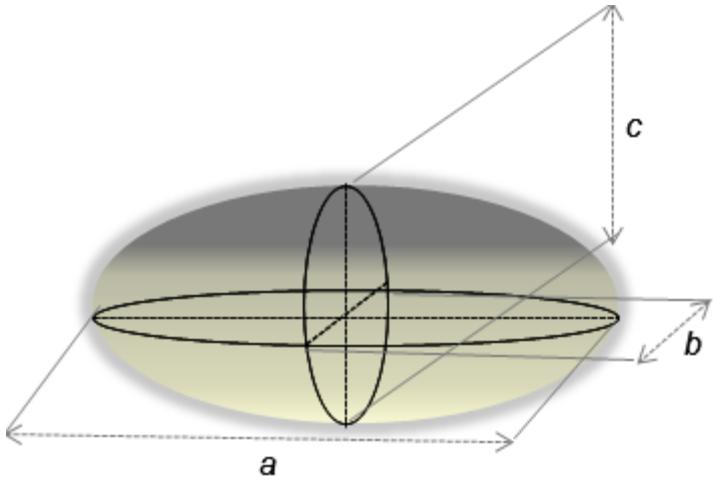

Figure 6.2 Schematic diagram showing axes of the ellipsoidal probe volume.

For a polycapillary based CXFI experiment, a polycapillary detection optic is installed in front of the detector as shown in the middle schematic panel of Figure 6.1. The diagram shows that only the fluorescent photons originating from the probe volume are registered by the detector, while others are restricted from entering the polycapillary. The experiment reported herein employed a microbeam of approximately 5 µm × 5 µm spot size in combination with a polycapillary optic (XOS®) of depth resolution 25 µm (at Mo Kα; 17.4 keV), which yielded a probe volume with axes 25, 5 and 5 µm (*a*, *b* and *c*) at Mo Kα.[30] The polycapillary depth resolution is inversely dependent on energy.[21] Hence the measured depth resolution for Pb Lα (10.5 keV) was found to be 40 µm, greater than the value at Mo Kα. Thus the estimated value for Sr Kα (14.1 keV) and Ca Kα (3.6 keV) would respectively be somewhat smaller (< 40 µm) and significantly larger (>> 40 µm) compared to the value at Pb Lα (10.5 keV). The fluorescence originating from the probe volume is conducted through the capillaries via total external reflection to arrive at the detector. Elemental maps were obtained by spatially rastering the sample through the probe volume along any desired plane within the sample. Data were collected using fly scan mode with a pixel resolution of 5 µm × 5 µm and 100 ms per point integration time. The measurement time required for the data was approximately 4 hrs.

6.5.2.3 SCA based CXFI

In a SCA based CXFI configuration, the detection focusing optic installed in front of the detector is a SCA optic, as schematically shown in the right side panel of Figure 6.1. This setup shows two major differences compared with the polycapillary based one: firstly, the smaller probe volume, hence higher spatial resolution; and secondly, a shorter working distance, hence less room for sample translation between the tip of optic and probe volume. The CXFI data obtained using two SCA optics of depth resolutions 7 μm and 2.5 μm are reported in this study. The 7 μm SCA optic, fabricated from a silicon wafer, was comprised of 96 channels each approximately 7 μm × 200 μm × 4 mm (width × depth × length) with a working distance of approximately 1.5 mm. The 2.5 μm SCA optic was germanium based comprising of 101 channels each approximately 2.5 μm × 200 μm × 4 mm (width × depth × length) with an approximate working distance of 1 mm. The microbeam sizes employed with 7 μm and 2.5 μm SCA optics were approximately 3 μm × 3 μm, and 2 μm × 2 μm, which respectively yielded approximate probe volume axes of 7, 3 and 2.75 μm and 2.5, 2 and 1.5 μm as calculated above. In case of SCA optics, the probe volume is nearly independent of energy.[23] The fluorescence originating at the probe volume travels through the collimating channels to arrive at the detector. Elemental maps were obtained by spatially rastering the sample through the probe volume along any desired plane within the sample. Both 7 μm and 2.5 μm SCA optics were implemented in measuring the same bone sample which also was measured using the above polycapillary based CXFI. Data were collected employing step scanning mode, using pixel resolutions of 5 μm × 5 μm, and 2.5 μm × 2.5 μm respectively for 7 μm and 2.5 μm SCA optics, and using a integration time of 100 ms per point. The measurement time for each case was approximately 11 hrs.

6.5.2.4 SCA based CXAS

The 2.5 μm SCA optic was employed for Pb L_3 CXAS in bone, in which XYZ motors associated with sample stage were driven to the locations of interest chosen from the CXFI map, and the spectra were recorded by scanning the energy of the incident X-rays at a fixed XYZ location. Data were taken with 0.5 eV steps and 3 s per point integration time through the near-edge region and to 100 eV below and 186 eV above for linear background removal and normalization to edge jump. In order to improve signal to noise ratio and to check for possible

effects of irradiation, ten sweeps were collected at each location. No indication of irradiation effect was observed. The acquisition time for each spectrum was 12 min. Spectra for the Pb standards were collected at beamline 7-3 at SSRL.

6.5.3 Data analysis

Data were analysed using the SMAK software package (http://home.comcast.net/approximatelysam_webb/smak.html). The recorded fluorescence counts were normalized to the incident intensity I_0 and were background corrected by subtracting the average intensity of pixels outside the image from the intensity of each pixel of the image. CXAS data were analyzed using the EXAFSPAK suite of programs (http://www-ssrl.slac. stanford.edu/exafspak.html).

6.6 Results and Discussion

6.6.1 Elemental mapping in archaeological human bone

Figure 6.3 shows elemental maps for Pb, Sr and Ca collected using various modes of X-ray fluorescence imaging indicated on the left. Two different bone samples recovered from the same subject were measured, a rib section for conventional XFI and a fibula section for all CXFI. Since the images for both sections were measured in the cortical region of bone, similar general structural features such as osteons are expected to be seen in the maps. Unlike rib, the fibula sample was extremely fragile due to poor preservation. Hence the challenge associated with thin sectioning made the fibula sample a logical candidate for CXFI. The data for each mode were collected during separate beamtime runs at 20ID-B, hence the spatial region within the sample mapped in each CXFI mode is different. The dimensions of the mapped area varied with the measuring modes and setups due to the variation in required measuring time per unit area.

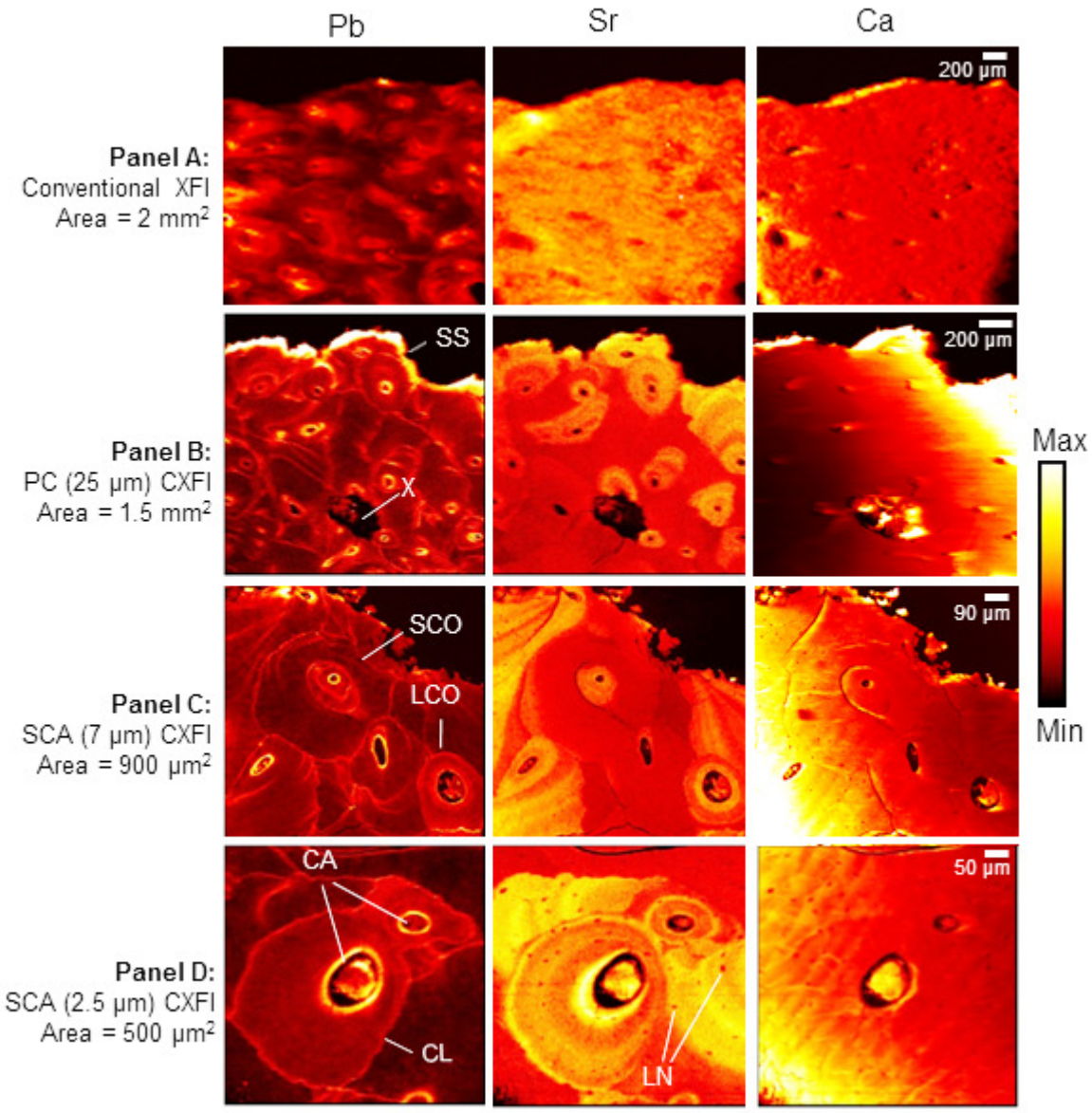

Figure 6.3 Elemental (Pb, Sr and Ca) maps from archaeological human bone samples collected using various XFI configurations presented in panels denoted on the left. All samples are from same archaeological subject: panel A presents a rib section, and panels B, C and D present different regions of a fibula sample. Scale bars, which are same for all elements within a panel but different for each panel, are shown in the Ca-maps. Inter-panel or inter-element intensities are not normalized to each other. PC: polycapillary, SCA: spoked channel array, SCO: small canal osteon, LCO: large canal osteon, CA: osteonal canals, CL: cement lines, SS: sample surface, LN: lacunae and X: an unknown feature (possibly due to bone resorption). The depths of subsurface areas mapped in CXFI with respect to the sample surface are 200 µm, 20 µm and 10

μm respectively for panels B, C and D. In the colour-legend, the low intensity levels are represented by black and darker red, and the higher intensity levels in yellow through white.

6.6.1.1 Conventional XFI

The images shown in panel A of Figure 6.3 are measured using a conventional XFI experiment. This technique lacks depth resolving capability due to the absence of detection focusing optics, hence requires samples to be thinned to a thickness similar to the desired depth resolution. The bone sample measured here was approximately 180 μm thick as creating a thinner sample was not possible due to its fragility. The Pb-map shows blurry osteon-like structures with some three dimensional information, such as the orientation of the cylindrical osteonal structures arising from the superposition of fluorescence originating from a range of depths within the sample. The Sr and Ca maps show rather a uniform distribution throughout except for the osteonal canals which appear as "holes", or low to zero concentration. Although these maps show a clear variation among the distributions of Pb, Sr and Ca, a detailed element to structure localization information is not available. These maps demonstrate the challenge of employing conventional XFI in investigating irregular three dimensional features such as osteons in an insufficiently thin sample. Additionally, the results from conventional XFI experiments are likely to suffer from a limited signal to noise ratio. The detection of both fluorescence and scatter occur at most places along the incident beam path (Figure 6.1) such as various sample depths (to the limit of fluorescence attenuation), some air, windows and sample holders. While a limited signal to noise ratio negatively affects all experiments, this would be of particular significance when a dilute biological sample is of interest since the excessive scatter would cause the detector deadtime effect.[13]

6.6.1.2 Polycapillary based CXFI

Data presented in panel B of Figure 6.3 are measured using a polycapillary based CXFI. The fundamental difference between this and conventional XFI arises from the use of a polycapillary detection focusing optic, which restricted the collection of fluorescence to its focal spot. Here, a poorly preserved fragile sample of 2.95 mm thickness is measured. Although this is a fairly thick sample compared to the one measured using conventional XFI, a remarkably

improved spatial resolution is achieved, particularly in the Pb and Sr maps. This is because the rastering of the sample through the probe volume in CXFI allowed optical sectioning of the sample. CXFI enables collection of maps from an area or volume of interest anywhere within a three dimensional sample as long as the emitted fluorescence is not completely attenuated by the overlying sample thickness. A comparison with the maps obtained from conventional XFI (panel A) demonstrates the value of CXFI in achieving higher spatial resolution maps from a sample for which thinning is difficult or impractical. The inherently higher signal to noise ratio offered by the confocal mode also contributes to the clearer appearance of the weak features such as remnants of older osteons.

A considerable variation is observed in the intensities of Pb throughout the map. A significantly higher accumulation of Pb is observed particularly in the canal walls and cement lines, likely due to a biogenic type of uptake as the cement surface layer is exposed to the interstitial fluid during bone remodeling.[31] Interestingly, while some of the canal walls show higher concentrations, others show very low levels; this may be due to the variation in the extent of exposure to Pb during the formation of a certain canal wall. A high concentration Pb layer is observed in the sample surface, the outer surface which was exposed to the burial environment. Since this accumulation is present throughout the imaged surface and does not show any correlation with bone microstructures, it may be an indication of diagenesis.

The Sr distribution is different from that of Pb. Only some osteons show higher Sr concentrations, while others show low; this may be linked with the change in diet during the formation of osteons, as will be discussed below. In the case of high Sr concentration osteons, the entire structure appears to be enriched in Sr relative to the surrounding bone.

The Ca map shows noticeable intensity variations across the map (zero to low intensities on the left and lower side, and high intensities on the upper right corner) as a collective consequence of several factors. First and foremost, the overlying sample thickness between the confocal plane and sample surface varies with spatial locations, likely as a result of a small mismatch of the plane of the bone specimen surface with the plane of scanning. Other factors include porosity of the bone which also may vary with spatial locations. It is the low energy

fluorescence which suffers most attenuation; therefore such effect is not apparent in the maps of Pb or Sr. Another observation regarding the Ca map includes a limited spatial resolution in comparison with Pb and Sr maps in the same panel. For instance, the osteonal canals are better resolved in the Pb and Sr maps compared to Ca map. This is due to the poorer polycapillary depth resolution for low energy Ca fluorescence, as predicted by the energy dependent nature of polycapillary.[21] A 'broken hole' looking feature denoted by X, which could be due to bone resorption, looks darker in Pb and Sr maps but appears significantly different in the Ca map. The extra features appearing as higher intensities inside the hole are likely due to a larger probe volume in the case of Ca.

While the maps obtained using a polycapillary optic show a substantial improvement in the clarity of element to structure visualization compared to the maps in conventional XFI, a further improvement can be anticipated if smaller probe volumes are employed.

6.6.1.3 SCA (7 μm) based CXFI

Data presented in panel C of Figure 6.3 are collected using SCA optics based CXFI experiment. A 7 μm SCA optic is used in conjunction with an approximate beam size of 3 μm × 3 μm, thus employing a probe volume with axes 7, 3 and 2.75 μm, which is smaller than the polycapillary derived probe volume dimensions 40, 5 and 5 μm. Since the pixel size (5 μm × 5 μm) employed in both cases was the same, it is the 6-fold improvement in depth resolution (7 μm compared with 40 μm) which is expected to contribute to the difference in spatial resolution. A comparison with the maps obtained from the polycapillary based measurements (panel B) show a clear improvement in map quality. The variations in Pb intensities among canal walls, cement lines and osteons are now much more clearly visible. Interestingly, while Pb is observed on most cement lines and canal surfaces, we see at least one osteon which is highly enriched in Pb. The Sr map also shows clearer details in the distributions across the map. Interestingly, the distributions among the osteons are not similar; while some are rich in Sr some show lower Sr concentrations. A younger looking osteon identified by a larger canal osteon (LCO), which likely was undergoing formation when death occurred, shows Pb and Sr within the canal, while this particular osteon also exhibits enrichment in Pb throughout the whole structure. Since the

osteonal canal contains blood supply, the presence of Pb and Sr is not surprising inside the canal. Importantly, it may imply the subject's exposure to Pb at the time of death. The other explanation for the presence of Pb and Sr in the canal could be the grinding of the sample surface during sample preparation which may leave microscopic debris of bone trapped inside the canal. However, the combination of both the enrichment of Pb throughout the osteon and the occurrence of Pb within the canal better supports the former. Another possibility could be leaching of Pb and Sr into the canal through diagenesis; however the accumulation only in this particular canal rather than all of them seems less likely in the case of diagenesis. Smaller intensity variations across the Ca-map in comparison to its counterpart in panel B can be attributed to smaller variations in the overlying sample thickness on the confocal plane as a function of spatial locations. Since a smaller area is mapped compared to panel B, a less variation in overlying sample thickness is expected. Interestingly, while the Pb and Sr show incremental improvement in spatial resolution compared to their counterparts in panel B, the Ca shows a greater improvement going to the SCA optic. This is due to a greater improvement in the depth resolution for Ca map, compared to the Pb or Sr, going from polycapillary to SCA. The other factor is the improved signal to noise ratio in panel C compared to panel B due to the closer proximity to the sample surface (depths are 200 µm, and 20 µm respectively for panels B and C), and use of a smaller probe volume. Additionally, here all three maps (Pb, Sr and Ca) appear to be of similar resolution; a careful observation show tiny low intensity circular bone microstructures, called lacunae, are of 2-3 pixels in both Sr and Ca. This is expected in accordance with the nearly energy independent nature of SCA optics with regard to spatial resolution.[23]

In spite of the improvement, the spatial resolution is still insufficient to resolve bone microstructures such as the width of an individual cement line, which is in the range of 2 µm.[31] Hence the fluorescence signal averaged over a larger matrix volume than the true feature occupies is observed in the maps.

6.6.1.4 SCA (2.5 µm) based CXFI

The SCA based CXFI data presented in panel D of Figure 6.3 are collected by implementing a higher resolution SCA optic. A 2.5 µm SCA optic was employed with a

beamsize of approximately 2 μm × 2 μm, thus forming an approximate probing volume with axes 2.5, 2 and 1.5 μm. This configuration resulted in approximately 3-fold improvement in the depth resolution (2.5 μm in place of 7 μm) compared to the previous SCA based configuration. Additionally, here the employed pixel size was 2.5 μm × 2.5 μm, which is comparable to the dimension of bone microstructures such as cement lines. This is an important aspect of this configuration as it allows improved accuracy in predicting the association between observed intensities and bone microstructures. Superior resolution maps showing excellent details of bone microstructures and lacunae (cellular spaces) demonstrate the advantage of the present CXFI configuration. Lacunae are clearly visible in most parts of the Sr and Ca maps, however not in the Pb map, which may be due to the deposition of Pb in those structures. The Sr map observed here shows interesting concentric intensity bands across the radii of osteons. This could be possible due to a change in diet or wellness over the duration of osteon formation. The mean formation time for a cortical osteon has been found to increase from 46 days at 10 years of age to 108 days at 60 years of age,[32] hence the Sr profile observed here may be reflecting a change in diet over a period of approximately two and a half months given the age of the individual in the present case is approximated as 40-45 years. Since the sample reported here is from a naval cemetery, a change in diet associated to travel is highly probable. With regard to Ca map, the intensity variation observed across the map here is least compared to its previous counterparts. This is likely due to the least variation in the distances between the sample surface and confocal plane as a function of spatial locations. Since this map is smallest in size, the least variation is expected. As observed in panel C, the appearance of lacunae in this panel (panel D) is also similar in both Sr and Ca maps, which suggests a similar spatial resolution in both maps. Here lacunae are of 4-6 pixels: the spatial resolution along the horizontal axis of the map is doubled compared to panel C, as expected.

6.6.2 Pb speciation using SCA (2.5 μm) based CXAS

In a CXFI arrangement, the created probe volume can also be used in performing three dimensionally resolved X-ray absorption spectroscopic measurements in order to determine localized elemental speciation information within a sample. To date, there are at least four instances of polycapillary based CXAS[30,33–35] and one occurrence of SCA based CXAS[25] in the

literature. However, the highest spatial resolution offered by a commercially available polycapillary optic is limited to approximately 8 μm,[22] and the previous SCA based CXAS reported a resolution of approximately 7 μm. The novelty of the experiment reported herein lies in the application of a SCA optic of 2.5 μm resolution in CXAS, which allowed probing a volume as small as approximately 2 μm × 2.5 μm × 1.5 μm.

The imaging study presented above has shown an indication of diagenetic Pb in the sample surface. This experiment attempted to test the hypothesis that the chemical form of Pb may be different depending on the type of uptake. Taking advantage of the superior resolution of SCA based CXAS, the species of Pb was examined by exploiting the Pb L_3-edge CXAS at selected volume elements of interest in specific locations within sample. Figure 6.4 shows the obtained results. The locations *a*, *b*, and *c* respectively correspond to the sample surface, cement line and canal wall features, which were chosen from the map shown in the inset. Since the spatial resolution employed in this experiment is comparable to the width of a cement line or canal wall (approximately 2 μm), the collected spectra should reflect a close correspondence with the features. Comparison among the spectra shows that while the spectra from *b* and *c* are fairly alike, the spectrum corresponding to *a* is different from *b* and *c*. In particular, a broad peak at around 13,083 eV in spectrum *a* is absent from *b* and *c*. Since the difference in spectra is a manifestation of the different chemical environments of Pb at the studied locations,[30,35] it can be inferred that the difference observed in *a* is indicative of a different Pb-chemical form at the sample surface. Since the surface was exposed to the burial environment, it is likely to pose a higher risk of diagenesis compared to the shielded inner bone structures. Or alternatively, this could be biogenic Pb but subjected to a different chemical environment post interment, leading to different chemical transformations. Interestingly, the results for inner locations, *b* and *c*, show a similar Pb chemical form, while the difference is observed in location *a*, which is outer surface.

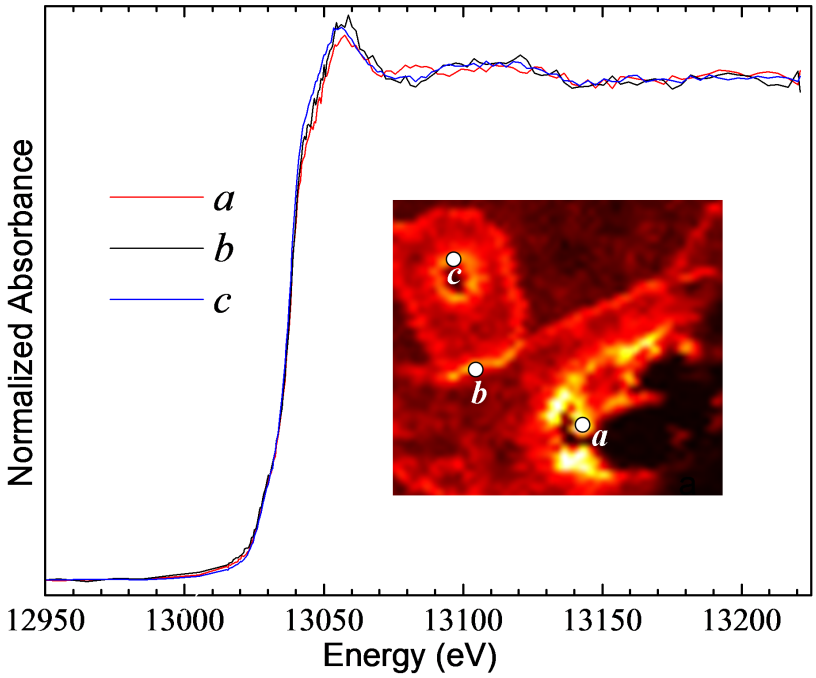

Figure 6.4 Pb L_3-edge CXAS spectra collected from an archaeological human bone sample. Spectra from three locations (a, b, and c) within the sample presented in panels B, C and D in Figure 6.3 are presented. The locations a, b, and c respectively correspond to sample surface, cement line and canal wall; chosen according to the map shown in the inset. Each spectrum was collected from a voxel dimension of approximately 2 µm × 2.5 µm × 1.5 µm.

A common method for identifying an unknown XAS spectrum is to compare the spectrum with a library of standard XAS spectra.[35] Figure 6.5 shows such an effort, in which the experimental Pb CXAS spectra from *a*, *b* and *c* are compared with Pb XAS from some standard Pb compounds. While no identical fingerprinting is observed between the bone data and shown standards, some similarity of *b* and *c* are visible with PbO. The absence of similarity with shown standards implies that the Pb species in bone spectra are not well represented by these specific standard Pb chemical forms. An extension of this analysis by including more standards is needed to elucidate the chemical forms of Pb in measured bone CXAS.

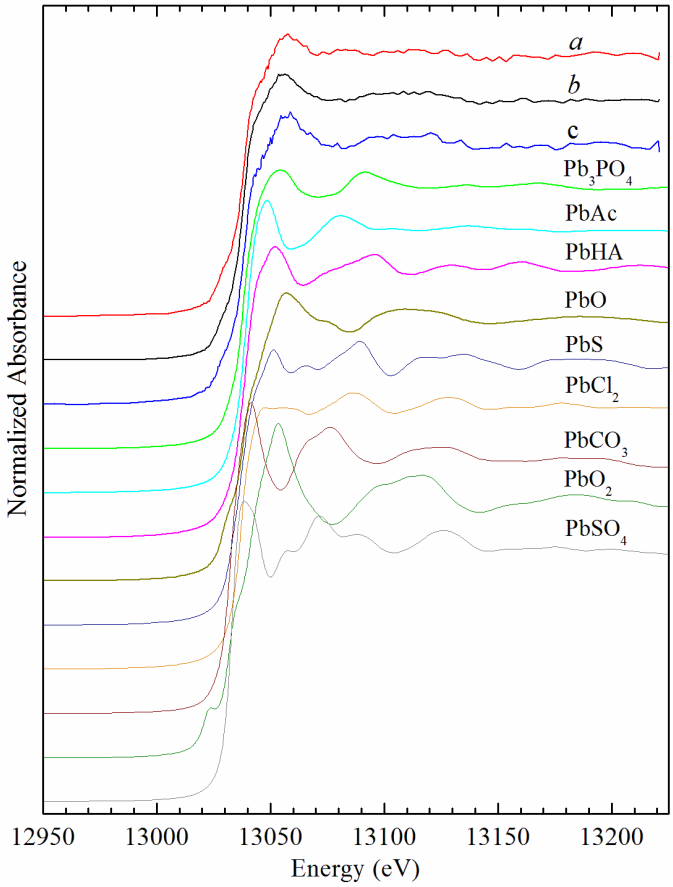

Figure 6.5 Comparison of Pb L_3-edge XAS spectra measured from bone with some standard Pb species. Bone spectra (a, b and c from Figure 6.4) are collected using confocal mode, and standards are measured using bulk XAS. PbHA: Pb Hydroxyapatite and PbAc: Pb Acetate.

6.6.3 Rationale for the presence of Ca, Pb and Sr in bone

The presence of Ca in bone is well understood as it is one of the main constituents of hydroxyapatite, the bone mineral.[36] Ca is generally expected to be present everywhere in the bone matrix and therefore, a Ca-map is viewed as a way of visualizing some bone micro structures such as osteonal canal, lacunae and outer boundary of a sample. For instance, the Ca-maps in Figure 6.3 show mapped areas with periosteal surfaces, the locations of osteons and lacunae. Unlike Ca, Pb and Sr are non-essential for bone; these elements get deposited in bone following biochemical mechanisms when exposure to these elements occurs during life through diet, occupation or other constituents of lifestyle. While neither has any known benefiting role to

health, Pb is known as a potential toxin. Studies have suggested that Pb^{2+} is competitive with Ca^{2+} ions,[37] and capable of occupying Ca^{2+} sites in the hydroxyapatite.[38] A recent confocal X-ray fluorescence study,[31] which demonstrated similar Pb distributions to those presented herein, suggested that the higher Pb intensity in the cement lines and canal walls compared to the adjacent mineralized bone matrix may likely be due to non-collagenous proteins like osteocalcin and osteopontin, which are higher in the cement lines and canal walls in comparison with the mineralized bone matrix.[39] Particularly, the higher affinity of osteocalcin for Pb compared to Ca may be responsible for the higher concentrations of Pb in these regions.[31] It is reasonable to think that the canal walls (also cement lines) accumulate Pb ions through their exposure to the interstitial fluid when the new bone matrix is deposited in the cement line materials (proteins and mineral).[31] Like Pb, Sr has been also known to replace Ca in the crystal lattice of the bone hydroxyapatite by ionic substitution.[40] While, our data show some similarities between the localization of Pb and Sr, some variation is also evident. This suggests a need for further studies to understand the uptake mechanism of Sr in bone.

6.6.4 Biogenicity versus diagenesis

Biogenicity implies uptake during life whereas diagenesis means molecular alteration of skeletal materials after interment. While biogenic elements are of interest in bioarchaeology, diagenesis is often a problem as it is difficult to differentiate between the two. This study attempted testing if the high resolution CXFI and CXAS can be useful in differentiating between biogenicity and diagenesis.

CXFI elemental maps showing details of the association between elements and microstructures may be advantageous to differentiate between the two types of uptakes. We see that the analysis of the results does, in fact, show some compelling evidences of biogenic uptake. The distributions of Pb showed a systematic pattern in the map, such as generally exhibiting higher intensities in the cement lines and canal walls. We speculate that this would not have been this way if the uptake was diagenetic; rather, a random presence of Pb in canals and throughout the sample would be expected. A further evidence of the biogenicity of Pb lies in the illustration of few canal walls showing almost no Pb accumulation while most canal walls do. We speculate that if diagenesis was the underlying reason of Pb accumulation, a distance of approximately 250

microns (approximate spacing between two osteons) is too short to exhibit any noticeable difference in Pb accumulation. Furthermore, the enrichment of at least one osteon with Pb combined with the presence of Pb within canal may be suggestive of high Pb levels in blood for about two months preceding death. On the other hand, the appearance of a high intensity Pb layer on the periosteal surface looks suspicious for biogenicity, thus may be suggestive of diagenesis as it is observed all over the surface which was exposed to the burial environment. Similar to Pb, the Sr also displays certain patterning in its localization within bone microstructures. The presence of high Sr in some osteons while others show very low levels is suggestive of biogenicity. In addition, the observation of intensity bands throughout the osteons likely manifest systematic biological processes as underlying reasons, not just a random diffusion from the burial environment.

The Pb chemical forms are likely to be different depending on the type of uptake: biogenic or diagenetic. SCA based CXAS enables probing highly localized bone microstructure specific Pb chemical form, thus can be advantageous in differentiating between the two. Strikingly, our CXAS result agrees with CXFI in indicating diagenesis of Pb at the sample surface. While more data and further studies are needed for the confirmation of results, this paper provides an initial demonstration of the potential of combining high resolution CXFI and CXAS as a successful strategy to differentiate elemental diagenesis from its biogenic counterparts.

6.7 Conclusions

This study demonstrated the first report of the implementation of novel high resolution SCA optics for biological CXFI and CXAS. The results illustrated the advantage of employing this optic in achieving a superior spatial resolution, approaching 2 microns, in confocal X-ray fluorescence mapping and absorption spectroscopy of elements. Unlike traditional polycapillary optics, the SCA optics have demonstrated an equivalent spatial resolution for a low energy element, Ca - a manifestation of the nearly energy independent nature of SCA optics. The SCA optics therefore can enhance the current capability of confocal imaging and spectroscopy.

While the analysis of bone data showed some indication of biogenesis, an extended study employing more samples from the same cemetery and other burial conditions such as from the

Arctic where diagenesis is unlikely to happen, is suggested for the confirmation of the nature of Pb in samples. The mapping of a larger area would be valuable as it will allow the examination of many osteons and the pattern of Pb localization. Improved statistics in a given spectrum, and more observations of spectra at different locations are also required in Pb CXAS to confirm the difference in Pb chemical form observed at the sample surface. A combined approach using both polycapillary and SCA based CXFI may be useful for large area and high resolution mapping.

Different modes of X-ray fluorescence imaging were presented in the mapping of elements and it is important to be aware that each of them has their own advantages and disadvantages. A decision about choosing a certain mode for a specific experiment will depend on a number of factors such as the required spatial resolution, necessity of sample cooling, required map size and available synchrotron beamtime. Conventional XFI may be sufficient if optical sectioning does not bring any advantage to the experiment and some background noise is acceptable. Polycapillary based CXFI is appropriate as long as a resolution smaller than approximately 8 μm is not a requirement. Although a high resolution SCA optic allows a resolution approaching 2 μm; these optics may restrict the use of certain samples such as those with a rough surface or requiring a cooling stage due to the shorter working distance. Also, the intensity counts obtained from a confocal volume using a SCA optic are likely to offer less efficiency compared to a polycapillary due to several SCA design restrictions, such as i) smaller vertical collection solid angle, ii) fluorescence striking the channel pillars being blocked from being transmitted to the detector and iii) if the distance between the optic and detector is big then some fluorescence transmitted through the channels may be too divergent to reach the detector. The long measuring time required for high resolution measurements could also be a limiting factor for some applications requiring large area mapping as access to synchrotron beamtime is limited.

6.8 Acknowledgements

This research was supported by a Social Sciences and Humanities Research Council (SSHRC) Insight Development Grant (#430-2012-0236), by NSERC Discovery Grants (to GNG and IJP), and by the Canada Foundation for Innovation through funding for BioXAS: Life Science Beamline for X-ray Absorption Spectroscopy at the Canadian Light Source Inc. SC is a

fellow in the Canadian Institutes of Health Research Training grant in Health Research Using Synchrotron Techniques (CIHR-THRUST, IJP and others). GNG, IJP and DMLC are Canada Research Chairs. Sector 20 facilities at the Advanced Photon Source, and research at these facilities, are supported by the US Department of Energy - Basic Energy Sciences, the Canadian Light Source and its funding partners, the University of Washington, and the Advanced Photon Source. Use of the Advanced Photon Source, an Office of Science User Facility operated for the U.S. Department of Energy (DOE) Office of Science by Argonne National Laboratory, was supported by the U.S. DOE under Contract No. DE-AC02-06CH11357. This work was performed in part at the Cornell NanoScale Facility, a member of the National Nanotechnology Infrastructure Network, which is supported by the National Science Foundation (Grant ECCS-0335765). This work is based upon research conducted at the Cornell High Energy Synchrotron Source (CHESS) which is supported by the National Science Foundation and the National Institutes of Health/National Institute of General Medical Sciences under NSF awards DMR-1332208 and DMR-0936384. Standards for spectroscopy were collected at the Stanford Synchrotron Radiation Lightsource (SSRL). Use of the SSRL, SLAC National Accelerator Laboratory, is supported by the U.S. Department of Energy, Office of Science, Office of Basic Energy Sciences under Contract No. DE-AC02-76SF00515. The SSRL Structural Molecular Biology Program is supported by the DOE Office of Biological and Environmental Research, and by the National Institutes of Health, National Institute of General Medical Sciences (including P41GM103393). The contents of this publication are solely the responsibility of the authors and do not necessarily represent the official views of NIGMS or NIH.

6.9 References

(1) Qin, Z.; Caruso, J. A.; Lai, B.; Matusch, A.; Becker, J. S. Trace metal imaging with high spatial resolution: applications in biomedicine. *Metallomics* **2011**, *3*, 28–37.

(2) Salt, D. E. Plant metallomics. *Metallomics* **2013**, *5*, 1088–1089.

(3) Outten, C. E.; Halloran, T. V. O. Femtomolar sensitivity of metalloregulatory proteins controlling zinc homeostasis. *Science* **2001**, *292*, 2488–2493.

(4) Swart, C.; Fisicaro, P.; Goenaga-Infante, H.; Zakel, S. Metalloproteins – a new challenge for metrology. *Metallomics* **2012**, *4*, 1137–1140.

(5) Waldron, K. J.; Robinson, N. J. How do bacterial cells ensure that metalloproteins get the correct metal? *Nat. Rev. Microbiol.* **2009**, *7*, 25–35.

(6) Lobinski, R.; Moulin, C.; Ortega, R. Imaging and speciation of trace elements in biological environment. *Biochimie* **2006**, *88*, 1591–1604.

(7) Fahrni, C. J. Biological applications of X-ray fluorescence microscopy: exploring the subcellular topography and speciation of transition metals. *Curr. Opin. Chem. Biol.* **2007**, *11*, 121–127.

(8) Pénicaut, B.; Bonnefoy, C.; Moesch, C.; Lachâtre, G. Inductively coupled plasma mass spectrometry. Perspectives in analysis and in biology. *Ann. Pharm. Fr.* **2006**, *64*, 312–327.

(9) Kikuchi, K.; Komatsu, K.; Nagano, T. Zinc sensing for cellular application. *Curr. Opin. Chem. Biol.* **2004**, *8*, 182–191.

(10) Yang, L.; Mcrae, R.; Henary, M. M.; Patel, R.; Lai, B.; Vogt, S.; Fahrni, C. J. Imaging of the intracellular topography of copper with a fluorescent sensor and by synchrotron X-ray fluorescence microscopy. *Proc. Natl . Acad. Sci . U. S. A.* **2005**, *102*, 11179–11184.

(11) Zeng, L.; Miller, E. W.; Pralle, A.; Isacoff, E. Y.; Chang, C. J. A selective turn-on fluorescent sensor for imaging copper in living cells. *J. Am. Chem. Soc.* **2006**, *128*, 10–11.

(12) Martin, J. L.; Stork, C. J.; Li, Y. V. Determining zinc with commonly used calcium and zinc fluorescent indicators, a question on calcium signals. *Cell Calcium* **2006**, *40*, 393–402.

(13) Pushie, M. J.; Pickering, I. J.; Korbas, M.; Hackett, M. J.; George, G. N. Elemental and chemically specific X-ray fluorescence imaging of biological systems. *Chem. Rev.* **2014**, *114*, 8499–8541.

(14) Korbas, M.; Blechinger, S. R.; Krone, P. H.; Pickering, I. J.; George, G. N. Localizing organomercury uptake and accumulation in zebrafish larvae at the tissue and cellular level. *Proc. Natl . Acad. Sci . U. S. A.* **2008**, *105*, 12108–12112.

(15) Golosio, B.; Simionovici, A.; Somogyi, A.; Lemelle, L.; Chukalina, M.; Brunetti, A. Internal elemental microanalysis combining X-ray fluorescence, compton and transmission tomography. *J. Appl. Phys.* **2003**, *94*, 145–156.

(16) Lombi, E.; de Jonge, M. D.; Donner, E.; Kopittke, P. M.; Howard, D. L.; Kirkham, R.; Ryan, C. G.; Paterson, D. Fast X-ray fluorescence microtomography of hydrated biological samples. *PLoS One* **2011**, *6*, 1–5.

(17) Jonge, M. D. De; Holzner, C.; Baines, S. B.; Twining, B. S.; Ignatyev, K.; Diaz, J.; Howard, D. L.; Legnini, D.; Miceli, A.; Mcnulty, I.; Jacobsen, C. J.; Vogt, S. Quantitative 3D elemental microtomography of *Cyclotella meneghiniana* at 400-nm resolution. *Proc. Natl. Acad. Sci. U. S. A.* **2010**, *107*, 15676–15680.

(18) Janssens, K.; Proost, K.; Falkenberg, G. Confocal microscopic X-ray fluorescence at the HASYLAB microfocus beamline: characteristics and possibilities. *Spectrochim. Acta B* **2004**, *59*, 1637–1645.

(19) Woll, A. R.; Mass, J.; Bisulca, C.; Huang, R.; Bilderback, D. H.; Gruner, S.; Gao, N. Development of confocal X-ray fluorescence (XRF) microscopy at the Cornell high energy synchrotron source. *Appl. Phys. A* **2006**, *83*, 235–238.

(20) MacDonald, C. A. Focusing polycapillary optics and their applications. *X-Ray Opt. Instrum.* **2010**, *2010*, 1–17.

(21) *X-ray Spectrometry: Recent Technological Advances*; Kouichi, T., Injuk, J., Grieken, R. Van, Eds.; John Wiley & Sons, Ltd: West Sussex, England, 2004.

(22) XOS Polycapillary https://xos.com/wp-content/uploads/micro-xrf.pdf.

(23) Woll, A. R.; Agyeman-Budu, D.; Bilderback, D. H.; Dale, D. 3D X-ray fluorescence microscopy with 1.7 μm resolution using lithographically fabricated micro-channel arrays. *SPIE Opt. Photonics* **2012**, *8502*, 85020K – 1–85020K – 14.

(24) Woll, A. R.; Agyeman-Budu, D.; Choudhury, S.; Coulthard, I.; Finnefrock, A. C.; Gordon, R.; Hallin, E.; Mass, J. Lithographically-fabricated channel arrays for confocal X-ray fluorescence microscopy and XAFS. *J. Phys. Conf. Ser.* **2014**, *493*, 012028 (1–4).

(25) Choudhury, S.; Hormes, J.; Agyeman-Budu, D. N.; Woll, A. R.; George, G. N.; Coulthard, I.; Pickering, I. J. Application of a spoked channel array to confocal X-ray fluorescence imaging and X-ray absorption spectroscopy of medieval stained glass. *J. Anal. At. Spectrom.* **2015**, *30*, 759–766.

(26) Varney, T. L.; Swanston, T.; Cooper, D. M. L.; Graham, N.; Pickering, I. J.; Reginald, A. A preliminary investigation of lead poisoning in a Napoleonic era Naval Cemetery in Antigua , W . I . *Caribb. Connect. A Publ. F. Res. Cent. 2(1) Spec. Issue Focus. Bioarchaeology Caribbean.* **2012**, *II* (1).

(27) Swanston, T.; Varney, T.; Coulthard, I.; Feng, R.; Bewer, B.; Murphy, R.; Hennig, C.; Cooper, D. Element localization in archaeological bone using synchrotron radiation X-ray fluorescence: identification of biogenic uptake. *J. Archaeol. Sci.* **2012**, *39*, 2409–2413.

(28) Swanston, T.; Varney, T.; Coulthard, I.; George, G. N.; Pickering, I. J.; Murphy, R.; Cooper, D. M. L. Synchrotron X-ray fluorescence imaging evidence of biogenic mercury identified in a burial in colonial Antigua. *J. Archaeol. Sci.* **2015**, *58*, 26–30.

(29) Heald, S.; Stern, E.; Brewe, D.; Gordon, R.; Crozier, D.; Jiang, D.; Cross, J. XAFS at the Pacific Northwest Consortium-Collaborative Access Team undulator beamline. *J. Synchrotron Rad.* **2001**, *8*, 342–344.

(30) Silversmit, G.; Vekemans, B.; Nikitenko, S.; Schmitz, S.; Schoonjans, T.; Brenker, F. E.; Vincze, L. Spatially resolved 3D micro-XANES by a confocal detection scheme. *Phys. Chem. Chem. Phys.* **2010**, *12*, 5653–5659.

(31) Pemmer, B.; Roschger, A.; Wastl, A.; Hofstaetter, J. G.; Wobrauschek, P.; Simon, R.; Thaler, H. W.; Roschger, P.; Klaushofer, K.; Streli, C. Spatial distribution of the trace elements zinc, strontium and lead in human bone tissue. *Bone* **2013**, *57*, 184–193.

(32) Lips, P.; Courpron, P.; Meunier, P. J. Mean wall thickness of trabecular bone packets in the human iliac crest: changes with age. *Calcif. Tiss. Res.* **1978**, *26*, 13–17.

(33) Wilke, M.; Appel, K.; Vincze, L.; Schmidt, C.; Borchert, M.; Pascarelli, S. A confocal set-up for micro-XRF and XAFS experiments using diamond-anvil cells. *J. Synchrotron Radiat.* **2010**, *17*, 669–675.

(34) Reiche, I.; Röhrs, S.; Salomon, J.; Kanngießer, B.; Höhn, Y.; Malzer, W.; Voigt, F. Development of a nondestructive method for underglaze painted tiles-demonstrated by the analysis of Persian objects from the nineteenth century. *Anal. Bioanal. Chem.* **2009**, *393*, 1025–1041.

(35) Meirer, F.; Pemmer, B.; Pepponi, G.; Zoeger, N.; Wobrauschek, P.; Sprio, S.; Tampieri, A.; Goettlicher, J.; Steininger, R.; Mangold, S.; Roschger P.; Berzlanovich A.; Hofstaetter J. G.; Streli C. Assessment of chemical species of lead accumulated in tidemarks of human articular cartilage by X-ray absorption near-edge structure analysis. *J. Synchrotron Rad.* **2011**, *18*, 238–244.

(36) Anthony Mescher. *Junqueira's Basic Histology: Text and Atlas*, 13th ed.; The McGraw-Hill Companies, 2013.

(37) Büsselberg, D.; Evans, M. L.; Rahmann, H.; Carpenter, D. O. Lead and zinc block a voltage-activated calcium channel of Aplysia neurons. *J. Neurophysiol.* **1991**, *65*, 786–795.

(38) Pounds, J. G.; Long, G. J.; Rosen, J. F. Cellular and molecular toxicity of lead in bone. *Environ. Heal. Perspect.* **1991**, *91*, 17–32.

(39) Skedros, J. G.; Holmes, J. L.; Vajda, E. G.; Bloebaum, R. D. Cement lines of secondary osteons in human bone are not mineral-deficient: New data in a historical perspective. *Anat. Rec. A Discov. Mol. Cell. Evol. Biol.* **2005**, *286A*, 781–803.

(40) Li, C.; Paris, O.; Siegel, S.; Roschger, P.; Paschalis, E. P.; Klaushofer, K.; Fratzl, P. Strontium is incorporated into mineral crystals only in newly formed bone during strontium ranelate treatment. *J. Bone Miner. Res.* **2010**, *25*, 968–975.

Chapter 7. Discussion and Conclusions

7.1 Linking the Goal and Findings

The unique properties of CXFI[1–6] and CXAS[7–9] offer tremendous potential and new opportunities for scientific exploration in a variety of disciplines (chapter 1). Research with biological samples can particularly benefit from these techniques since the confocal method allows measurement of intact (unthinned or unstained) samples for determination of elemental distribution or speciation. On the other hand, most biological samples are generally better candidates for confocal X-ray fluorescence investigation due to greater achievable probe depth. Since a biological sample matrix is usually comprised of light elements with low X-ray absorption cross sections with a concomitantly low density, they allow probing a greater depth compared to their inorganic counterparts. Although there is potential, both CXFI and CXAS techniques are relatively new and still underutilized in biological research. The fundamental principle of the confocal method requires restricting the detector's field of view by employing an additional detection focusing optic in a microprobe setup to the focal spot of the optic. A polycapillary[10,11] is the traditionally used detection focusing optic for the construction of a confocal X-ray fluorescence geometry. While highly suitable, a polycapillary limits the achievable value of spatial resolution (up to 10 – 12 μm or greater at 10 keV) and also gives rise to spatial resolution that is inversely proportional to energy.[8,12] Recently a new detection focusing optic, SCA,[8,12] has been proposed for achieving higher spatial resolutions (in the scale of ~2 μm) even for light elements (2 - 5 keV). Such improvement in spatial resolution has made confocal X-ray fluorescence techniques even more suitable for biological applications since biological systems often involve light elements and micron scale inhomogenity. This thesis, therefore, aimed at developing the confocal techniques, CXFI and CXAS, for biological applications, with a long term goal of implementing the instrumentation at the BioXAS beamline at CLS.

The 20ID-B beamline at APS,[13,14] a beamline of Canadian partnership, was used as the main venue for this research, since 20ID-B offered all the required capabilities while the BioXAS beamline at the CLS was under construction during this project and therefore unavailable for testing. The G-line at CHESS synchrotron was also used once for a special purpose. Chapter 2 gives an account of how CXFI and CXAS were initiated and developed at 20ID-B through a number of test experiments in which both types of detection optics mentioned above, the traditional polycapillary and novel SCA optics, were employed in investigating a variety of systems. For the purpose of discussion, the complete technique development project is divided into two parts, the polycapillary- and SCA-based studies.

Polycapillary based CXFI and CXAS: Polycapillary optic based confocal X-ray fluorescence configurations were employed in the starting phase of the project. It was logical to start with the traditional polycapillary optics, since the beginning of this project in fact initiated the confocal capability at 20ID-B beamline. Section 2.3.1.1 described the first confocal setup constructed at the beamline 20ID-B. The first test experiment reported in this section studied Hg distribution in the eye of a zebrafish larva exposed to organic Hg. While a number of depth selective elemental maps through the eye were collected successfully, some irradiation effects such as browning and slight melting of the sample were problematic in the experiment, suggesting the need for a sample cooling system. It is worth noting that the irradiation effects in confocal experiments are significant since the same paths through a sample are irradiated multiple times during the collection of a number of depth selective two dimensional maps. The requirement of a sample cooling system was also evident in the measurements of mouse brain sections at beamlines 20ID-B, APS and G-line, CHESS (sections 2.3.1.3 and 2.3.2.1) in which drying and tearing of samples also occurred. While almost all experiments in this thesis were performed at 20ID-B, the G-line, CHESS was once used to utilize a bigger beam spot size of ~ 25 μm, which is relevant for measuring bigger biological samples. In order to overcome the irradiation effects, a sample cooling system, based on a Linkam stage and utilizing liquid nitrogen, was employed in the setup of 20ID-B (section 2.3.1.2). However, achieving a stable cooling system required applying some improvements through the implementation of a better quality transfer line and bigger dewar to the initial system (section 2.3.1.4).

The study exploiting the first stable CXFI setup developed at 20ID-B investigated the effect of embryonic exposure to elevated selenium in intact zebrafish larva. The detail of experiments and findings can be found in chapter 3 and has also been published.[15] Maternal transfer of selenium is an important route of selenium exposure for fish in the natural environment. The study intended to determine tissue specific spatial distribution and speciation of maternally transferred selenium in the early developmental stage of life using CXFI and CXAS in an intact larva. Strikingly, the CXFI revealed a preferential accumulation of selenium in the eye lens. The reported CXAS data, which marked the first published biological CXAS, suggested the speciation of selenium within the eye lens of intact larva to be a selenomethionine-like species. It was hypothesized that the preferential accumulation of Se in the eye lens is likely due to the substitution of Se for the naturally occurring sulfur in the eye lens. As selenomethionine readily replaces methionine,[16] it was thought that the chemical form of selenium in the eye lens is highly likely to be selenomethionine-like species, as determined in CXAS. Interestingly, a literature search following this observation uncovered previous reports of ocular impairments in fish inhabiting selenium elevated water.[17–19] The study suggested that there may be a relationship between the exposure to elevated selenium and reported ocular impairments. While studying this scientific question, this study also has demonstrated the practicality and usefulness of the first confocal setup at 20ID-B in investigating the trace element distribution and speciation in an intact biological specimen.

The first confocal setup at 20ID-B was then employed to measure high resolution elemental maps from poorly preserved archaeological human bone samples, for which thin sectioning and consequently, conventional XFI was impractical. The detail of this study is reported in chapter 4 and a manuscript has been accepted.[20] While the study described in the previous paragraph benefitted from the confocal method by employing an intact sample to maintain the sample integrity, the use of confocal in this study was intended to enable measurement of a fragile sample, which is impractical for thin (micron scale) sectioning and hence unrealistic for best spatial resolution results using conventional XFI. This work demonstrated the value of CXFI as a tool for generating high resolution elemental maps from a fragile archaeological bone sample showing excellent details of elemental incorporation into bone microstructures.

SCA based CXFI and CXAS: The implementation of novel SCA optic in the confocal setup at 20ID-B was considered as the next logical step. While the use of a polycapillary optic as a confocal detection optic is utilized in all known previously demonstrated experiments, the SCA optics are first demonstrated in experiments reported in this thesis. The implementation of SCA optics as an alternative to polycapillary was primarily intended to achieve higher spatial resolutions in elemental mapping and speciation obtained by CXFI and CXAS. The use of polycapillary optics imposes two limitations in confocal experiments: firstly, the highest achievable resolution is approximately 10 - 12 µm or greater at 10 keV;[8,12] and secondly, the resolution deteriorates with decreasing X-ray energy (from 10 to ~ 40 µm as X-ray energy vary from 12 down to 3 keV).[4,5,21,22] In contrast, SCA optics are nearly achromatic, enabling ~2 µm resolution operation;[8,12] hence an important tool for CXFI especially when resolution superior to polycapillary is required. While SCA is applicable in most cases, some restrictions with regard to the sample type and cooling system may be applied due to the limited working distance and collection efficiency (section 2.2.3).

The first CXFI experiment at 20ID-B that employed a SCA optic was primarily intended to test the feasibility of the optic. The detail of this study is reported in chapter 5 and is published.[23] The experiment studied an inorganic type sample, a medieval stained glass, obtained from 13th Century Paderborn Cathedral, Germany. This sample was chosen due to the relatively high elemental concentrations. Three dimensional distributions of Fe, Ca and Mn, and the localized chemical form of Fe were measured in the intact corrosion layer of the sample. Implementation of the SCA optic enabled superior resolution depth selectivity in the intact corrosion layer and measurement of elemental distribution and speciation in a highly localized manner within the layer. The results showed that both the composition and the chemical form vary as a function of three dimensional locations in the corrosion layer. While demonstrating the potential of implementing SCA based confocal techniques in the study of corrosion layers, this work demonstrated the first implementation of SCA based CXFI and CXAS at 20ID-B.

As a next step, the SCA based confocal setup at 20ID-B was applied in studying biological samples. An archaeological human bone sample was studied using confocal X-ray fluorescence configurations with SCA optics of varied resolutions. The detail of this study is

reported in chapter 6. This chapter presents CXFI elemental maps of unprecedented resolution and highly localized CXAS spectroscopic data in bone. Several recent studies of human bone employing CXFI in conjunction with quantitative backscattered electron imaging (qBEI)[24–26] explicitly noted that the comparatively poor spatial resolution of CXFI prevented the images from two different techniques to be overlaid precisely, and obscured the degree of variation in elemental concentrations among different bone microstructures. The measurements described in chapter 6 presented superior resolution maps, obtained using the 2.5 μm SCA optic, showing excellent details of bone microstructures and lacunae (cellular spaces). The results allowed improved accuracy in predicting the association between observed intensities and bone microstructures. Besides demonstrating the practical utility and benefit of employing SCA optics in elemental imaging and speciation within bone, Chapter 6 also served to shed light in answering the question, whether the observed Pb is biogenic (uptake when alive) or diagenetic (postmortem contamination). Although more statistics are required for confirmation, the observed variation in the Pb intensities among canal walls, cement lines and osteonal canals; and Pb speciation data among canal wall, cement line and periosteal surface indicated a biogenic uptake of Pb. It was speculated in the chapter that confocal X-ray fluorescence techniques, CXFI and CXAS, can be applied as important tools in determining the nature of Pb. The knowledge with regard to the origin of Pb eventually may aid in answering the historical question: whether lead poisoning played a role in the demise of the British military in colonial Antigua, West Indies.

To conclude, this thesis successfully included the confocal capability in elemental imaging and speciation offered at the 20ID-B beamline. This beamline now accepts user proposals requesting CXFI and CXAS experiments. The superior resolutions obtained by the implementation of SCA optics have potential to significantly broaden the range of application of confocal X-ray fluorescence techniques. While polycapillary still remains the predominant means of performing confocal X-ray fluorescence experiments, the SCA optic serves as an important addition to the toolkit when superior spatial resolution results (< 10 μm) are required. It is expected that the confocal X-ray fluorescence capabilities studied in this thesis will be implemented at the BioXAS imaging beamline at the CLS in near future.

7.2 Recommendations for Future Research

While the development of confocal X-ray fluorescence techniques was the primary focus of this thesis, several scientific questions were also studied along the way as reported in chapters 3 - 6. To discuss the future directions of this research, this section is divided into two parts: one focused to the studied scientific cases, and other focused to the technique development.

7.2.1 Future research related to the scientific cases studied

1. *Selenium in zebrafish:* The effect of maternal transfer of Se is investigated and reported in chapter 3. When compared to fish on a control diet the study found that although Se is widely distributed in the larval body, the highest level is present within the eye lens. This observation is of importance in understanding possible Se-related ocular impairments; however, the preferential accumulation in the eye lens needs to be supported by better statistics. Therefore, a large scale future study including more larvae may be suggested for improved understanding. This study also found that the chemical form of Se in the eye lens is selenomethionine; however, this was obtained based on the CXAS data collected from only a single hot spot of Se. More CXAS data from other locations at the eye lens are needed for the confirmation. In an effort to explain Se-related cataract, this study hypothesized that the opacification of the eye lens or cataract likely occurs from the oxidation of selenomethionine, which disrupts the strictly organized structure of the eye lens protein, crystallin. This hypothesis can be tested in a future study investigating the chemical form of Se in a cataract affected fish eye lens collected from a high selenium water area. In another extension, comparing the toxicity of various chemical forms of selenium through different routes of exposure such as diet or water may be of interest.[27]

2. *Antique stained glass:* Antique stained glass sample obtained from 13th century Paderborn Cathedral, Germany is investigated and reported in chapter 5. The study attempted determining the composition and chemical form of metals in the corrosion layer of the sample. It was observed that both the composition and the chemical form vary as a function of three dimensional locations in the corrosion layer, however only a small area of a single specimen was studied. Future larger scale studies of mapping and speciation in additional related specimens

and using higher resolution SCA optics will provide valuable information to understand the process of corrosion.

3. *Archeological bone:* Archaeological bone samples excavated from the Royal Naval Hospital Cemetery (c. A.D. 1793-1822), Antigua were studied in chapters 4 and 6. A key historical question related to this population was whether Pb poisoning played a role in the demise of the British military in West Indies, and whether the observed Pb was biogenic (deposited during life) or diagenetic (postmortem contamination). Although the Pb elemental maps and speciation data presented in those chapters have shown indication of Pb being biogenic, additional mapping and speciation data are necessary to confirm the understanding of the nature of Pb. This study could be expanded in several directions, such as by employing more specimens of the same or other individuals, and different burial environments.

7.2.2 Future technique development

1. *Improved depth resolution*: The depth resolution in confocal X-ray fluorescence techniques is determined by the focal spot of the detection focusing optic. In contrast to polycapillaries, the novel SCA optics are nearly achromatic, enabling ~2 μm resolution operation. While the SCA optics have demonstrated improvement in depth resolution, there may be possibilities of achieving a further improvement when optics are fabricated from materials other than silicon or germanium. A simulation designed for SCA optics has indicated that it should be possible to make channel arrays having channel widths of 0.5 μm by using gold (see appendix), possibly through electrodeposition.

2. *Smaller incident beam*: The dimensions (X, Y, and Z) of a probe volume in a confocal X-ray fluorescence experiment is determined by the sizes of the incident beam and focal spot of the detection focusing optic. The use of an incident beamsize smaller than ~ 2 μm × 2 μm, the smallest employed in this thesis (chapter 6), should improve spatial resolutions along two dimensions (say, X and Y), regardless of the focal spot size of the detection focusing optic (Z). While such configuration can not be applied to any general scenario, it may be worth applying in circumstances when a higher resolution is required for a sample plane (XY), however the

variation in sample features along the perpendicular direction (say, Z) can be viewed by employing the resolution available from the detection focusing optic.

3. *Larger working distance of SCA optics*: The shorter working distance (only up to 1.5 mm) of SCA based confocal configurations represent a limitation of the technique. This limitation restricts the use of sample cooling stages or samples with rough surfaces due to the space limitation between the tip of the optic and the confocal volume. An improved SCA design, in which collimating channels were formed by the staggered arrays of pillars, showed an improved working distance of ~ 1.5 mm.[8] A further improvement to the working distance of SCA optics may be possible, in which a higher SCA depth can be obtained by implementing synchrotron based lithography, for which an improved aspect ratio compared to DRIE could be obtained.[8]

4. *Increased collection solid angle for SCA optics*: Section 2.2.3 discussed the weaker performance of a SCA optic compared to a polycapillary with regard to the collection of the amount of fluorescence from a volume element. This is because the vertical collection solid angle for a SCA optic is smaller than a polycapillary of similar resolution. This vertical collection angle is determined by the channel's depth, which is limited by the typical aspect ratios for deep reactive ion etching (DRIE).[8] Implementation of synchrotron based lithography in fabricating optics may allow deeper channels.

5. *Improved count rate by vertical stacking of the devices*: Biological samples are often dilute, hence an improved count rate will significantly contribute to the success of an experiment. It can be hypothesized that employing a slightly complex setup, in which a number of detection focusing optics vertically stacked on a holder, all focused to a single confocal volume will significantly increase the count rate in an experiment. This idea can be applied in both polycapillary or SCA based setup, although it may be easier with SCA optics due to their compact size.

6. *Creating cryogenic sample environment*: Cryogenic conditions were proved to be vital for many biological samples (chapter 2). A Linkam THMS600 cooling stage, which received a

constant liquid nitrogen flow, was used in this research; however applying this cooling system in a SCA based setup is impractical due to the shorter working distance of the optic. Although other means of sample cooling, such as the implementation of a cryogenic gas (N2) stream or cold finger may be helpful, these may cause vibration of the optical system or frosting of the sample. The implementation of a cryostream or cold finger have not been tested in this thesis, hence future experiments testing the feasibility of these cooling techniques would be valuable.

7. *Quantification*: CXFI has been employed to analyze samples of different origin, such as pigment layers in art objects or elemental distributions in biological and environmental samples. The desire of quantifying elements at spatial locations of interest within samples lead to several reports,[5,22,28–31] in which only a couple[22,30] dealt with biological samples. The quantification of CXFI data is relatively less straightforward compared to conventional XFI as the calculations in CXFI require detailed knowledge of the absorption of both the incoming and detected beams, spatial form of the probe volume, and sample matrix. In case of SCA based CXFI, the calculations would face one less complication as the SCA derived probe volume is nearly energy independent, unlike the polycapillary optics. It may be possible to extend the method suggested by B. De Sambar *et. al.*[22] to use the K_α to K_β peak ratios of all elements to predict the degree of attenuation of fluorescence for all elements. This may be applied to the quantification of CXFI data from biological samples.

7.3 Conclusion

This thesis facilitated establishing confocal capability in the X-ray fluorescence detection at beamline 20ID-B, APS. Two confocal setups, based on two types of detection side X-ray focusing optics; the polycapillary and novel SCA, were developed. For both configurations, K-B mirror pairs were used to achieve the focusing of incident X-rays. The introduction of confocal detection capability enhances beamline competence by enabling important advantages such as localized X-ray fluorescence analysis of microscopic sub-volumes within a larger sample (limited by the escape depth of emitted X-ray fluorescence), and improved signal to noise ratio through a superior scatter reduction. This thesis successfully implemented novel SCA optics as an additional confocal detection focusing optic. The reported results demonstrated that SCA optics can be the optics of interest when polycapillary derived spatial resolution is insufficient,

and these are capable of extending the scope of confocal X-ray fluorescence to resolutions approaching two microns even for light elements such as calcium. Future research enabled by the developments achieved in this thesis shows outstanding potential.

7.4 References

(1) Janssens, K.; Proost, K.; Falkenberg, G. Confocal microscopic X-ray fluorescence at the HASYLAB microfocus beamline: characteristics and possibilities. *Spectrochim. Acta B* **2004**, *59*, 1637–1645.

(2) Kanngießer, B.; Malzer, W.; Reiche, I. A new 3D micro X-ray fluorescence analysis set-up – First archaeometric applications. *Nucl. Instrum. Meth. B* **2003**, *211*, 259–264.

(3) Kanngießer, B.; Malzer, W.; Pagels, M.; Lühl, L.; Weseloh, G. Three-dimensional micro-XRF under cryogenic conditions: a pilot experiment for spatially resolved trace analysis in biological specimens. *Anal. Bioanal. Chem.* **2007**, *389*, 1171–1176.

(4) Vincze, L.; Vekemans, B.; Brenker, F. E.; Falkenberg, G.; Rickers, K.; Somogyi, A.; Kersten, M.; Adams, F. Three-dimensional trace element analysis by confocal X-ray microfluorescence imaging. *Anal. Chem.* **2004**, *76*, 6786–6791.

(5) Woll, A. R.; Mass, J.; Bisulca, C.; Huang, R.; Bilderback, D. H.; Gruner, S.; Gao, N. Development of confocal X-ray fluorescence (XRF) microscopy at the Cornell high energy synchrotron source. *Appl. Phys. A* **2006**, *83*, 235–238.

(6) Kanngießer, B.; Malzer, W.; Mantouvalou, I.; Sokaras, D.; Karydas, A. G. A deep view in cultural heritage—confocal micro X-ray spectroscopy for depth resolved elemental analysis. *Appl. Phys. A* **2012**, *106*, 325–338.

(7) Silversmit, G.; Vekemans, B.; Nikitenko, S.; Schmitz, S.; Schoonjans, T.; Brenker, F. E.; Vincze, L. Spatially resolved 3D micro-XANES by a confocal detection scheme. *Phys. Chem. Chem. Phys.* **2010**, *12*, 5653–5659.

(8) Woll, A. R.; Agyeman-Budu, D.; Choudhury, S.; Coulthard, I.; Finnefrock, A. C.; Gordon, R.; Hallin, E.; Mass, J. Lithographically-fabricated channel arrays for confocal X-ray fluorescence microscopy and XAFS. *J. Phys. Conf. Ser.* **2014**, *493*, 012028 (1–4).

(9) Wilke, M.; Appel, K.; Vincze, L.; Schmidt, C.; Borchert, M.; Pascarelli, S. A confocal set-up for micro-XRF and XAFS experiments using diamond-anvil cells. *J. Synchrotron Radiat.* **2010**, *17*, 669–675.

(10) Ding, X.; Gao, N.; Havrilla, G. Monolithic polycapillary X-ray optics engineered to meet a wide range of applications. *Proc. SPIE* **2000**, *4144*, 174.

(11) MacDonald, C. A. Focusing polycapillary optics and their applications. *X-Ray Opt. Instrum.* **2010**, *2010*, 1–17.

(12) Woll, A. R.; Agyeman-Budu, D.; Bilderback, D. H.; Dale, D. 3D X-ray fluorescence microscopy with 1.7 μm resolution using lithographically fabricated micro-channel arrays. *SPIE Opt. Photonics* **2012**, *8502*, 85020K – 1 – 85020K – 14.

(13) Heald, S. M.; Cross, J. O.; Brewe, D. L.; Gordon, R. A. The PNC/XOR X-ray microprobe station at APS sector 20. *Nucl. Instr. Meth. Phys. Res.* **2007**, *582*, 215–217.

(14) Heald, S.; Stern, E.; Brewe, D.; Gordon, R.; Crozier, D.; Jiang, D.; Cross, J. XAFS at the Pacific Northwest Consortium-Collaborative Access Team undulator beamline. *J. Synchrotron Rad.* **2001**, *8*, 342–344.

(15) Choudhury, S.; Thomas, J. K.; Sylvain, N. J.; Ponomarenko, O.; Gordon, R. A.; Heald, S. M.; Janz, D. M.; Krone, P. H.; Coulthard, I.; George, G. N.; et al. Selenium preferentially accumulates in the eye lens following embryonic exposure: A confocal X-ray fluorescence imaging study. *Environ. Sci. Technol.* **2015**, *49*, 2255–2261.

(16) Strub, M.-P.; Hoh, F.; Sanchez, J.-F.; Strub, J. M.; Böck, A.; Aumelas, A.; Dumas, C. Selenomethionine and selenocysteine double labeling strategy for crystallographic phasing. *Structure* **2003**, *11*, 1359–1367.

(17) Lemly, A. D. A teratogenic deformity index for evaluating impacts of selenium on fish populations. *Ecotox. Environ. Safe.* **1997**, *37*, 259–266.

(18) Lemly, A. D. Ecological basis for regulating aquatic emissions from the power industry: the case with selenium. *Regul. Toxicol. Pharm.* **1985**, *5*, 465–486.

(19) Lemly, A. D. Symptoms and implications of selenium toxicity in fish: the Belews lake case example. *Aquat. Toxicol.* **2002**, *57*, 39–49.

(20) Choudhury, S.; Swanston, T.; Varney, T.; Cooper, D. M. L.; George, G. N.; Pickering, I. J.; Vaughan, G.; Bewer, B.; Coulthard, I. Confocal X-ray fluorescence imaging facilitates high resolution elemental mapping in fragile archaeological bone. *Archaeometry* **2016**, In press, DOI: 10.1111/arcm.12232.

(21) Mihucz, V. G.; Silversmit, G.; Szalóki, I.; Samber, B. De; Schoonjans, T.; Tatár, E.; Vincze, L.; Virág, I.; Yao, J.; Záray, G. Removal of some elements from washed and cooked rice studied by inductively coupled plasma mass spectrometry and synchrotron based confocal micro-X-ray fluorescence. *Food Chem.* **2010**, *121*, 290–297.

(22) Samber De, B.; Silversmit, G.; Schamphelaere De, K.; Evens, R.; Schoonjans, T.; Vekemans, B.; Janssen, C.; Masschaele, B.; Hoorebeke Van, L.; Szalóki, I.; Vanhaecke, F.; Rickers, K.; Falkenberg, G.; Vincze, L. Element-to-tissue correlation in biological samples determined by three-dimensional X-ray imaging methods. *J. Anal. At. Spectrom.* **2010**, *25*, 544–553.

(23) Choudhury, S.; Hormes, J.; Agyeman-Budu, D. N.; Woll, A. R.; George, G. N.; Coulthard, I.; Pickering, I. J. Application of a spoked channel array to confocal X-ray fluorescence imaging and X-ray absorption spectroscopy of medieval stained glass. *J. Anal. At. Spectrom.* **2015**, *30*, 759–766.

(24) Pemmer, B.; Hofstaetter, J. G.; Meirer, F.; Smolek, S.; Wobrauschek, P.; Simon, R.; Fuchs, R. K.; Allen, M. R.; Condon, K. W.; Reinwald, S.; Phipps, R. J.; Burr, D. B.; Paschalis, E. P.; Klaushofer, K.; Streli, C.; Roschger, P. Increased strontium uptake in trabecular bone of ovariectomized calcium-deficient rats treated with strontium ranelate or strontium chloride. *J. Synchrotron Rad.* **2011**, *18*, 835–841.

(25) Roschger, A.; Hofstaetter, J. G.; Pemmer, B.; Zoeger, N.; Wobrauschek, P.; Falkenberg, G.; Simon, R.; Berzlanovich, A.; Thaler, H. W.; Roschger, P.; Klaushofer, K.; Streli, C. Differential accumulation of lead and zinc in double-tidemarks of articular cartilage. *Osteoarthr. Cart.* **2013**, *21*, 1707–1715.

(26) Pemmer, B.; Roschger, A.; Wastl, A.; Hofstaetter, J. G.; Wobrauschek, P.; Simon, R.; Thaler, H. W.; Roschger, P.; Klaushofer, K.; Streli, C. Spatial distribution of the trace elements zinc, strontium and lead in human bone tissue. *Bone* **2013**, *57*, 184–193.

(27) Dolgova, N.; Hackett, M.; MacDonald, T.; Nehzati, S.; James, A. K.; Krone, P. H.; George, G. N.; Pickering, I. J. Distribution of selenium in zebrafish larvae after exposure to organic and inorganic selenium forms. *Metallomics* **2016**, DOI: 10.1039/C5MT00279F, (In Press).

(28) Mantouvalou, I.; Malzer, W.; Kanngießer, B. Quantification for 3D micro X-ray fluorescence. *Spectrochim. Acta B* **2012**, *77*, 9–18.

(29) Malzer, W.; Kanngieβer, B. A model for the confocal volume of 3D micro X-ray fluorescence spectrometer. *Spectrochim. Acta B* **2005**, *60*, 1334–1341.

(30) Perez, R. D.; Sánchez, H. J.; Perez, C. A.; Rubio, M. Latest developments and opportunities for 3D analysis of biological samples by confocal μ-XRF. *Radiat. Phys. Chem.* **2010**, *79*, 195–200.

(31) Wrobel, P.; Czyzycki, M. Direct deconvolution approach for depth profiling of element concentrations in multi-layered materials by confocal micro-beam X-ray fluorescence spectrometry. *Talanta* **2013**, *113*, 62–67.

Appendix

Energy vs. SCA channel length plot

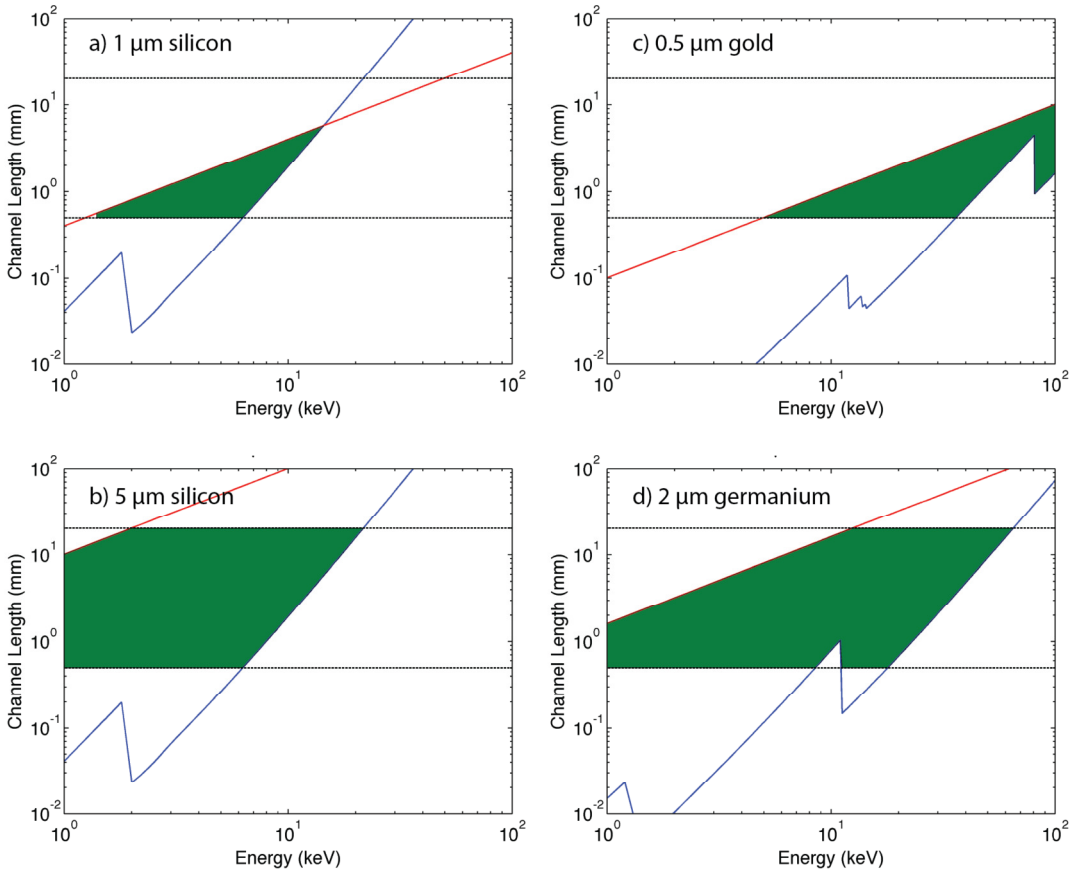

Figure 1. Energy vs. SCA channel length plots for four choices of channel width and absorber material: (a) 1 µm silicon channels, (b) 5 µm silicon channels, (c) 0.5 µm gold and (d) 2 µm germanium channels. In each plot, the lower line at high energy (blue) corresponds to minimum length required for sufficient absorption of unwanted emission from the sample, and the upper line at low energy (red) to maximum length, above which diffraction-induced losses are expected to play a role. The shaded overlap region (green) shows the region in which channels are expected to perform well.[Figure courtesy: Arthur R. Woll and David N. Agyeman-Budu]